



# The origin of collectivity in small systems via heavy-flavour measurements at the ALICE LHC experiment

László Gyulai

Advisor: Dr. Róbert Vértesi

Consultant: Dr. Dániel Péter Kis

Doctoral School of Physical Sciences
Budapest University of Technology and Economics

2025

# Abstract

Quantum chromodynamics (QCD) is a gauge field theory that describes one of the fundamental interactions – the strong interaction. QCD has a dual nature: the strength of the coupling depends on the energy scale. At low energy scales, we observe colour confinement, that is, quarks and gluons are confined into colour-neutral states. On the other hand, at high-energy-scale processes, strongly interacting particles exhibit asymptotic freedom. However, at high energy densities, which can be achieved in modern particle accelerators, a state of matter forms in which quarks and gluons can be found in an unconfined state – the quark-gluon plasma (QGP). This QGP is believed to have comprised the Universe during the first several microseconds after the Big Bang.

Heavy-flavour quarks, charm and beauty, are formed in the initial stages of high-energy hadronic collisions, before the formation of the QGP, and survive throughout the entire evolution of the system. This makes heavy-flavour probes a crucial tool for studying the properties of the QGP.

Recent measurements at particle colliders, such as the LHC and RHIC, have observed effects typically attributed to the presence of the QGP even in small collision systems with both high and low final-state multiplicities. In such systems, the QGP is not expected to form due to much lower energy densities. Theoretical works attempt to explain the observed similarities between small and large collision systems using vacuum QCD models such as mini-jet production or multiple-parton interactions (MPI). Heavy-flavour measurements can aid in testing these QCD models in proton–proton and proton–ion collisions.

In my thesis, I use heavy-flavour production from small to large systems, both in theory and in experiment, to understand the thermodynamical properties and the QGP-like effects in reactions. I investigate the production of heavy-flavour D and B mesons, as well as $c$ and $b$ quarks as a function of transverse-event activity in simulations, to study the influence of MPI on heavy-flavour particle production. Based on the results of these simulations, I carry out the data analysis of $\mathrm{D}^0$-meson production in the ALICE experiment and compare the results with the simulations. Finally, I utilise a non-extensive thermodynamics model to investigate the timeline of heavy-flavour production and compare it with light flavours based on measurements of the ALICE and STAR experiments.

*Dedicated to my loving parents*

# Contents

# Chapter 1

# High-energy hadron collisions

## 1.1 The Standard Model of particle physics

The last century was a fruitful period for the study of elementary particles and the fundamental forces that connect them. With the rapid development of quantum field theory (QFT) and the discovery of an increasing number of particles, it became necessary to create a unified model that could incorporate much of the known theory in particle physics. The Standard Model (SM) emerged as a QFT that incorporates several interactions of matter and organises elementary particles into a periodic table-like system, shown in Fig. 1.1.

Interactions in the Standard Model are associated with local gauge symmetries which determine their mathematical structure. The symmetry group of the SM is $SU(3)_C \times SU(2)_L \times U(1)_Y$, where $SU(3)_C$ corresponds to the strong interaction (Quantum Chromodynamics) with $C$ indicating the colour charge, $SU(2)_L$ is the gauge group of weak interactions with $L$ indicating that it acts only on left-handed fermions, and $U(1)_Y$ corresponds to the electroweak interaction with the hypercharge $Y$.

The particles in the Standard Model can be divided into two main categories depending on their spin:

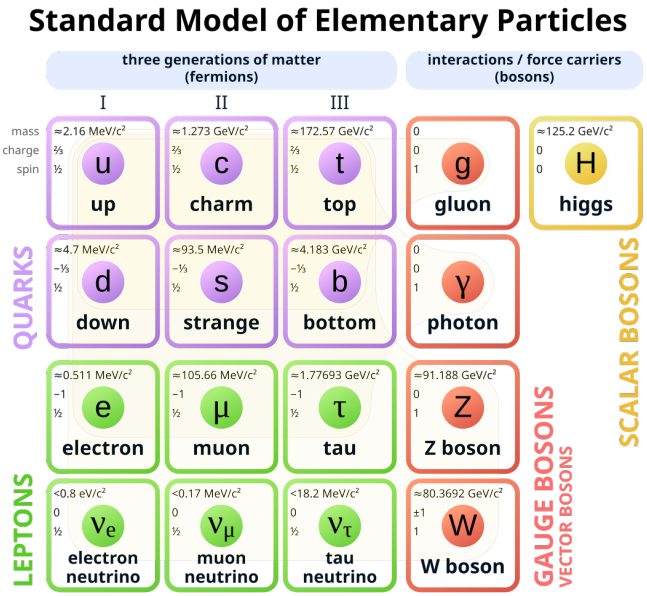


Figure 1.1: Particle content of the Standard Model.
(Source: `https://en.wikipedia.org/wiki/Standard_Model`)

- fermions – half-integer spin particles that follow Fermi – Dirac statistics and build up the visible matter of the Universe. Fermions include quarks, which come in six flavours (up, down, strange, charm, bottom, top). Quarks participate in strong interactions, as well as in electroweak interactions. Another group of fermions is the leptons, which can be organised into three so-called generations: electrons, muons, and tau leptons that carry electromagnetic charge, along with their corresponding neutrinos, which have no charge. Leptons are only subject to electroweak interactions;

- bosons – integer-spin particles that obey Bose – Einstein statistics. These include gauge bosons, which are force carriers: the photon (mediator of electromagnetic interactions), the W and Z bosons (mediators of weak interactions), and eight types of gluons (mediators of strong interactions). The SM also includes an important scalar boson responsible for the acquisition of mass by elementary particles – the Higgs boson.

While the Standard Model has been highly successful in predicting various experimental results – such as the existence of a third generation of leptons and the top quark – it falls short of being a complete theory of fundamental interactions. SM does not explain gravity, and it is unable to explain phenomena such as the presence of dark matter, the observed extent of CP violation, and neutrino oscillations. These and similar phenomena are explored in theories collectively referred to as the Beyond the Standard Model (BSM) physics.

## 1.2 Quantum chromodynamics

Quantum chromodynamics (QCD) is the fundamental theory describing the strong interactions between elementary particles. In QCD, quarks, besides having electric charge and spin, possess an additional property called the colour charge. This quantum number introduces a new degree of freedom, enabling quarks to satisfy the Pauli exclusion principle in multi-quark systems such as baryons. The colour charge comes in three types, referred to as red, green, and blue, by analogy with the RGB colour model. The strong force is mediated by the interaction between particles carrying colour charge, governed by the $SU(3)_C$ gauge symmetry. The $SU(3)_C$ symmetry group has eight generators, corresponding to the gluons that mediate strong interactions. Because gluons themselves carry colour charge, this results in self-interaction of gluons, making QCD a non-Abelian gauge theory.

The QCD Lagrangian describes the dynamics of quarks and gluons, capturing the essential features and symmetries of the strong interaction. It is symmetric under local $SU(3)_C$ transformations and takes the form

$$\mathcal{L}_{QCD} = -\frac{1}{4} F^a_{\mu\nu} F^{a\mu\nu} + \overline{\psi}(i\gamma^\mu D_\mu - m)\psi \ . \tag{1.1}$$

The first term contains the gluon field strength tensor $F^a_{\mu\nu}$, defined as

$$F^a_{\mu\nu} = \partial_\mu A^a_\nu - \partial_\nu A^a_\mu - g_s f^{abc} A^b_\mu A^c_\nu \ , \tag{1.2}$$

where $A^a_\mu$ are the gluon fields, $f^{abc}$ are the structure constants of the Lie algebra, and $g_s$ is the strong coupling constant. The last term of Eq. (1.2) contains self-interactions of the gluon fields. The second term of Eq. (1.1) represents the interaction between quark fields $\psi$ and gluon fields, as well as allows for the inclusion of different quark flavours with distinct masses $m$. The covariant derivative is defined as

$$D_\mu = \partial_\mu + ig_s A^a_\mu \frac{\lambda^a}{2} \ , \tag{1.3}$$

where $\lambda^a$ are the Gell-Mann matrices defining the generators of the $SU(3)_C$ symmetry.

An important property of QCD is that the coupling parameter, $\alpha_s$, varies with the energy scale $\mu$. The running of $\alpha_s$ is governed by the QCD beta function, $\beta(\alpha_s)$, which describes the change of the coupling with respect to the energy scale:

$$\mu \frac{d\alpha_s}{d\mu} = \beta(\alpha_s) \ . \tag{1.4}$$

The solution to this differential equation leads to the energy dependence of $\alpha_s$,

$$\alpha_s = \frac{1}{b_0 \ln\left(\mu^2/\Lambda^2_{QCD}\right)} \ , \tag{1.5}$$

where the parameter $\Lambda_{QCD}$ is the QCD scale, a characteristic energy below which perturbative QCD breaks down, typically ranging from 200 to 300 MeV. The constant $b_0$ depends on the number of active quark flavours $n_f$ at the scale $\mu$ and is given by

$$b_0 = \frac{11 - \frac{2}{3} n_f}{4\pi} \ . \tag{1.6}$$

The running coupling $\alpha_s$ of QCD decreases as the energy scale $\mu$ increases (as shown in Fig. 1.2), or the corresponding length scale decreases, leading to

asymptotic freedom. This property of QCD causes quarks and gluons to interact

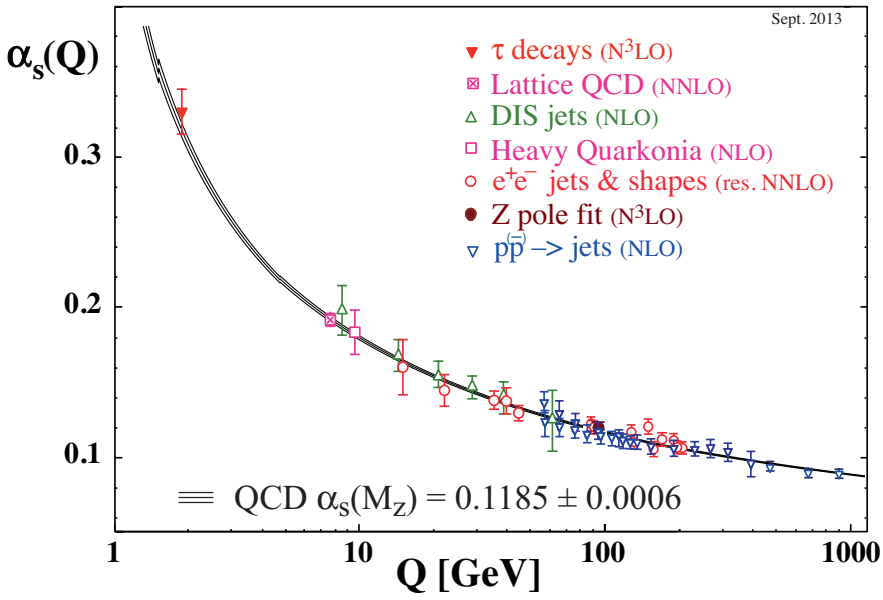


Figure 1.2: Running coupling $\alpha_s$ determined at different energy scales through various measurements and numerical calculations (data points) and compared with theoretical predictions from QCD [1].

more weakly at shorter distances. Due to this asymptotic freedom, quarks behave as nearly free particles inside hadrons at high energies, allowing for precise perturbative calculations of the interactions at these energy scales.

In contrast, at low energies or long distances, the running coupling increases and eventually becomes divergent, leading to an ever-stronger force between quarks as they move further apart. At a critical distance, the force becomes so strong that it leads to the creation of new quark-antiquark pairs, rather than allowing isolated quarks or gluons, as shown in Fig. 1.3. This phenomenon is known as colour confinement, because it prevents the separation of quarks and gluons. As a result, only colour-neutral particles (hadrons) can be observed in nature at low energies and long distances. The production of new quark-antiquark pairs due to the colour confinement leads to the production of hadron showers, which are grouped together in a narrow, collimated cone, known as a jet. Since

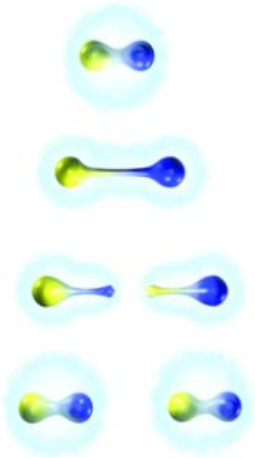

Figure 1.3: Creation of new quark-antiquark pairs due to the colour confinement.

colour confinement is in the non-perturbative regime of the QCD, lattice QCD calculations and simplified, phenomenological models can be used to compute such interactions.

## 1.3 The quark-gluon plasma

It has long been predicted by theoretical studies that a state of matter exists in which quarks and gluons can be found in an unconfined state [2]. This medium, referred to as the quark-gluon plasma (QGP), can only exist under conditions of extremely high temperature and density, resembling the state of the early Universe during the first several microseconds after the Big Bang. The discovery of the QGP and the characterisation of its phase diagram (Fig. 1.4) have become feasible with modern particle accelerators, which perform particle collisions at very high energies.

Although promising potential indicators of the quark-gluon plasma were already observed at the Super Proton Synchrotron (SPS) at the European Organization for Nuclear Research (CERN) [3], clear evidence was first provided by the Relativistic Heavy Ion Collider (RHIC) experiments in the early 2000s [4]. The STAR experiment at RHIC analysed the dijet structures of particles in proton–

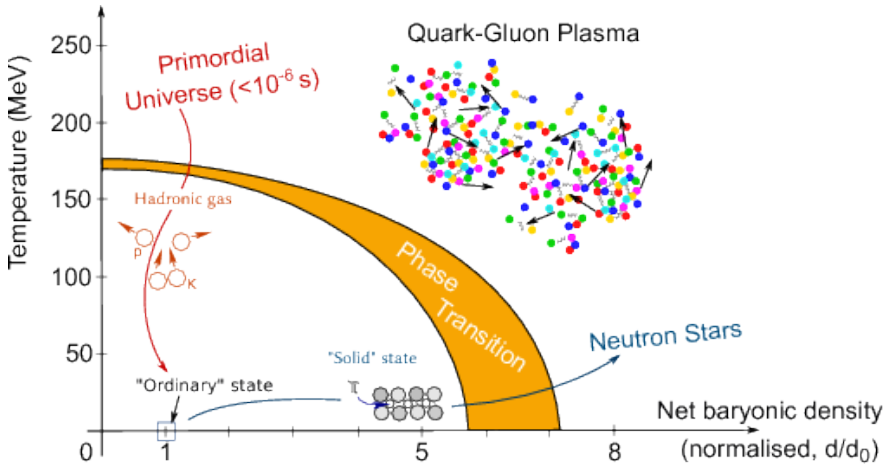


Figure 1.4: Phase diagram (temperature, net baryon density) of QCD matter, ranging from regular nuclear matter to quark-gluon plasma.
(Source: `https://cds.cern.ch/record/2025215`)

proton (pp), deuteron–gold (d–Au), and gold–gold (Au–Au) collisions [5]. Angular correlation of particles within the leading jet (near-side peak, at a relative angle around $\Delta\phi = 0$) was observed in pp, d–Au and Au–Au collisions. However, while the correlations of the leading jet with the recoil jet (away-side peak, at $|\Delta\phi| \approx \pi$) were present in pp and d–Au collisions, as well as in peripheral Au–Au collisions, they were completely absent in central (highly overlapping) Au–Au collisions, as shown in Fig. 1.5. This finding demonstrated the presence of a strongly interacting medium in central Au–Au collisions that is absent in d–Au and in peripheral Au–Au collisions. The secondary jets in these events lost most of their energy during the interaction with the QGP. This phenomenon is known as jet quenching [7]. Similar effects were also observed in Pb–Pb collisions at the Large Hadron Collider (LHC) [8].

A hot and dense medium, created in high-energy collisions, is expected to emit thermal radiation. By measuring the thermal photons produced in collision events, one can probe the properties of the matter in the early stages of the collision. However, the precision of such measurements is limited by the substantial background of photons originating from hadronic decays. Measurements

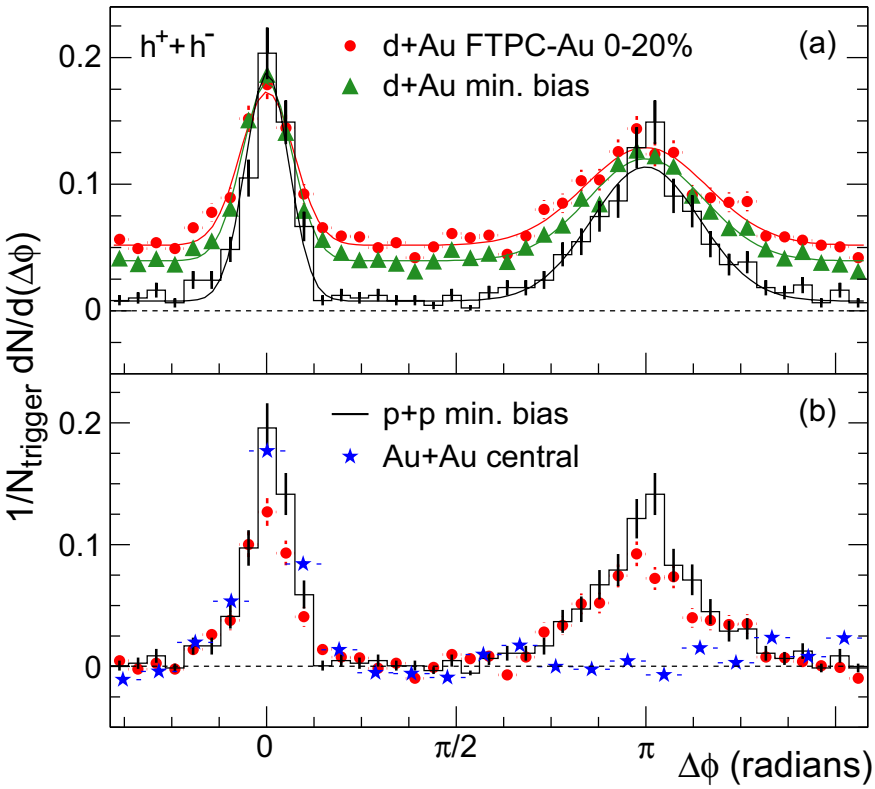


Figure 1.5: Comparison of two-particle azimuthal distributions for central d–Au collisions to those seen in pp and central Au–Au collisions from the STAR experiment [6].

by the PHENIX experiment [9] revealed an excess of direct photons in the thermal regime. The results for Au–Au collisions at $\sqrt{s_{\mathrm{NN}}} = 200$ GeV, shown in Fig. 1.6, imply an initial temperature in the range 250–400 MeV depending on the transverse momentum of photons, corresponding to a few trillions of Kelvin.

Another method for estimating the temperature of the quark-gluon plasma is through the dileptonic decay channel measurements of quarkonia (mesons composed of a heavy quark and an anti-quark of the same flavour). Leptons do not carry colour charge and are therefore unaffected by the strong interaction. This allows them to escape the QGP without interaction. Measurements of $\Upsilon(3S)$ bottomonium at the LHC, at a centre-of-mass energy of $\sqrt{s_{\mathrm{NN}}} = 5.02$ TeV, estimated the QGP temperature at this energy scale to be in the range $T =$

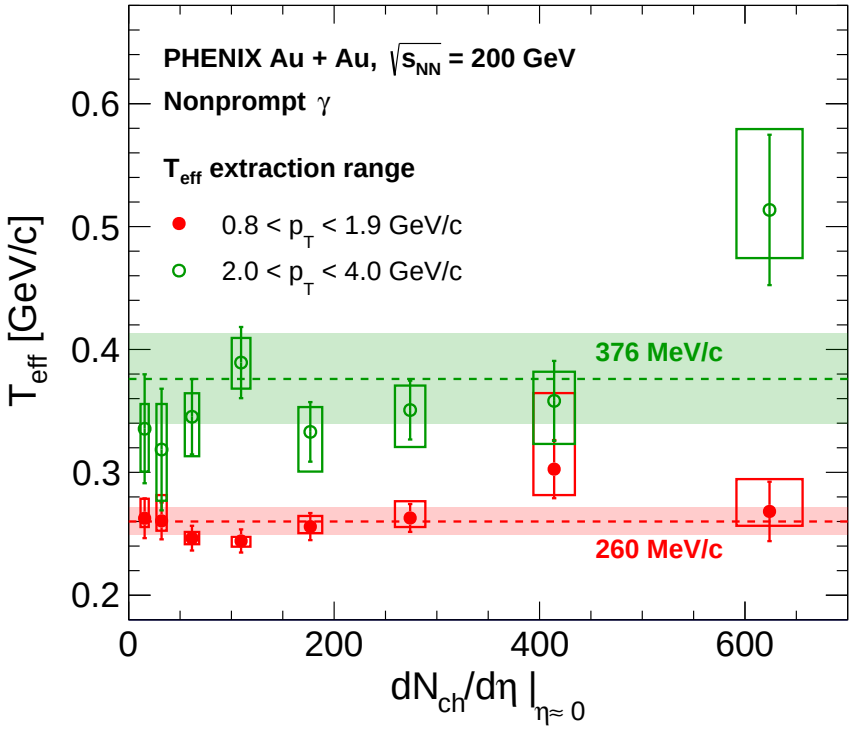


Figure 1.6: Effective temperature $T_{\text{eff}}$ as a function of charged-particle multiplicity $\mathrm{d}N_{ch}/\mathrm{d}\eta$ and transverse momentum of photons $p_{\mathrm{T}}$ at midrapidity measured by the PHENIX experiment [9].

$550 - 800$ MeV [10].

While early theoretical works [2, 11] proposed that the quark-gluon plasma would behave like an ideal gas of quarks and gluons in the state of asymptotic freedom, experiments revealed that the QGP exhibits strong coupling and behaves like an almost perfect (non-viscous) fluid [12, 13]. In non-central heavy-ion collisions, the bulk matter is created with spatial anisotropy in a roughly almond-shaped volume (see Fig. 1.7). Due to the strong coupling, pressure builds up and drives particles away from the interaction point. The pressure is highest in the reaction plane (the plane defined by the two beam axes), where the matter is most strongly compressed. Consequently, the initial spatial anisotropy is converted into momentum anisotropy. This is typically expressed using a Fourier expansion of the momentum distribution in the azimuthal angle [15]. A signifi-

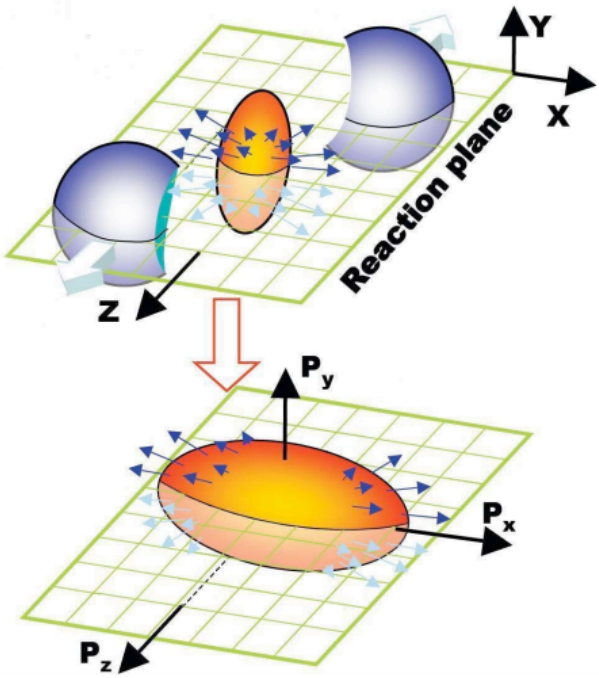


Figure 1.7: Creation of elliptical shaped "fireball" in a semi-peripheral heavy ion collision [14].

cant second Fourier-coefficient ($v_2$, known as the elliptic flow) has been observed in Au–Au collisions at $\sqrt{s_{\mathrm{NN}}} = 200$ GeV at RHIC and in Pb–Pb collisions at $\sqrt{s_{\mathrm{NN}}} = 2.76$ TeV at the LHC [13, 16]. Figure 1.8 shows the measured elliptic flow patterns of baryons and mesons [17]. Analysing $v_2$ as a function of transverse kinetic energy ($KE_{\mathrm{T}}$) results in two distinct branches: one for mesons and the other for baryons. When both $v_2$ and $KE_{\mathrm{T}}$ are scaled by the number of valence quarks ($n_{\mathrm{q}} = 2$ for mesons, $n_{\mathrm{q}} = 3$ for baryons), the two branches merge into a universal curve for all hadrons. This indicates that the flow pattern is developed at the quark level.

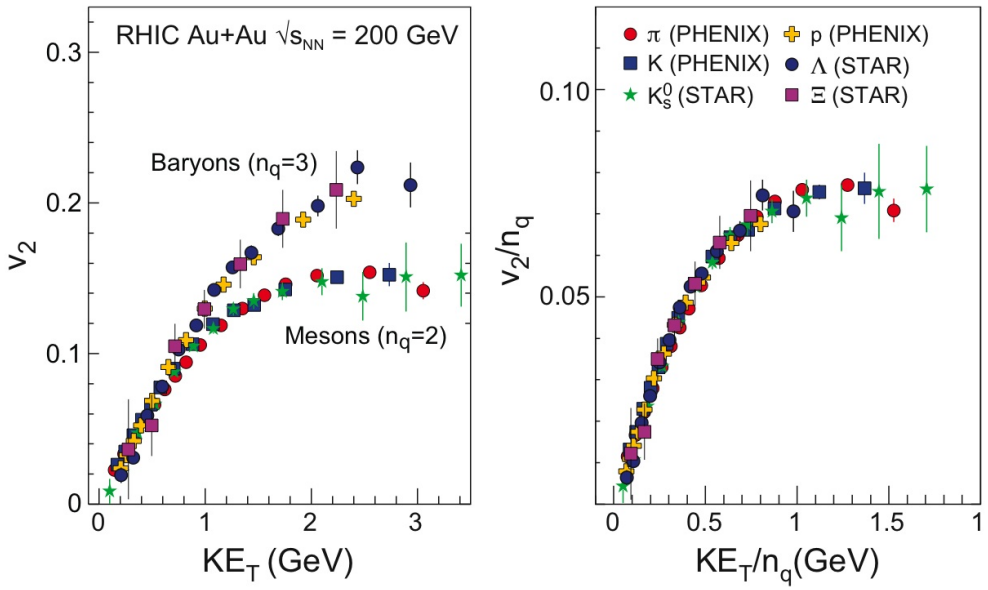


Figure 1.8: Elliptic flow measured for various mesons and baryons as a function of transverse kinetic energy (left) and its collapse into a universal curve when $v_2$ and $KE_{\mathrm{T}}$ are scaled by the number of valence quarks $n_{\mathrm{q}}$ of the hadron (right) from the STAR and PHENIX experiments [17].

## 1.4 Collective effects in small systems

Recently, it was observed that pp collisions with large final-state multiplicity exhibit features similar to proton–nucleus (p–A) and even nucleus–nucleus (A–A) collisions, leading to debates about the possible existence of QGP in small collision systems.

Measurements of azimuthal particle correlations in small collision systems, such as proton–lead (p–Pb) and pp collisions, were performed at the CMS experiment [18, 19]. The results, shown in Fig. 1.9, demonstrate a clear ridge in the $\Delta\phi \approx \pi$ region in high-multiplicity pp events, similar to the one observed in Pb–Pb collisions. In Pb–Pb collisions, this phenomenon can be understood with the presence of QGP. However, it remains an open question whether the QGP can cause this collective behaviour in smaller collision systems, as the energy densities in these collisions may not be sufficient to produce the QGP in significant volumes.

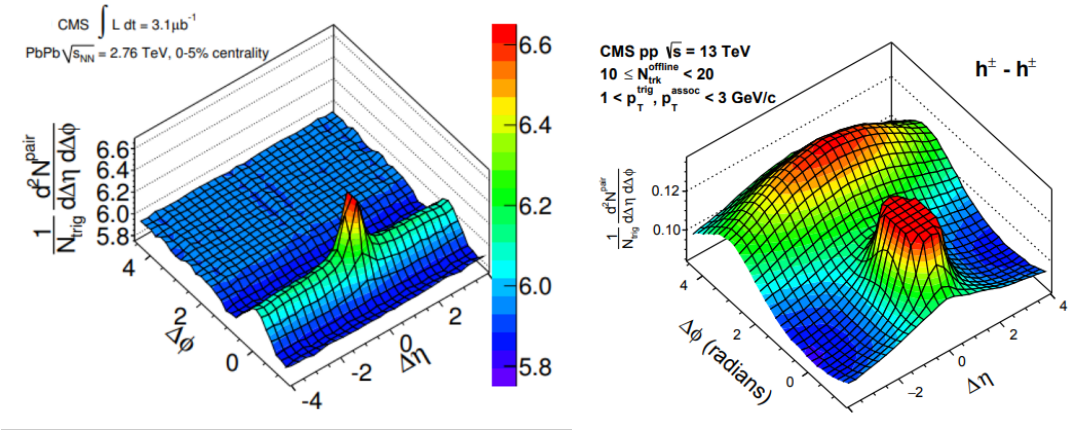


Figure 1.9: Azimuthal particle correlations in Pb–Pb collisions [20] (left) and in high-multiplicity pp collisions [19] (right) measured by the CMS experiment.

The values of the elliptic flow $v_2$ measured in pp collisions appear to be comparable to those observed in low-multiplicity Pb–Pb collisions [21]. The results of this measurement are shown in Fig. 1.10.

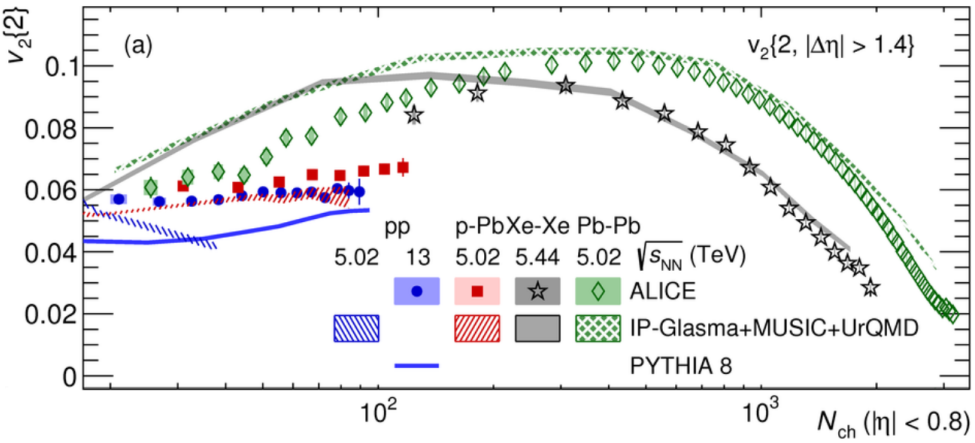


Figure 1.10: Elliptic flow measured using two-particle cumulants with a pseudo-rapidity separation in pp, p–Pb, Xe–Xe, and Pb–Pb collisions as a function of multiplicity from the ALICE experiment [21].

Another QGP-like feature in pp collisions was observed by the ALICE experiment in the measurement of the ratios of the yields of $K^0_S$, $\Lambda$, $\Xi$ and $\Omega$ to the pion yield as a function of multiplicity [22]. A significant enhancement in the strange-to-non-strange hadron production can be seen in Fig. 1.11 with increasing particle

multiplicity in pp collisions. The behaviour observed in pp collisions resembles

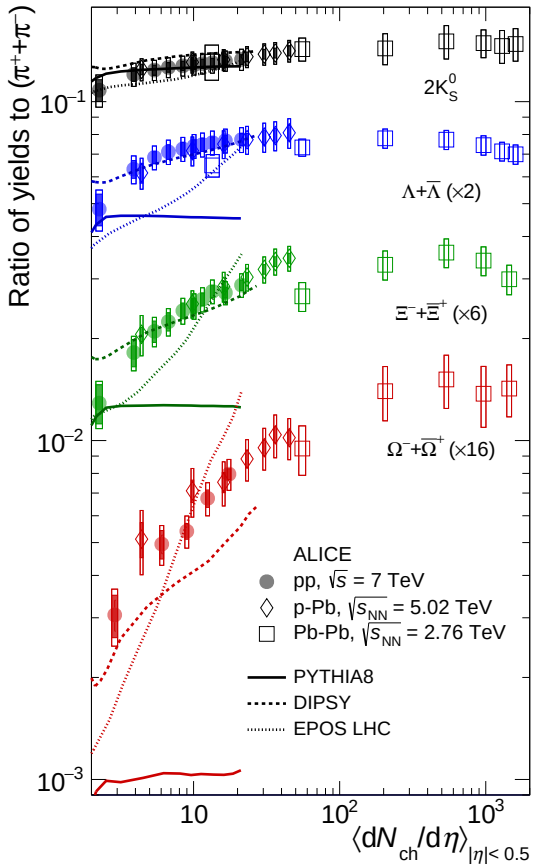


Figure 1.11: $K^0_S$, $\Lambda$, $\Xi$ and $\Omega$ yields ratio to pion yields as a function of multiplicity in pp, p–Pb and Pb–Pb collisions at centre-of-mass energies between $\sqrt{s_{\rm NN}} = 2.76$ TeV and $\sqrt{s_{\rm NN}} = 7$ TeV measured by the ALICE experiment [22].

that of p–Pb collisions at slightly lower centre-of-mass energy, in terms of both the values of the ratios and their evolution with multiplicity. At high multiplicity, the yield ratios reach values similar to those observed in Pb–Pb collisions, where no significant change with multiplicity is observed beyond an initial slight rise.

Some theoretical works assume a QGP droplet in small collision systems [23], or even question the creation of QGP in nucleus-nucleus systems [24]. However, the mainstream explanation for the observed similarities between small and large collision systems are vacuum quantum chromodynamics processes at the soft–hard boundary, such as mini-jet production [25] or multiple-parton interac-

tions (MPI) [26, 27]. A schematic drawing of a pp collision with MPI is shown in Fig. 1.12. There are two major forms of MPI. First, multiple partons within

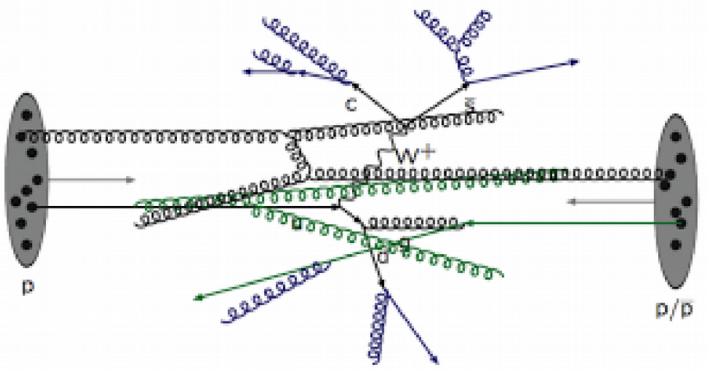


Figure 1.12: Schematics of the multiple-parton interaction.

the projectile and target hadron can scatter, causing more than one hard process. Second, partons can rescatter on each other [28]. Multiple-parton interactions increase overall multiplicity by enhancing the production of the underlying event, i.e. mostly soft hadrons that are not directly related to the leading hard process.

Multiple-parton interactions are also expected to depend on the flavour of the emerging particles. Fragmentation of heavy-flavour jets is expected to differ from that of light-flavour jets due to colour charge and mass effects. The internal structures of heavy-flavour jets may, therefore, provide a deeper insight into the flavour-dependent development of jets and their connection to the underlying event.

## 1.5 Heavy flavour

Heavy-flavour charm ($c$) and beauty ($b$) quarks are produced in the initial stages of high-energy hadronic collisions through hard partonic scatterings (see Fig. 1.13). The production and fragmentation of heavy flavour differ significantly from those of light-flavour partons due to colour-charge and mass-related effects [29, 30].

The mean lifetime of heavy-flavour quarks is sufficient for them to survive

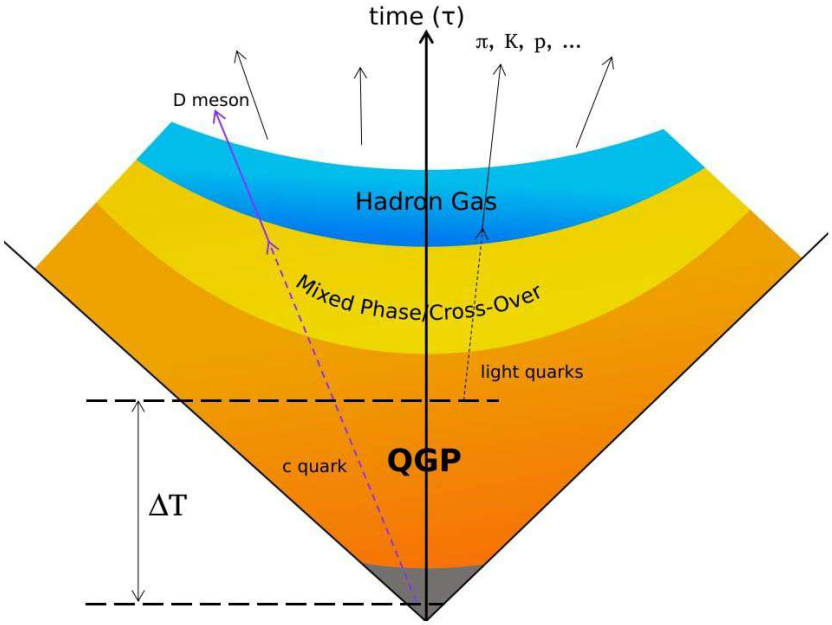


Figure 1.13: Schematic view of the evolution of matter in a high-energy nucleus-nucleus collision. Heavy $c$ quarks are produced in the initial stages, while light quarks are formed in the QGP phase. Later, during the phase transition, quarks combine to form hadrons.

throughout the collision, hadronise, and escape the interacting medium, thus they carry information about each stage of the collision. In heavy-ion collisions, heavy-flavour probes can be used to investigate the transport properties of the quark-gluon plasma. Proton on heavy-ion collisions can be used to isolate and understand cold nuclear matter (CNM) effects, that are also present in A–A collisions. In proton–proton collision systems, heavy flavour is primarily used to test perturbative QCD models by measuring cross sections of produced particles.

The measurement of heavy-flavour production in pp collisions allows for testing the factorisation theorem, which describes heavy-flavour production as a convolution of four terms [31] (Fig. 1.14):

$$\sigma_{AB\to C} = f_{a/A}(x_a, Q^2) \otimes f_{b/B}(x_b, Q^2) \otimes \sigma_{ab\to c} \otimes D_{c\to C}(z, Q^2) \ , \qquad (1.7)$$

where $f_{a/A}(x_a, Q^2)$ and $f_{b/B}(x_b, Q^2)$ are the parton distribution functions of the

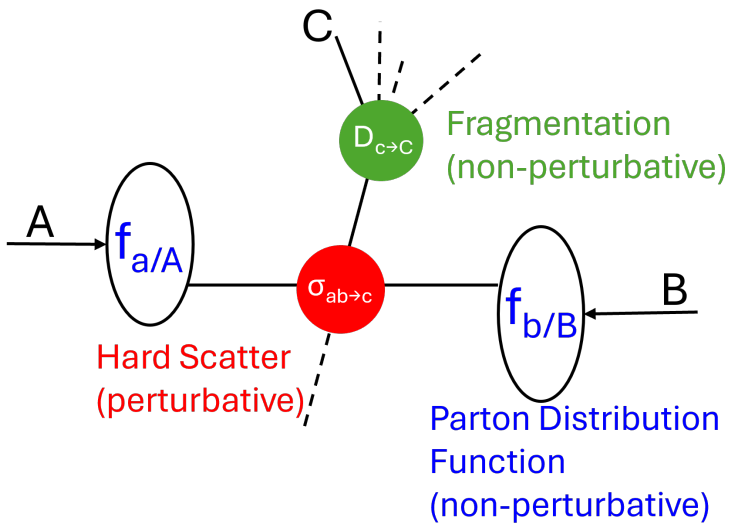


Figure 1.14: Schematics of the A+B→C process as described by the factorisation theorem.

incoming beam particles, $\sigma_{ab\to c}$ is the hard-scattering cross section of the partons, and $D_{c\to C}(z, Q^2)$ is the fragmentation function. Measurements by the ALICE and CMS experiments [32, 33] have shown that charm baryon-to-meson ratios are significantly enhanced compared to those observed in $e^+e^-$ and $e$p collisions. These results are underpredicted by models based on fragmentation functions estimated in those collision systems, thereby questioning the universality of fragmentation.

The lightest heavy-flavour particles are D mesons. They consist of a $c$ quark bound to a light ($u$, $d$) or strange ($s$) antiquark, or vice versa. The D mesons decay weakly via hadronic or semileptonic channels. The weak decay of the $c$ quark is only possible into one of the lighter $u$ or $d$ quarks, resulting in decay products that are mostly pions and kaons (e.g., $\mathrm{D}^0 \to K^-\pi^+$, $\mathrm{D}^+ \to K^-\pi^+\pi^+$, $\mathrm{D}^0 \to K^-e^+\nu_e$). D mesons are not detected directly because their mean lifetime, though much longer than the timescale of the collision, is still too short for them to reach the detectors. However, modern detectors are precise enough to measure the secondary vertex of their decays, which helps with reconstructing the original D mesons from their decay products.

B mesons contain a $b$ quark or antiquark along with one of the $u$, $d$, $s$, or $c$ quarks or antiquarks. As a result, B mesons often decay into mesons with charm quark components, such as D mesons. This makes detecting them even more challenging because their primary decay products, such as D mesons, are themselves not detected directly in many cases.

The measured self-normalised yields of heavy flavour show a steeper-than-linear increase with multiplicity, as can be seen in Fig. 1.15 [34]. The contribution

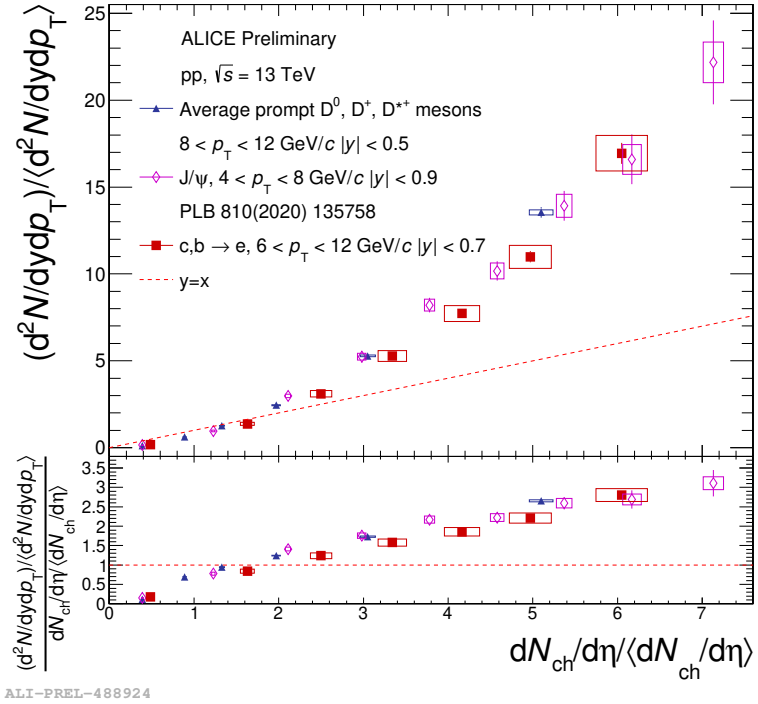


Figure 1.15: Average D-meson, J/$\Psi$, and heavy-flavour decay electrons self-normalised yields as a function of relative charged-particle multiplicity in pp collisions at $\sqrt{s} = 13$ TeV measured by the ALICE experiment [34].

of MPI in collisions where heavy quarks are produced can induce a correlation between the heavy-flavour yields and the charged-particle multiplicity produced in the collision. However, auto-correlation effects may also play a role if the multiplicity is estimated in the same region as the heavy-flavour yields. The auto-correlation effects can be mitigated by estimating the multiplicity in a region of pseudorapidity or azimuth angle that is distant from the measurement region.

# Chapter 2

# Experimental methods

## 2.1 Ultrarelativistic particle colliders

In the second half of the XX century, large particle accelerators were constructed, that allowed for the study of QCD matter at previously unprecedented energy levels. One of the first circular colliders which could reach energies of up to a few hundred GeV, the Large Electron-Positron Collider (LEP), was built at the European Organization for Nuclear Research (CERN) facility and operated between 1989 and 2000.

In 2001, the LEP was dismantled to make way for the Large Hadron Collider (LHC). The LHC reused the 27-km-circumference tunnel originally constructed for the LEP (Fig. 2.1). At the LHC, particles are accelerated in two parallel vacuum beam pipes, each containing a beam of particles moving in opposite directions. The beams intersect at four designated points, where detectors register the collisions. The particles within beams are accelerated and focused with the help of superconducting magnets at an operating temperature of 1.9 K.

There are four main large detectors operating at the LHC's intersection points: Compact Muon Solenoid (CMS), A Toroidal LHC Apparatus (ATLAS), A Large Ion Collider Experiment (ALICE), and LHC-beauty (LHCb). The CMS is a

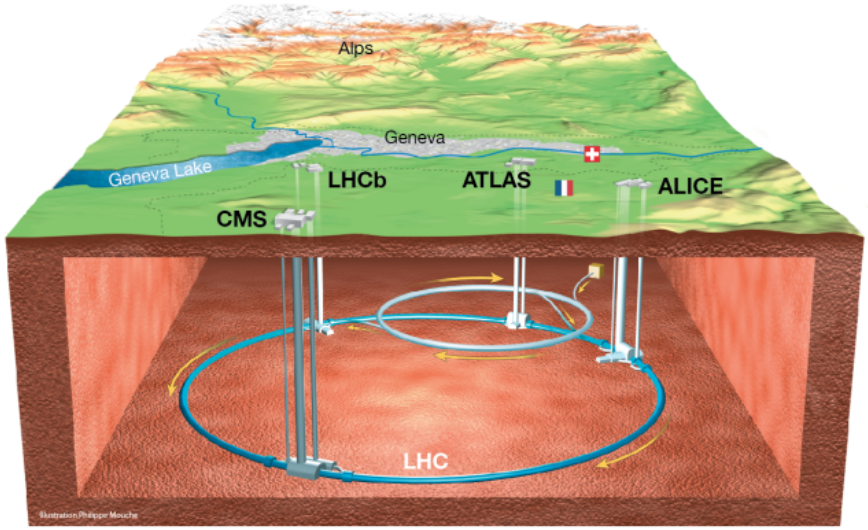


Figure 2.1: Overall view of the LHC.
(Source: `https://cds.cern.ch/record/1708847`)

general-purpose detector primarily focused on testing Standard Model predictions, as well as investigating Higgs physics and Beyond-the-Standard-Model physics. It also has an extensive heavy-ion physics program, aimed at studying the properties of the QGP. Similarly to CMS, ATLAS is designed to explore a wide range of physics phenomena, though with slightly different design choices. The ALICE detector is specifically designed to study the properties of strongly interacting matter at extreme energy densities and temperatures, with a primary focus on exploring the quark-gluon plasma. The LHCb detector mainly focuses on the production and decay of heavy-flavour particles, particularly those involving the bottom quark.

The first proton–proton collisions at the LHC were recorded in 2010 at an energy of 3.5 TeV per particle beam. The long-anticipated Higgs boson was discovered simultaneously in CMS and ATLAS in 2012, during the first LHC operational period (Run 1) [35, 36]. In the second run period (Run 2), the LHC reached the collision energies of 13 TeV for proton–proton beams. Currently, in

the ongoing Run 3 period, the LHC is operating at a collision energy of 13.6 TeV and with higher luminosity compared to Run 2. The future transition of the LHC into the High-Luminosity LHC will further increase the collision rate to provide experiments with large amounts of experimental data.

On the other side of the globe, at the Brookhaven National Laboratory (BNL), another heavy-ion particle collider was built and brought online in 2000: the Relativistic Heavy Ion Collider (RHIC). RHIC features two beam pipes that accelerate particles in opposite directions. RHIC has a slightly hexagonal shape with curved edges and a circumference of nearly 4 km (Fig. 2.2). The RHIC apparatus

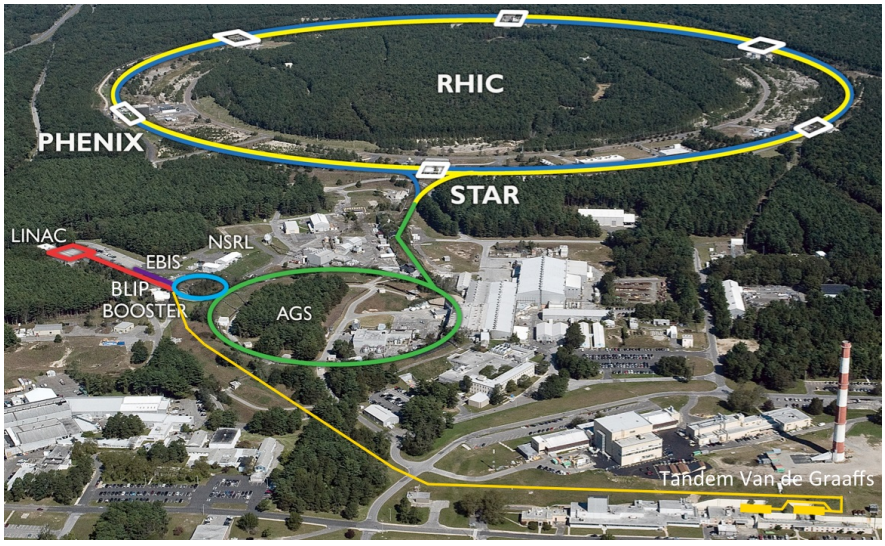


Figure 2.2: Layout of RHIC facility.
(Source: `https://www.bnl.gov/cad/accelerator`)

is extremely versatile and optimised for studying heavy-ion collisions. The most common particles involved in collisions are gold, copper, lead, deuterons, and protons. RHIC also has a unique capability to collide polarised protons, allowing for the study of the spin structure of protons. Additionally, RHIC has the capability to operate at lower collision energies compared to the LHC, ranging from 5.5 GeV for Au–Au collisions to up to 510 GeV for proton–proton collisions. In the fixed-target configuration, RHIC achieves the lowest possible centre-of-mass energy per nucleon pair, down to $\sqrt{s_{\mathrm{NN}}} = 3$ GeV.

There are two experiments currently operating at RHIC: STAR and sPHENIX. STAR is focused on detecting hadrons with its system of time projection chambers, which cover a large solid angle, while sPHENIX is further specialised in detecting rare and electromagnetic particles, utilising a detector system with only partial spatial coverage.

## 2.2 The ALICE experiment

In my doctoral work, I carried out data analysis on the ALICE data and also relied on the ALICE and STAR data for phenomenological studies. This section provides a description of the ALICE detector. The STAR detector has a very similar design [37].

The ALICE detector (Fig. 2.3) focuses mainly on the physics of strongly interacting matter at extreme energy densities. The main subject of study at

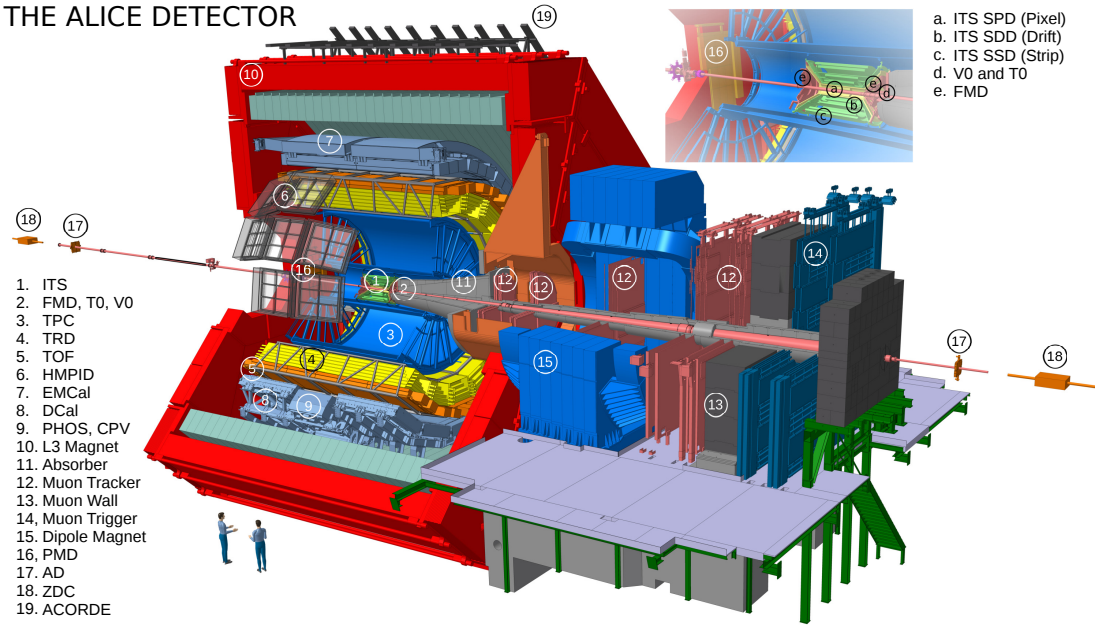


Figure 2.3: ALICE schematics as during Run 2.
(Source: `https://cds.cern.ch/record/2263642`)

the experiment is to understand the formation and evolution of QGP, with the

ultimate goal of investigating the nature of strong interactions and colour confinement. It primarily concentrates on measurements in heavy-ion (typically Pb–Pb) collisions, but its rich physics program also extends to the smaller pp and p–Pb collision systems.

In the data analysis described in Chapter 4, particle tracking and identification were performed using a combination of two detectors: the Inner Tracking System (ITS) [38] and the Time Projection Chamber (TPC) [39]. The ITS detector, the innermost subsystem of the ALICE detector, is composed of six cylindrical layers of silicon detectors and it is involved in tracking the emerging particles close to the interaction point. One of its main purposes is to identify the spatial origin of charged particles with very high precision (up to fractions of a millimetre). Such precision allows for the distinction between particles originating from the primary vertex (the location of the collision) and those stemming from weak particle decays at a secondary vertex, thus ITS is essential to perform heavy-flavour measurements.

The TPC is a gas-filled detector located outside the ITS with a volume of 88 $\mathrm{m}^3$ and serves as the main particle tracking device in ALICE. Charged particles moving through the gas mixture ionise it, freeing electrons that drift toward the end plates of the detector. The ALICE detector is placed inside a large solenoid magnet inherited from the L3 LEP experiment, enabling measurement of the mass and charge of particles by analysing the curvature of their trajectories. The particle identification is further carried out via the measurements of the specific ionisation energy loss $\mathrm{d}E/\mathrm{d}x$ in the TPC.

Both the ITS and the TPC cover the pseudorapidity interval $|\eta| < 0.9$ and operate in a magnetic field of $B = 0.5$ T, provided by the cylindrical solenoid. Particle identification for charm-hadron decay products is further improved by the Time-Of-Flight (TOF) detector [40], while the trigger signal is provided by the V0 detector, which consists of two scintillator arrays covering the pseudorapidity intervals $-3.7 < \eta < -1.7$ and $2.8 < \eta < 5.1$ on either side of the nominal

collision point [41].

A detailed description of the ALICE apparatus can be found in Ref. [42].

## 2.3 Modelling in high-energy physics

We use computer modelling in several areas of high-energy physics. Theoretical frameworks and computational techniques are used to make predictions for particle production in interactions. One of the most often used methods is Monte Carlo (MC) calculations. These can be used to solve deterministic problems in a stochastic manner, such as computing complex integrals. The major event generators work on MC principles to create complete collision events that model the whole process from the incoming hadrons to the final state. The outcome can be compared to data to understand underlying mechanisms. Passage through matter is also simulated with MC methods, facilitating detector development and giving accurate physics predictions. Furthermore, simulations can be used to create pseudo-experiments and estimate systematic effects.

### 2.3.1 PYTHIA 8

The PYTHIA 8 event generator is one of the most commonly used software tools in particle physics, designed to simulate the complex physical processes occurring in high-energy particle collisions. Although the starting point of a simulation is usually a simple cross section computed in fixed-order perturbation theory, the total probability distribution for simulated events typically cannot be expressed analytically. Instead, it is evaluated using numerical methods, with Markov Chain Monte Carlo (MCMC) algorithms based on pseudorandom number generators as the main ingredient. PYTHIA 8 simulates high-energy collisions in the following main steps [43]:

1. First, a hard scattering of two partons, one from each incoming hadron,

into a few outgoing particles is calculated. The initial partons are selected according to parton distribution functions, and the kinematics of the outgoing particles are determined using perturbation theory. These calculations are performed with the leading-order corrections, which are further refined in subsequent steps. The hard process may also produce gauge bosons or short-lived top quarks, whose decays must also be considered.

2. The next step involves the parton shower, which includes the initial-state radiation (ISR) and final-state radiation (FSR) of additional particles from the hard scattering and any resonance decays.

3. Additional scattering processes between partons from the incoming beams, the multiple-parton interactions, are also included.

4. Non-perturbative colour dipoles, referred to as strings, begin to form after the MPIs. These formations are typically not unique in the $N_c = 3$ case, and ambiguities in the colour-space configuration can be resolved using the so-called colour reconnection (CR) methods.

5. The strings fragment into hadrons according to the Lund string model, a widely used framework for describing hadronisation. Unstable hadrons produced during fragmentation decay into other particles to form the stable final state.

6. In densely populated regions of phase space, the produced particles may rescatter, reannihilate, or recombine with one another.

The main applications of PYTHIA 8 include testing theoretical hypotheses by comparing simulations to data, interpreting measurements (including estimating systematic uncertainties), and developing experimental strategies and detector designs. It also serves as an important tool for exploring new theoretical ideas.

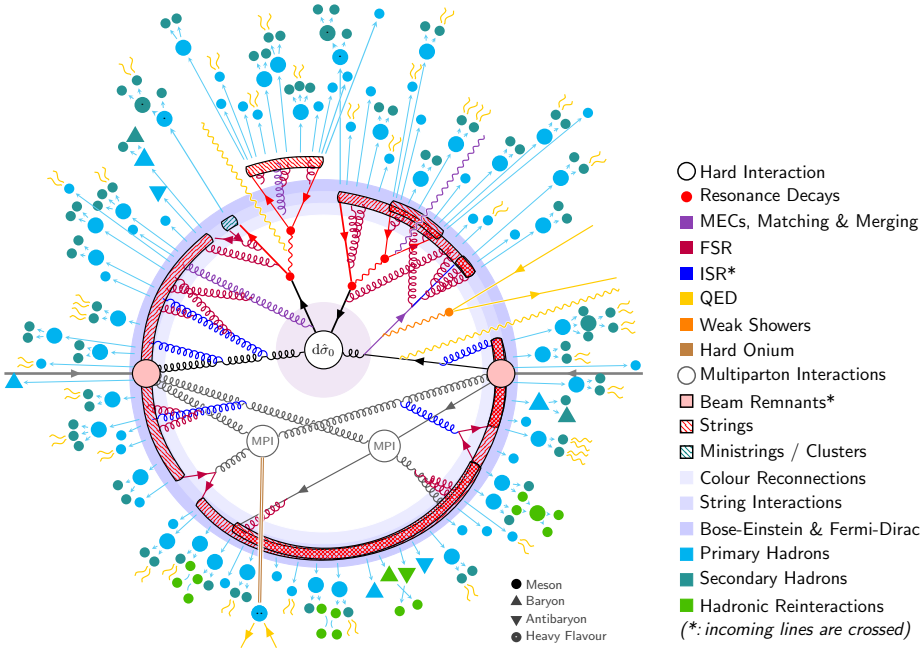


Figure 2.4: Schematic of the structure of a pp $\rightarrow t\bar{t}$ event, as modelled by PYTHIA 8 [43].

PYTHIA 8 can be parametrised (tuned) in multiple ways to test different approaches to the simulation of high-energy collisions. A standard tune of PYTHIA 8, called the Monash 2013 tune [44], was parametrised to reproduce observables measured in pp collisions at the LHC, using data from minimum-bias events, Drell – Yan processes, and from the underlying events. The energy dependence of the parameters was constrained by data from the SPS, Tevatron, and the LHC. However, the Monash tune fails to accurately reproduce strangeness enhancement and baryon-to-meson production ratios. This discrepancy arises from the non-universality of heavy-quark fragmentation across different collision systems.

The PYTHIA CR-BLC (colour reconnection beyond leading colour) tune introduces junctions to the PYTHIA 8 colour strings and is better suited for reproducing heavy-flavour production [45]. The CR-BLC tune has three modes, which differ in their time-dilation constraints. Mode 2, considered the "standard" parametrisation for the CR-BLC tune, requires that all dipoles involved in

a reconnection be causally connected.

In Chapter 3, I provide predictions using phenomenological modelling based on the PYTHIA 8 Monash tune, while in Chapter 4 I also utilise the CR-BLC Mode 2 parametrisation to compare with the data.

### 2.3.2 The FONLL formalism

In processes involving hard scatterings or heavy-flavour production, the leading-order simulations by PYTHIA 8 are usually not accurate enough. Next-to-leading-order event generators, like POWHEG [46], include higher-order QCD corrections to leading-order processes. However, event generators have the shortcoming that obtaining results with the desired precision may need a lot of time and resources. For simple observables such as cross sections, direct calculations can be better suited.

Performing next-to-leading order calculations for heavy-flavour production is a complex task when dealing with high-energy particles. If the renormalisation scale is close to the heavy-quark mass, the mass of the heavy quark acts as an infrared cutoff on collinear singularities, leading to a power expansion in the strong coupling constant $\alpha_{\mathrm{s}}$ [47]. However, this approach fails when the transverse momentum $p_{\mathrm{T}}$ of the heavy quark is much larger than its mass $m$, as large logarithms of the ratio $p_{\mathrm{T}}/m$ emerge at all orders in the perturbative expansion, spoiling the convergence.

The FONLL formalism is used for computing the theoretical predictions of heavy-flavour production [48]. The notation FONLL stands for Fixed-Order plus Next-to-Leading Logarithms. In this formalism, the terms of order $\alpha_{\mathrm{s}}^2$ and $\alpha_{\mathrm{s}}^3$ are included exactly, including mass effects, and the terms of order $\alpha_{\mathrm{s}}^2\alpha_{\mathrm{s}}^k \log^k p_{\mathrm{T}}/m$ and $\alpha_{\mathrm{s}}^3\alpha_{\mathrm{s}}^k \log^k p_{\mathrm{T}}/m$ are also included exactly. This allows for the merging of the fixed-order and fragmentation-function approaches.

In Chapter 4, I used interactive calculations based on the FONLL formalism

to compute the contribution of B-meson decays to the yield of D mesons.

### 2.3.3 GEANT

With the increasing scale and complexity of high-energy physics experiments, simulation studies have become increasingly essential for designing and optimising detectors, developing analysis software, and interpreting experimental data. GEANT is a system of detector description and simulation tools developed to satisfy these needs [49].

The GEANT program simulates the passage of elementary particles through matter. One of its applications is simulating the transport of particles through the experimental setup to study detector response. This can be done for both measured and recorded data, as well as for events simulated by Monte Carlo generators. GEANT also provides a graphical representation of the detector setup and particle trajectories, which simplifies debugging and helps reveal weaknesses in both hardware and software.

In Chapter 4, GEANT 3 is utilised to estimate the detection efficiency of D mesons, as well as geometrical acceptance of the ALICE detector.

## 2.4 Description of high energy collisions

In this Section, I introduce parameters and observables in high-energy collision events that are frequently mentioned throughout this thesis.

### 2.4.1 Kinematic observables

In ultra-relativistic collisions, a set of kinematic variables is used to describe the event and its participants. As inelastic scattering processes can be characterised by the momentum transfer perpendicular to the beam axis, the projection of the total momentum of the particles onto the transverse plane, the so-called

transverse momentum, $p_{\mathrm{T}}$, is often used. The vectorial sum of all $p_{\mathrm{T}}$ values of an event can be approximated as zero, however, due to different factors (like a small angle between incoming beams, or presence of undetectable neutrinos) it is never exactly zero.

Rapidity, another important and widely-used parameter in high-energy collisions, is a measure of a particle's velocity along the collision axis. It is used to characterise the longitudinal motion of particles produced in events:

$$y = \frac{1}{2} \ln \frac{E + p_z c}{E - p_z c} \, , \tag{2.1}$$

where $E$ is the energy of the particle and $p_z$ is its momentum component along the beam axis. Unlike velocity or other parameters, rapidity differences are invariant under Lorentz boosts along the beam axis. Consequently, when two particles undergo a Lorentz transformation, their rapidity difference does not change, simplifying calculations in boosted frames.

In high-energy physics, rapidity is often approximated by the pseudorapidity $\eta$ – a purely geometrical parameter, directly related to the angle $\theta$ between the particle's momentum and the beam axis,

$$\eta = -\ln \left( \tan \frac{\theta}{2} \right) \, . \tag{2.2}$$

In the $m \to 0$ ($E \approx |\overrightarrow{p}|$) limit, rapidity reduces to the pseudorapidity.

To describe the energy of a pp collision, $\sqrt{s}$ is used, where $s$ is the Mandelstam variable that is Lorentz-invariant. The value of $\sqrt{s}$ represents the centre-of-mass energy of the colliding beams.

### 2.4.2 Multiplicity and centrality

Charged-particle multiplicity is one of the most commonly used event classifiers, providing information about both soft and hard QCD processes occurring during

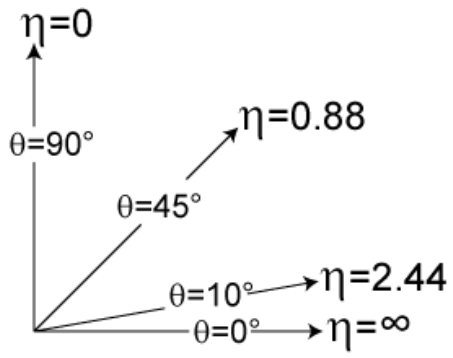


Figure 2.5: Correspondence between pseudorapidity values and the polar angle $\theta$ between momentum of the particle and the positive direction of the beam line.

the collision. It offers insight into both the leading process and the underlying event activity.

The multiplicity of an event can be defined in different ways, depending on the object of study. Technically, the simplest multiplicity estimator is the number of particles at mid-rapidity ($|\eta| < 0.8$). However, a drawback of this definition is that it also includes the contribution of the observed mid-rapidity regions, particularly jet fragments. This leads to autocorrelation and thus the interpretation of the results is not straightforward. A remedy for this, in the case of a suitable detector, is to introduce a rapidity gap between the acceptance of the measurement and the region used for the multiplicity estimation. This so-called forward multiplicity is measured by the V0 detector in the pseudorapidity regions $2.8 < \eta < 5.1$ and $-3.7 < \eta < -1.7$ in the case of the ALICE experiment.

In heavy-ion collisions, an important parameter is the centrality of an event. It describes the geometric configuration of the collision, specifically the degree of overlap between the two colliding ions (see Fig. 2.6). A central collision corresponds to a high degree of overlap between the nuclei, where the colliding nuclei pass very close to each other, leading to a high energy density in the interaction zone. On the other hand, a peripheral collision occurs when the nuclei only brush each other, resulting in a lower energy density.

The collision centrality is defined as a fraction of a total inelastic nucleus–

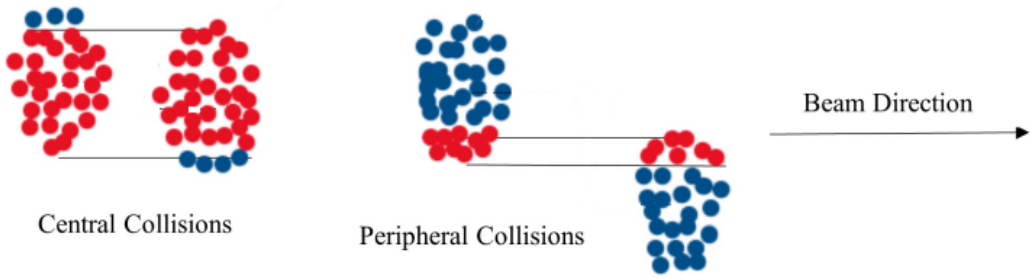


Figure 2.6: Schematic representation of central and peripheral collisions.

nucleus cross section ($\sigma_{\text{inel}}^{\text{AA}}$):

$$\text{Centrality} = \frac{1}{\sigma_{\text{inel}}^{\text{AA}}} \int_0^b \frac{\mathrm{d}\sigma}{\mathrm{d}b'} \mathrm{d}b' \ , \tag{2.3}$$

where $b$ is the impact parameter and $\frac{\mathrm{d}\sigma}{\mathrm{d}b}$ is the differential cross section of a nucleus– nucleus collision.

In experiments, however, centrality is measured by comparing the charged-particle multiplicity in a collision to theoretical predictions from the Glauber model [50]. The distribution of the centrality classes based on the summed amplitudes in the V0 detector, as measured by the ALICE experiment [51], is shown in Fig. 2.7.

### 2.4.3 Event classification by transverse activity

Final states are usually subdivided into two categories: particles originating from processes related to the primary hard scattering (the primary hard process), and particles that come from other sources, such as secondary hard collisions and interaction with the beam remnants (the underlying event, UE). The UE is usually assumed to be independent of the primary process. However, recent considerations propose that there is an interconnection between the two, e.g. via multiple parton interactions. These relations can be studied in the transverse plane of a

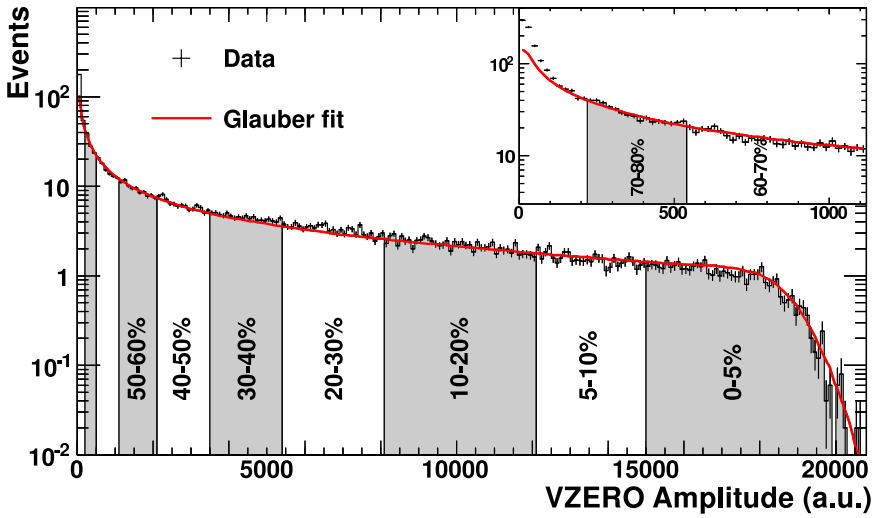


Figure 2.7: Distribution of the summed amplitudes in the V0 scintillator measured by the ALICE experiment compared with the Glauber model [51].

collision (see Fig. 2.8).

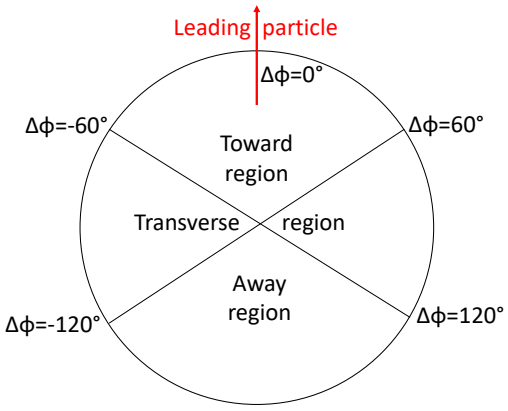


Figure 2.8: Schematic view of three regions in the transverse plane.

In the following, I use the CDF (Collider Detector at Fermilab) categorisation for the event activity [52], which is practical in case of two-jet events. First, the highest-transverse-momentum particle (leading particle) is selected as a proxy for an energetic jet. The region around it, spanning $|\Delta\varphi| < \frac{\pi}{3}$, is called the

toward region. ($\Delta\varphi$ is the azimuth angle relative to the leading hadron.) Most of the jet fragments are expected in this region. The recoil jet will be typically contained in the away region, defined as $|\Delta\varphi| > \frac{3\pi}{2}$. In the transverse region (which comprises parts defined by $\frac{\pi}{3} < |\Delta\varphi| < \frac{2\pi}{3}$), the influence of the hard processes becomes much weaker (negligible in events with back-to-back jets). This region is dominated by soft, underlying processes, although hard radiation may also contribute in events with more complicated topologies [53].

The relation between particle production in these regions and the hardness of the main event has been studied in various experiments over a broad range of energies, from RHIC [54] to the LHC [55–57]. Recently, a measurement in pp collisions at $\sqrt{s} = 13$ TeV was performed by the ALICE experiment [58]. The average number of charged particles increases steeply with the transverse momentum of the leading particle up to $p_{\mathrm{T}}^{\mathrm{leading}} \approx 5$ GeV/$c$ in all three regions (Fig. 2.9). Above $p_{\mathrm{T}}^{\mathrm{leading}} \approx 5$ GeV/$c$, particle production continues to rise in the toward and

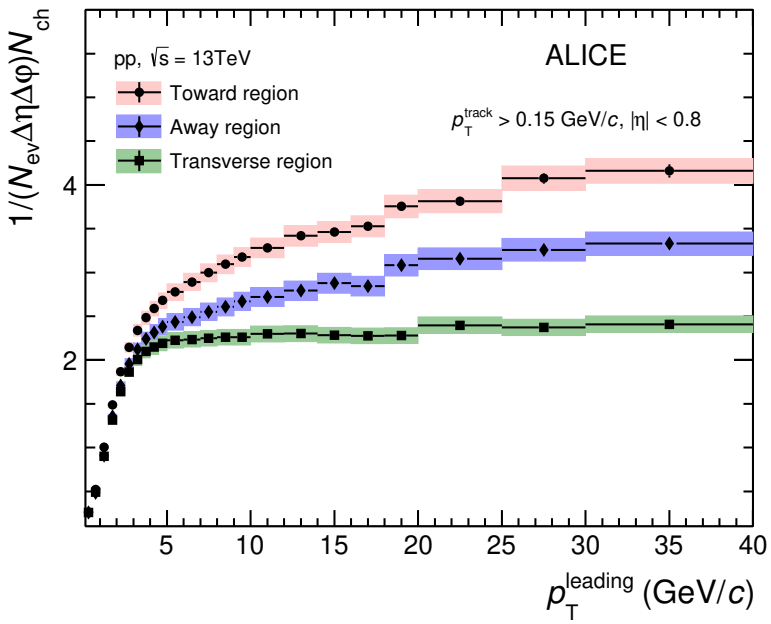


Figure 2.9: Charged-particle multiplicity measured in the toward, away, and transverse regions as a function of the transverse momentum of leading particle in pp collisions at 13 TeV centre-of-mass energy in the ALICE experiment. [58]

away regions, although at a smaller rate. In the transverse region, however, particle production saturates and reaches a plateau at $p_{\mathrm{T}}^{\mathrm{leading}} \approx 5$ GeV/$c$. This shows that the transverse region is not affected strongly by a sufficiently energetic hard scattering, and thus the transverse region primarily represents the underlying event.

In Ref. [59], it was proposed to introduce the relative transverse activity $R_{\mathrm{T}}$ for event characterisation by the activity of the underlying event. The $R_{\mathrm{T}}$ is defined as the ratio of the inclusive number of charged particles in the transverse region in an event, $N_{\mathrm{trans}}$, to the event-averaged number density, $\langle N_{\mathrm{trans}} \rangle$:

$$R_{\mathrm{T}} = \frac{N_{\mathrm{trans}}}{\langle N_{\mathrm{trans}} \rangle} \ . \tag{2.4}$$

As a self-normalised observable, $R_{\mathrm{T}}$ is relatively insensitive to centre-of-mass energy and variations in kinematic selection. At the same time, the transverse activity classifier covers a large dynamic range in terms of event activity. According to simulations, $R_{\mathrm{T}}$ is strongly correlated to MPI in a collision [59], therefore measuring it will indirectly classify events by MPI.

### 2.4.4 Jet reconstruction

Jets are collimated sprays of particles that emerge from the hadronisation of quarks or gluons produced in high-energy collisions. When partons are produced in a collision, they radiate gluons and split into additional quarks and gluons due to the colour confinement, creating a cascade of particles. This parton shower eventually hadronises into colour-neutral hadrons through non-perturbative QCD processes. The resulting jets typically consist of pions, kaons and nucleons, although higher-mass resonances can also be produced.

From an experimental point of view, jets are sprays of particles that have to be clusterised and connected to the initiating parton. Several algorithms exist for jet reconstruction [60, 61]. These algorithms group particles based on their

proximity in momentum space, with an emphasis on simplicity and robustness. Another property of jet reconstruction which is critical for theoretical predictions is the infrared safety. It ensures that the presence of soft, low-energy particles does not affect the final jet structure or the interpretation of the jet.

In my thesis, I utilise the anti-$k_{\mathrm{T}}$ algorithm for jet reconstruction [62]. It has the advantage of pulling soft, low-$p_{\mathrm{T}}$ particles toward high-$p_{\mathrm{T}}$ particles due to its inverse dependence on $p_{\mathrm{T}}$. This results in jets with approximately circular shape in the $y - \phi$ plane, as illustrated in Fig. 2.10.

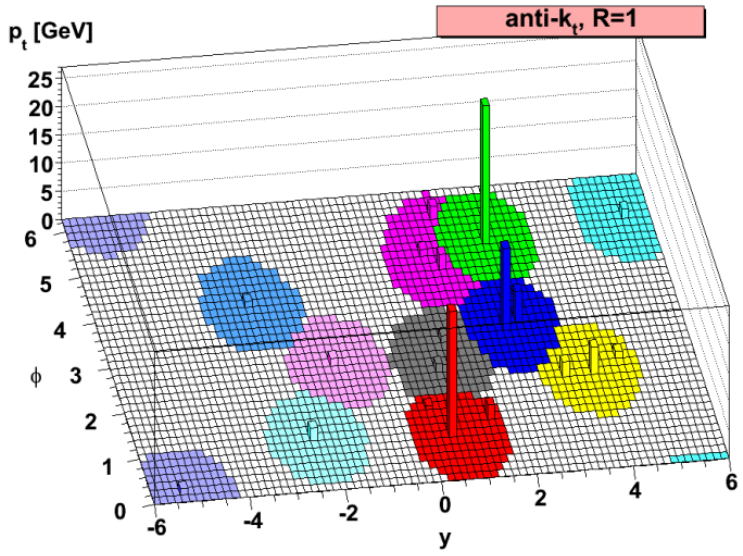


Figure 2.10: An example of jet clustering in a sample parton-level event. The resulting jets have a circular shape, with the highest-$p_{\mathrm{T}}$ particles located near the centre of the reconstructed jets [62].

The anti-$k_{\mathrm{T}}$ algorithm introduces a distance measure $d_{ij}$ between particles $i$ and $j$, defined as

$$d_{ij} = \min\left(\frac{1}{p_{Ti}^2}, \frac{1}{p_{Tj}^2}\right)\frac{\Delta R_{ij}^2}{R^2} \ , \tag{2.5}$$

where $\Delta R_{ij}^2 = (y_i - y_j)^2 + (\phi_i - \phi_j)^2$. Here, $p_{Ti}$, $y_i$, and $\phi_i$ are the transverse momentum, rapidity and azimuth of particle $i$, respectively. The parameter $R$ is

the jet resolution parameter. For isolated or high-energy jets, $R$ corresponds to the radius of the jet cone.

The jet reconstruction proceeds iteratively as follows:

- Distances $d_{ij}$ and $d_{iB}$ are computed for all particles or proto-jets, where $d_{iB}$ is the distance of particle $i$ from the beam and is defined as: $d_{iB} = \frac{1}{p_{Ti}^2}$.
- Next, the smallest distance, $\min(d_{iB}, d_{ij})$, is identified.
- If the smallest distance is $d_{ij}$, particles $i$ and $j$ are merged into a single proto-jet by summing their four-momenta.
- If the smallest distance is $d_{iB}$, the particle (or proto-jet) $i$ is declared a final jet and removed from the clustering process.

## 2.5 Thermodynamics from the final state

One of the most fundamental observables in high-energy collisions is the transverse momentum distribution of hadrons. It offers valuable insights into the parton creation and hadronisation processes and the properties of QCD matter that may be produced in these reactions.

The soft, low-$p_{\mathrm{T}}$ part of hadron spectra is usually associated with particles stemming from thermal equilibrium. This part is well described by extensive thermodynamics using the Boltzmann – Gibbs statistics, characterised by the kinetic freeze-out temperature, which parametrises the exponential function [63, 64] in the form

$$f(E) \sim \exp\left(-\frac{E-\mu}{T}\right) , \tag{2.6}$$

where $\mu$ is the chemical potential and $T$ is the associated temperature. However, as we go toward higher transverse momenta, the fits already fail at relatively low transverse momentum values ($p_{\mathrm{T}} \gtrsim 3$ GeV). The hadron spectra in this energy

regime follow a power-law-tailed distribution, inherited from perturbative QCD hadron production [65].

It is possible to unify the low- and high-$p_{\mathrm{T}}$ parts of the spectra in a single description, but the statistical picture needs to be modified. It has been shown that the non-extensive Tsallis – Pareto family of distributions, derived from the generalisation of the traditional Boltzmann – Gibbs entropy, successfully unites the low- and high-$p_{\mathrm{T}}$ parts of the spectrum [66–68]. The Tsallis – Pareto distribution can be written as

$$f(E, q, T, \mu) = \left[1 + \frac{q-1}{T}(E - \mu)\right]^{-\frac{1}{q-1}} , \tag{2.7}$$

where $T$ is the Tsallis temperature that follows the non-extensive statistics, while $q$ is the non-extensivity parameter. The Tsallis – Pareto distribution reduces to the Boltzmann – Gibbs distribution in the $q \to 1$ limit. The Tsallis form of hadron distribution leads to the following invariant transverse momentum distribution:

$$\left.\frac{\mathrm{d}^2N}{2\pi p_{\mathrm{T}}\mathrm{d}p_{\mathrm{T}}\mathrm{d}y}\right|_{y\approx 0} = Am_{\mathrm{T}}\left[1 + \frac{q-1}{T}(m_{\mathrm{T}} - \mu)\right]^{-\frac{q}{q-1}} , \tag{2.8}$$

where $A = gV\frac{1}{(2\pi)^3}$ is a normalisation factor with $g$ being the degeneracy factor for the given type of degrees of freedom and $V$ denoting the volume of the system, and $m_T = \sqrt{p_{\mathrm{T}}^2 + m^2}$. In the mid-rapidity limit ($y \approx 0$), the energy of a light particle is $E \approx m_{\mathrm{T}}$, while for the relativistic case the chemical potential is approximated as the rest mass of a given hadron, $\mu \approx m$. This is a theoretically motivated [69, 70] pragmatic choice supported by data-driven studies [71]. It has been shown in several recent studies that various parametrisations of Tsallis – Pareto distributions fit well to the measured data from RHIC to LHC energies [65, 66, 70–78].

While thermal equilibrium is often implicitly assumed in heavy-ion collisions, it is debated whether it can form [78, 79], and it is even less likely to be encountered in small collision systems. Fortunately, this assumption is not necessary for

understanding the observed patterns of the final state [80]. The non-extensive statistical framework can be applied to small as well as rapidly evolving systems without requiring thermal equilibrium [81].

The Tsallis – Pareto-distributed transverse momentum leads to a negative binomial distribution of the total charged hadron multiplicity in events, which is supported by data [82–84]. This allows to define the Tsallis parameter $T$ by the (one-dimensional, extremely relativistic) equipartition, and to relate the $q$ parameter to the scaled variance of the produced particle number [75, 85–87]:

$$T = \frac{E}{\langle n \rangle}, \tag{2.9}$$

$$q = 1 - \frac{1}{\langle n \rangle} + \frac{\Delta n^2}{\langle n \rangle^2}. \tag{2.10}$$

By combining the above equations, one arrives at an energy-dependent linear correlation between the Tsallis parameters,

$$T = E(\delta^2 - (q-1)), \tag{2.11}$$

where the relative size of multiplicity fluctuations $\delta^2 := \frac{\Delta n^2}{\langle n \rangle^2}$ is assumed to be constant.

# Chapter 3

# Heavy-flavour production in connection to the underlying event

Multiplicity-dependent measurements of heavy-flavour hadrons provide means to investigate the interplay between hard and soft QCD processes. By studying heavy-flavour production as a function of event multiplicity and underlying event activity, one can characterise the role of MPI in particle production and its dependence on event properties.

Measurements of unidentified hadron yields have shown that the number of particles produced in connection with the underlying event is almost independent of the transverse momentum scale of the hard leading process [58, 88]. However, identified heavy-flavour probes with their production mechanisms linked to the hard process may show such dependence and, therefore, serve as a tool to test the connection between the leading process and the underlying event.

This chapter details a study of heavy-flavour production as a function of the transverse event activity classifier $R_{\mathrm{T}}$ in simulated proton–proton collisions at $\sqrt{s} = 13$ TeV. The main results have been published in Ref. [89].

To generate heavy-flavour distributions comparable to those observed in particle accelerators, I used PYTHIA 8 simulations with the Monash tune [44] and soft QCD settings with the MPI-based colour-reconnection scheme during the parametrisation of the simulation. These settings are intended to represent the total cross section of hadron collisions with inelastic events, including diffractive topologies to account for the contamination of experimental minimum-bias samples. I simulated a total of 1 billion pp collisions to achieve an acceptable level of statistical uncertainty.

Besides the goals outlined above, the current study also served to evaluate the feasibility of such a measurement with existing detector systems. Therefore, I reproduced the capabilities of the ALICE experiment at CERN by considering only charged final-state hadrons generated by PYTHIA 8 within the midrapidity window $|\eta| < 0.8$ and above the transverse-momentum threshold of $p_{\mathrm{T}} = 0.15$ GeV/$c$. Final-state particles were defined as those with a lifetime $c\tau > 10$ mm, as such particles can be tracked in the detector. This approach ensured that the results would later be comparable with measurements.

## 3.1 Event triggering with hadrons and jets

As the first part of my study, I compared the results from my simulations to the trends observed by the ALICE experiment [58] for the distributions of charged-particle multiplicity in three azimuthal regions – toward, away, and transverse – in dependence on the transverse momentum of the leading particle, $p_{\mathrm{T}}^{\mathrm{leading}}$. The highest-$p_{\mathrm{T}}$ (leading) particle is often called the trigger particle when it is used to select events. This terminology is also used in the current thesis. However, it should not be mistaken for the experimental concept of a trigger that serves as a start signal for data taking. The ALICE measurements are shown together with my simulations in the left panel of Fig. 3.1. PYTHIA 8 closely reproduces the experimental results, indicating that the simulation parameters were chosen ap-

propriately to match the experimental behaviour and provide a reliable reference for future measurements. Additionally, the simulations show that the multiplicity in the transverse region saturates for $p_{\mathrm{T}}^{\mathrm{leading}} \gtrsim 5$ GeV/$c$, consistent with the behaviour of the underlying event observed in the experiment.

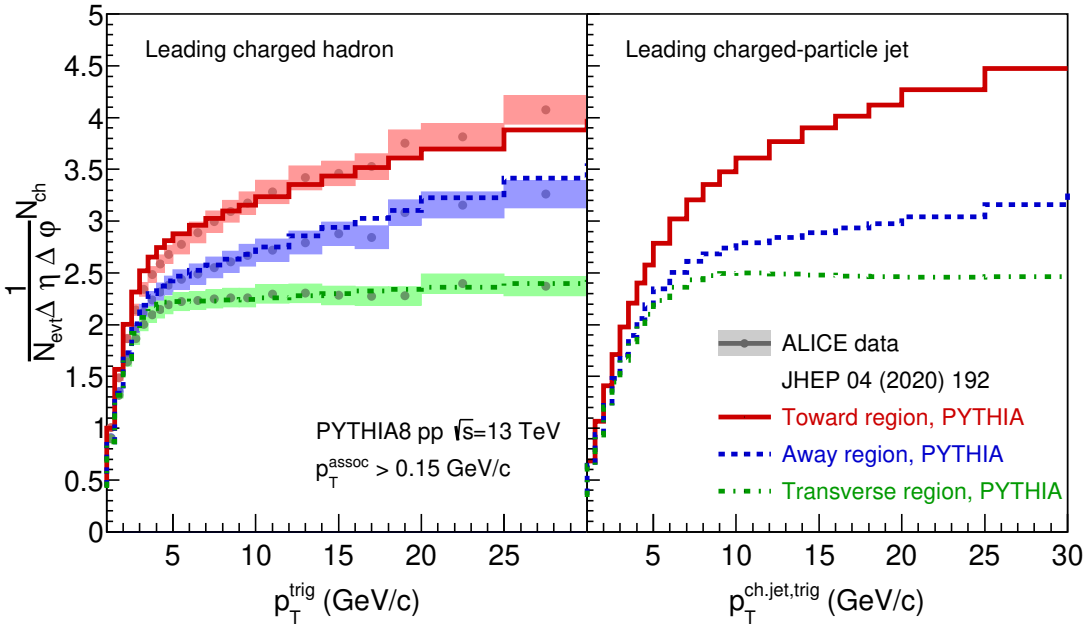


Figure 3.1: Charged-hadron multiplicity distributions in toward, away, and transverse regions as a function of the transverse-momentum of leading particle, $p_{\mathrm{T}}^{\mathrm{leading}}$ (left) and leading jet, $p_{\mathrm{T}}^{\mathrm{ch.jet,trig}}$ (right). The simulated distributions on the left panel are compared to the results from the ALICE experiment [58].

As heavy-flavour hadrons have different fragmentation properties compared to light flavour, using trigger hadrons does not allow for a bias-free comparison between heavy and light-flavour production, especially in the toward and away regions. For this reason, I suggested reconstructing charged-particle jets in events and associating the leading process with the highest-momentum jet. This allows for retaining the connection between the leading process and the heavy-flavour particle created in association with it. Moreover, by defining the leading process through reconstructed charged-particle jets, the results with different probes can be directly compared.

The jet reconstruction was performed with the anti-$k_{\mathrm{T}}$ algorithm [62] using the FastJet package [90] with a resolution parameter $R = 0.4$. Note that the choice of the resolution parameter is always a pragmatic trade-off. If $R$ is too small, a significant part of radiation may be lost. On the other hand, by increasing $R$, the jets pick up more background, and the effective detector acceptance will also be reduced. The choice of $R = 0.4$ was guided by several inclusive and heavy-flavour jet analyses [91, 92]. Similarly to the hadron-trigger case, the jets were required to be fully contained within the pseudorapidity region of $|\eta| < 0.8$. The jet containing particles with the highest sum of transverse momenta was considered the leading jet, and the direction of the leading process was defined to coincide with the direction of the leading jet.

The charged-particle multiplicity in the three azimuthal regions as a function of the transverse momentum of the leading jet, $p_{\mathrm{T}}^{\mathrm{ch.jet,trig}}$, is presented in the right panel of Fig. 3.1. The behaviour observed for the leading charged hadron is qualitatively reproduced for leading jets. However, the plateau region now begins at $p_{\mathrm{T}}^{\mathrm{ch.jet,trig}} \approx 10$ GeV/$c$. This shift occurs because the hardest hadron in the jet carries only a fraction of the transverse momentum of the fragmented jet.

Additionally, I classified jets based on the flavour of the initiating parton. Charm and beauty jets were defined as those containing the respective heavy quark within the jet cone, while light jets were identified as those with no heavy-flavour quark in the cone, indicating initiation by a gluon or an up, down, or strange quark. This classification enabled further categorisation of events and facilitated the derivation of new insights into the behaviour of heavy-flavour hadrons produced in such events. Note that with this method, jets that contain a late gluon splitting into a heavy-flavour quark pair are also categorised as heavy-flavour jets.

## 3.2 Comparison of $R_{\mathrm{T}}$ definitions

To characterise the underlying event using the transverse activity classifier $R_{\mathrm{T}}$, the average charged-particle multiplicity in the transverse region must be determined for each generated event. The $R_{\mathrm{T}}$ value depends on the trigger condition, particularly on the type of trigger (charged hadron or charged-particle jet). In the case of a charged-hadron trigger, at least one of the final-state charged hadrons must have a transverse momentum of $p_{\mathrm{T}}^{\mathrm{leading}} > 5$ GeV/$c$. This ensures that only events in the plateau region are studied, where the transverse side is not strongly influenced by hard processes. For events triggered by a jet, I used a $p_{\mathrm{T}}^{\mathrm{ch.jet,trig}} = 10$ GeV/$c$ threshold, corresponding to the start of the plateau in the transverse region for jet-triggered events (Fig. 3.1).

I generated a set of events with a charged-hadron trigger to obtain the average multiplicity in the transverse region, yielding $\langle N_{\mathrm{trans}} \rangle = 7.426$. With this value determined, all events with a $p_{\mathrm{T}}^{\mathrm{leading}} > 5$ GeV/$c$ trigger particle were categorised by the transverse activity $R_{\mathrm{T}}$. The $R_{\mathrm{T}}$-distribution of events triggered by a final-state hadron is shown in blue in Fig. 3.2. The distribution peaks around $R_{\mathrm{T}} = 1$ (the average transverse activity corresponding to the average multiplicity in the transverse region, $\langle N_{\mathrm{trans}} \rangle$). The upper limit was chosen to be $R_{\mathrm{T}} = 10$, where the $R_{\mathrm{T}}$ distribution is already negligible. I defined a total of four $R_{\mathrm{T}}$ classes: $0 < R_{\mathrm{T}} < 0.5$, $0.5 < R_{\mathrm{T}} < 1$ (below-average activity); $1 < R_{\mathrm{T}} < 2$, $2 < R_{\mathrm{T}} < 10$ (above-average activity). Additionally, an $R_{\mathrm{T}}$-integrated category, $0 < R_{\mathrm{T}} < 10$, was considered as a reference.

Since the transverse region within the plateau area is not expected to be influenced by the selection of the leading process, the average transverse multiplicity for jet-triggered events was assumed to be the same as for the leading hadron case: $\langle N_{\mathrm{trans}} \rangle = 7.426$. The $R_{\mathrm{T}}$-distribution of events with jet triggers is shown in red in Fig. 3.2. This distribution is more compact compared to that of hadron-triggered events, which can be attributed to the fact that inclusive-jet triggers

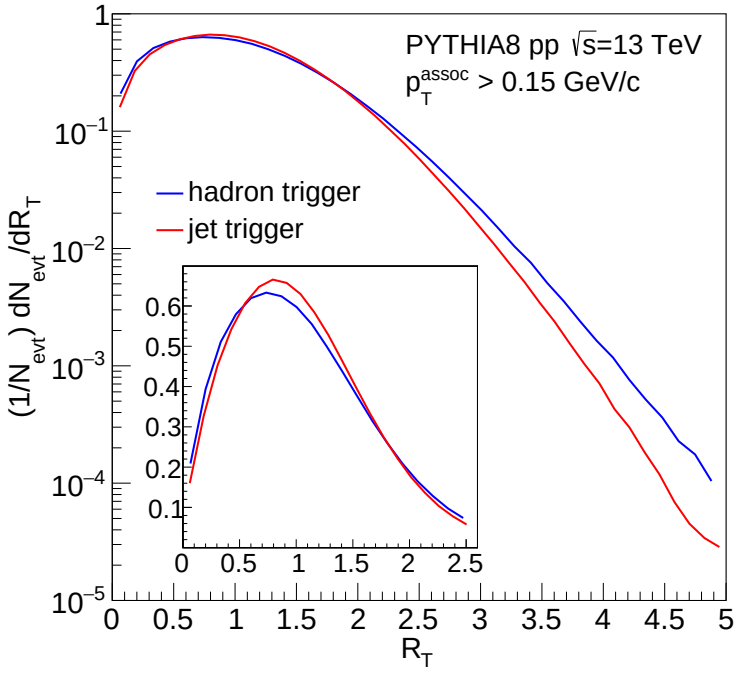


Figure 3.2: Distribution of the simulated events by their transverse activity $R_{\mathrm{T}}$ for events triggered with the leading hadrons (blue) and those triggered with inclusive jets (red). The insert shows the same distribution on a linear scale.

tend to select the leading process more reliably than charged-hadron triggers.

## 3.3 Triggering with charged hadrons

To study the production of heavy flavour as a function of transverse activity, I used the yields of D mesons ($\mathrm{D}^0$, $\mathrm{D}^+$ and $\mathrm{D}^{*+}$) and B mesons ($\mathrm{B}^0$, $\mathrm{B}^+$ and $\mathrm{B}^{*+}$), as well as of their charge conjugates. The yields were obtained for each of the four previously described $R_{\mathrm{T}}$ intervals, as well as for the $R_{\mathrm{T}}$-integrated interval.

Figure 3.3 shows the production of D and B mesons corresponding to each $R_{\mathrm{T}}$ interval in both hadron- and jet-triggered events. The distributions are presented for the full event as well as separately for the toward, transverse, and away regions. It can be observed, that the heavy-flavour production is larger in events with $R_{\mathrm{T}} > 1$ compared to the events with $R_{\mathrm{T}} < 1$, especially in the transverse region.

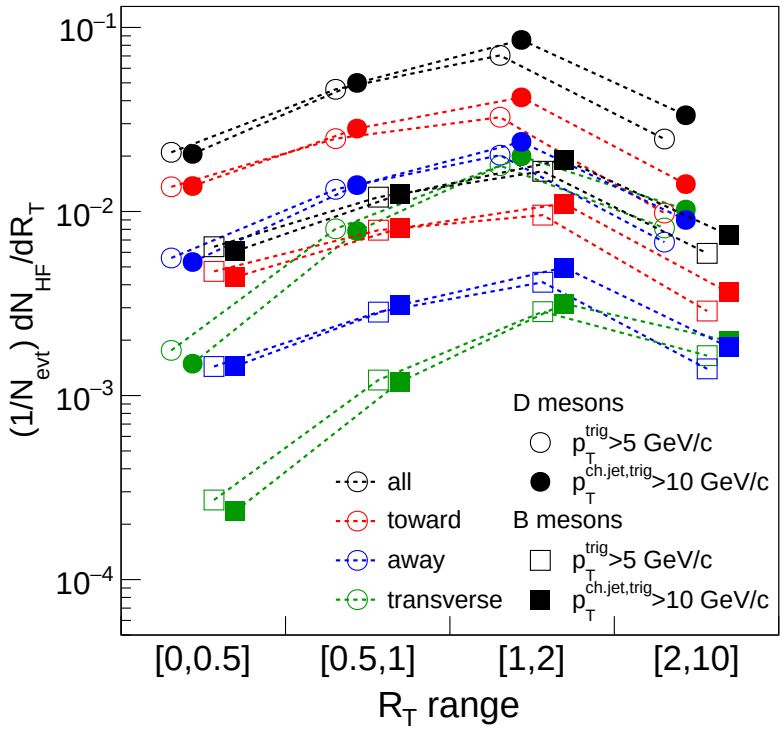


Figure 3.3: Distributions of heavy-flavour D and B hadrons across the different $R_{\mathrm{T}}$ intervals in hadron-triggered and jet-triggered events, shown for the full event and for the toward, transverse, and away regions separately. (The dashed lines are to guide the eye).

The normalised, per-trigger transverse momentum distributions of D mesons in the toward region are shown in the top left panel of Fig. 3.4. For a better comparison between the $R_{\mathrm{T}}$ intervals, the bottom left panel shows the ratios of the yields in each differential $R_{\mathrm{T}}$ class with respect to the $R_{\mathrm{T}}$-integrated yield. For D mesons with transverse momentum $p_{\mathrm{T}}^{\mathrm{D}} \gtrsim 8$ GeV/$c$, the $R_{\mathrm{T}}$ dependence of per-trigger yields is absent within the uncertainties. This is because these D mesons are produced in the hard scattering and are, therefore, not influenced by the underlying event. A slight increase in D-meson production is observed at high transverse momentum for $R_{\mathrm{T}} > 2$, likely due to the bias toward higher transverse event activity in events where multiple $c\bar{c}$ pairs are produced. Below the trigger threshold, for D mesons with transverse momentum $p_{\mathrm{T}}^{\mathrm{D}} < 5$ GeV/$c$,

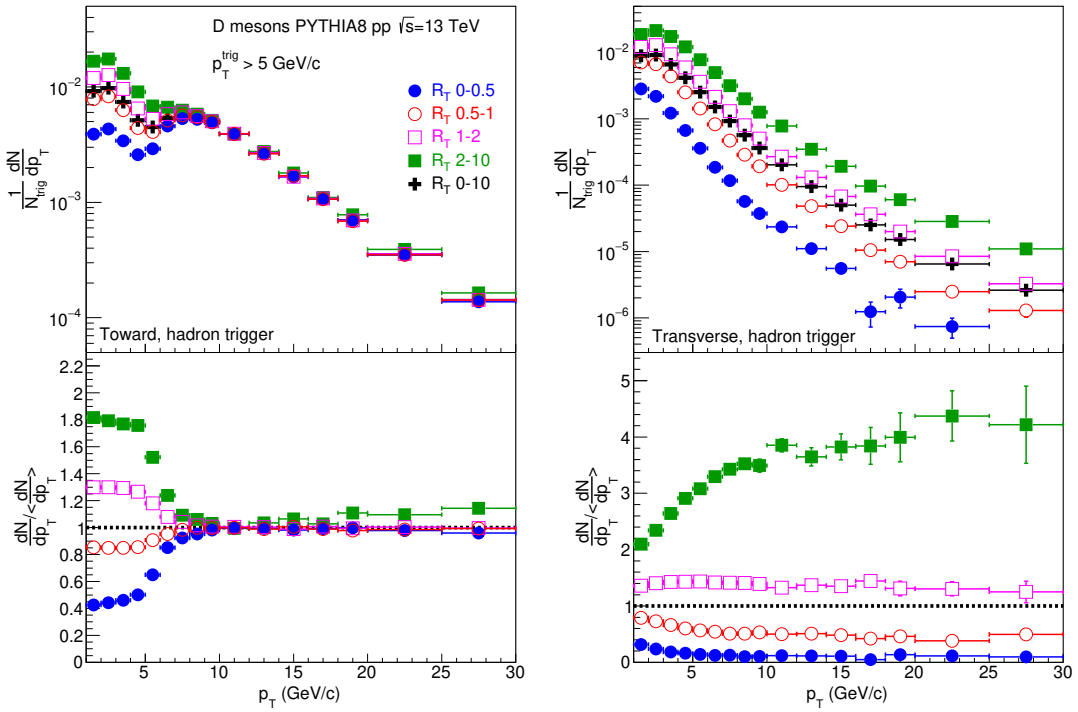


Figure 3.4: Per-trigger D-meson production in the toward region (left) and the transverse region (right) in events with a hadron trigger. The yields are presented for each of the $R_{\mathrm{T}}$ intervals (top), as well as the ratio to the $R_{\mathrm{T}}$-integrated yields (bottom).

a clear distinction between the different transverse-activity intervals is observed. Since the transverse momentum of these D mesons is below the trigger threshold requirement ($p_{\mathrm{T}}^{\mathrm{leading}} > 5$ GeV/$c$), these heavy-flavour hadrons are disconnected from the hard scattering selected by the trigger and are predominantly produced in secondary processes associated with the underlying event. The per-trigger yield of D mesons increases with transverse activity, while its transverse momentum dependence remains weak. As the D-meson transverse momentum increases above the $p_{\mathrm{T}}^{\mathrm{D}} = 5$ GeV/$c$ threshold, a trigger "turn-on" effect can be observed, showing a gradual transition between the $R_{\mathrm{T}}$-dependent and $R_{\mathrm{T}}$-independent regions of the D-meson spectra. This transition reflects the decay kinematics of D mesons and the changing probability that they originate from hard or soft processes. From simulations, I determined that about 16% of D mesons within the $5 < p_{\mathrm{T}}^{\mathrm{D}} <$

6 GeV/$c$ transverse momentum range produce a $p_{\mathrm{T}}^{\mathrm{leading}} > 5$ GeV/$c$ charged-hadron trigger upon decay. This fraction increases to 66% for D mesons with $7 < p_{\mathrm{T}}^{\mathrm{D}} < 8$ GeV/$c$ transverse momentum, and for $p_{\mathrm{T}}^{\mathrm{D}} > 10$ GeV/$c$, more than 97% of D mesons produce a $p_{\mathrm{T}}^{\mathrm{leading}} > 5$ GeV/$c$ trigger particle. In this case, almost all of D mesons produce a daughter particle with $p_{\mathrm{T}} > 5$ GeV/$c$; however, in approximately 3% of events, a harder particle is present in the same event.

The production of D mesons in the transverse region is shown in the right panel of Fig. 3.4. Unlike the behaviour observed in the toward region, in the transverse region the D-meson yields are separated into different $R_{\mathrm{T}}$ intervals across the entire $p_{\mathrm{T}}$ range. This suggests that heavy-flavour particle production in the transverse region is strongly influenced by the underlying event. At higher $p_{\mathrm{T}}$ values, the per-trigger D-meson production increases significantly with transverse activity.

I obtained similar results for B-meson production. Fig. 3.5 shows that in the toward region, B-meson production depends on $R_{\mathrm{T}}$ at low transverse momentum values, while the transverse activity dependence vanishes at higher $p_{\mathrm{T}}$. The per-trigger B-meson production in each of the $R_{\mathrm{T}}$ intervals, with respect to the $R_{\mathrm{T}}$-integrated production, is constant up to $p_{\mathrm{T}}^{\mathrm{B}} = 5$ GeV/$c$, after which all data tend towards unity. However, unlike the case of D mesons, for B mesons the transition between the $R_{\mathrm{T}}$-dependent and $R_{\mathrm{T}}$-independent parts of the spectrum is much smoother and occurs over a broader $p_{\mathrm{T}}$ range. A hint of an excess in the $2 < R_{\mathrm{T}} < 10$ class at high $p_{\mathrm{T}}$ values is also observed for the B mesons. This can be attributed to the effects of multiple $b\bar{b}$ pair production, similarly to the charm case.

## 3.4 Scale shift by heavy-flavour fragmentation

Simulations allow us not only to study the hadrons formed during fragmentation, but also to access the partonic level directly. Therefore, the next step in my

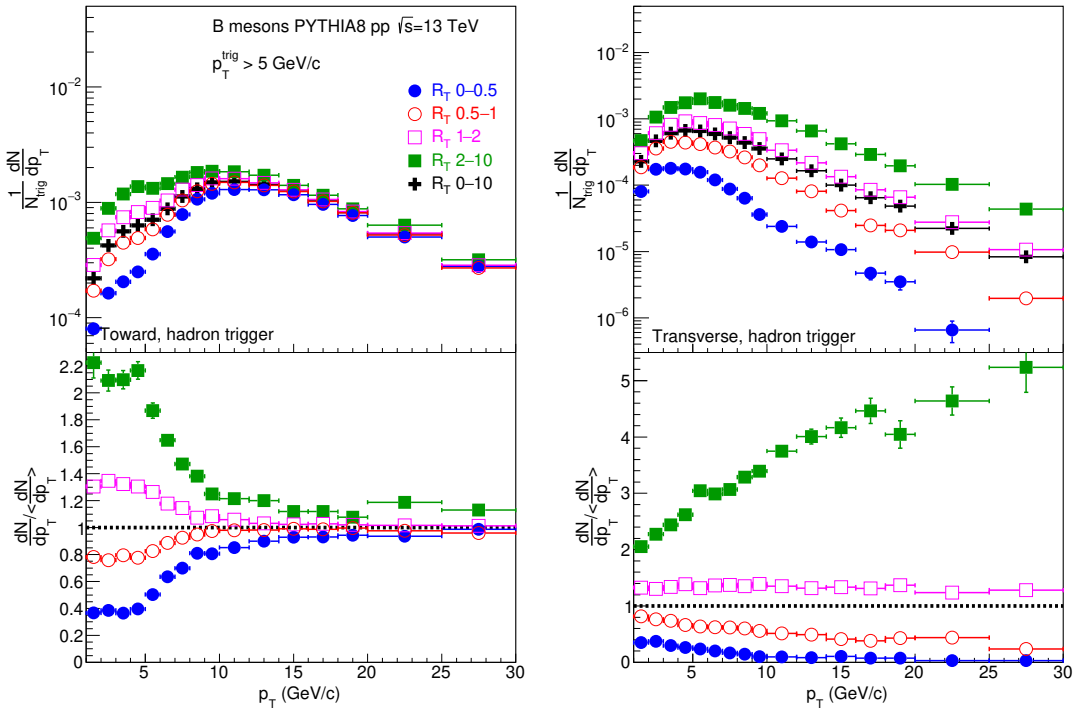


Figure 3.5: Per-trigger B-meson production in the toward region (left) and transverse region (right) in events with a hadron trigger. The yields are presented for each of the $R_{\mathrm{T}}$ intervals (top), as well as the ratio to the $R_{\mathrm{T}}$-integrated yields (bottom).

studies was to investigate the production of $c$ and $b$ quarks as a function of transverse activity in events with a trigger hadron having $p_{\mathrm{T}}^{\mathrm{leading}} > 5$ GeV/$c$. I considered the partons in the last stage just before hadronisation. By comparing heavy-flavour quark production to meson production, the effects of fragmentation can be directly investigated.

The upper and lower right panels of Fig. 3.6 show the production of $c$ and $b$ quarks, respectively, in the toward region in the four $R_{\mathrm{T}}$ intervals described in the previous sections. The upper and lower left panels show the production of D and B mesons in the toward region, as discussed previously. The qualitative trends exhibited by the quarks are similar to those observed for their corresponding mesons. For D mesons and $c$ quarks, the low-$p_{\mathrm{T}}$ part is relatively constant and $R_{\mathrm{T}}$-dependent, while the $R_{\mathrm{T}}$ dependence vanishes at high transverse momenta. A

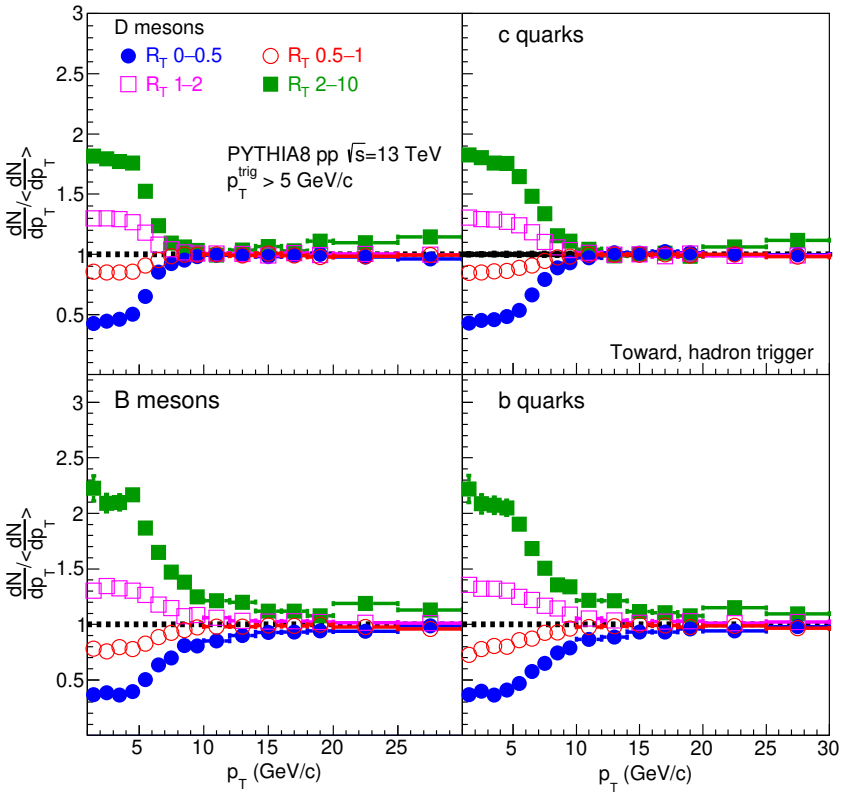


Figure 3.6: Per-trigger production ratios of D mesons (top left), $c$ quarks (top right), B mesons (bottom left) and $b$ quarks (bottom right) with charged-hadron triggers as a function of $p_{\mathrm{T}}$ for different $R_{\mathrm{T}}$ intervals in the toward region, over the $R_{\mathrm{T}}$-integrated per-trigger yield.

small increase in $c$-quark production is also observed in the highest $R_{\mathrm{T}}$ interval, similar to the behaviour seen for D mesons. In the case of B mesons and $b$ quarks, the trends are also very similar: a strong $R_{\mathrm{T}}$ dependence at low transverse momenta smoothly vanishes towards higher $p_{\mathrm{T}}$ values.

However, by comparing the differences in the presented results, one can observe a flavour-dependent shift in the momentum scale. For charm quarks, the trigger turn-on range is located about 40% higher in $p_{\mathrm{T}}$ than for hadrons, rising from $p_{\mathrm{T}} \approx 7$ GeV/$c$ for D mesons to $p_{\mathrm{T}} \approx 10$ GeV/$c$ for $c$ quarks. This shift is due to the change in momentum scale during the fragmentation of $c$ quarks into D mesons. For beauty quarks, the transition between underlying-event-dominated

and leading-process-dominated production occurs at $p_{\mathrm{T}} \approx 10-15$ GeV/$c$ for both B mesons and $b$ quarks. This is because $b$ quarks have a larger mass, leading to a larger dead-cone effect [30, 93], which results in harder fragmentation (with less parton radiation) of $b$ quarks into B mesons compared to $c$ quarks into D mesons.

## 3.5 Triggering with charged jets

When triggering an event with a final-state charged hadron, it is impossible to distinguish between leading processes initiated by heavy- and light-flavour jets. Therefore, the direct connection between heavy-flavour production and the underlying event cannot be unambiguously established. To better understand heavy-flavour production in dependence on the specifics of the hard scattering, I triggered the events with identified jets. As mentioned in Section 3.1, I defined three different types of jets: charm-jets (or c-jets, containing at least one charm quark), beauty-jets (or b-jets, containing at least one beauty quark) and light-jets (containing only $u$, $d$, and $s$ quarks, as well as gluons).

I evaluated the D-meson production in events triggered by charm-jets and light-jets with a total transverse momentum of at least $p_{\mathrm{T}}^{\mathrm{ch.jet,trig}} = 10$ GeV/$c$. The D-meson production in events with beauty-jet triggers was not considered due to the very limited number of events where both a beauty and a charm quark are produced in the toward region.

Figure 3.7 shows per-trigger D-meson production with c-jet triggers in the toward (top left) and transverse (bottom left) regions. In the c-jet triggered events, the dependence on transverse activity $R_{\mathrm{T}}$ is observed at low transverse momenta in the toward region. However, while in the case of hadron-triggered events the self-normalised D-meson yields were constant over this $p_{\mathrm{T}}$ region, here a stronger dependence on transverse momentum is seen. The overall resemblance between the D-meson production in hadron-triggered and c-jet-triggered events at low $p_{\mathrm{T}}$ suggests that charm production in the toward region is generally disconnected

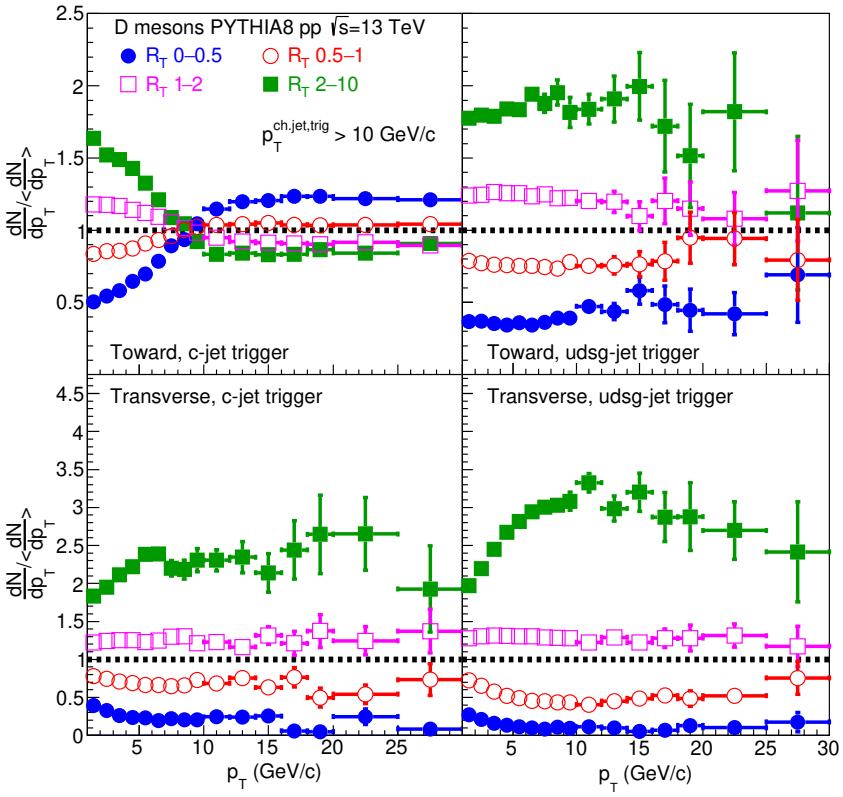


Figure 3.7: Per-trigger D-meson production ratios with charm-jet triggers (left panels) as well as light-jet triggers (right panels), as a function of $p_{\mathrm{T}}$ for different $R_{\mathrm{T}}$ classes in the toward (top panels) and transverse (bottom panels) regions, over the $R_{\mathrm{T}}$-integrated per-trigger yield.

from the leading process at these transverse momentum values.

There is, however, a different behaviour of the curves above the trigger threshold compared to the hadron-triggered case. Instead of the $R_{\mathrm{T}}$ dependence of D-meson production vanishing at higher $p_{\mathrm{T}}$, for c-jet-triggered events it is observed that lower underlying-event activity corresponds to a higher D-meson yield. A probable cause of this behaviour is the autocorrelation from wide-angle gluon-splitting processes. When a gluon splits into a $c\bar{c}$ pair, with one of the quarks falling into the toward and the other into the transverse region, the multiplicity in the transverse region increases. This leads to a decrease in the number of D mesons compared to the case where both jets fall into the toward region. This ef-

fect would not show up prominently in the charged-hadron-triggered case, where a more energetic hadron is expected from the jet that balances the splitted gluon.

In the transverse region, the production of D mesons in c-jet-triggered events is qualitatively similar to that in hadron-triggered events. There is a strong $R_{\mathrm{T}}$ dependence over the entire studied $p_{\mathrm{T}}$ range, with D-meson production increasing towards higher $R_{\mathrm{T}}$ values.

The right-hand panels of Fig. 3.7 show the per-trigger D-meson production ratios for light-jet-triggered events. The trends in the transverse region (lower right panel) are similar to those observed in all previously described cases: $R_{\mathrm{T}}$ dependence is seen over the entire $p_{\mathrm{T}}$ range, with higher D-meson production corresponding to higher transverse activity. The toward region (upper right panel), on the other hand, exhibits different behaviour: D-meson production in this region is $R_{\mathrm{T}}$-dependent even at high $p_{\mathrm{T}}$ values. The D-meson production here resembles that typically observed in the transverse region. This is because charm is excluded from the leading process, so all D mesons observed in the toward region are disconnected from it, similarly to what we observe in the transverse region. Therefore, by studying heavy-flavour production in the toward region in light-jet-triggered events, one can investigate the production of heavy flavour from the underlying event, even in a region dominated by hard processes. However, the statistics for this special case are limited.

Figure 3.8 shows the per-trigger B-meson production with b-jet triggers (left) and light-jet triggers (right) in the toward (top) and transverse (bottom) regions. The trends observed in B-meson production for events triggered by b-jets are generally comparable to those in D-meson production for c-jet-triggered events. An autocorrelation effect is present in the toward region for events with b-jet triggers, attributed to the wide-angle gluon splitting. B-meson production in the transverse region shows $R_{\mathrm{T}}$ dependence over the entire $p_{\mathrm{T}}$ range, with higher production observed in events with higher transverse activity. In light-jet-triggered events, B-meson production in the toward region becomes dependent on trans-

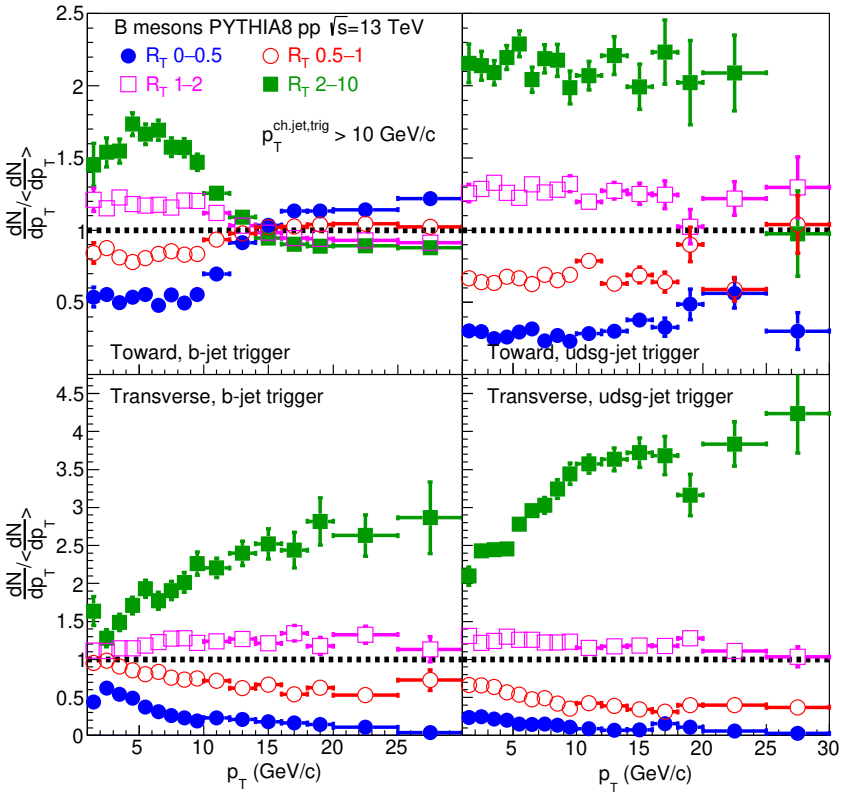


Figure 3.8: Per-trigger B-meson production ratios with beauty-jet triggers (left panels) as well as light-jet triggers (right panels), as a function of $p_{\mathrm{T}}$ for different $R_{\mathrm{T}}$ classes in the toward (top panels) and transverse (bottom panels) regions, over the $R_{\mathrm{T}}$-integrated per-trigger yield.

verse activity, although statistics are limited in the high-$p_{\mathrm{T}}$ region.

## 3.6 Summary

In the case of light-flavour hadrons, the CDF event classification is based on transverse event activity with respect to a leading hadron. This is not necessarily suitable in the case of heavy-flavour production, because heavy-flavour hadrons have different fragmentation characteristics. To make the results comparable across different probes, I suggested the utilisation of jet triggers for determining the leading process in an event. Events triggered with light- or heavy-flavour jets

retain the connection between the leading process and the heavy-flavour particle created in association with it, and bring more direct information on the underlying heavy-flavour production process.

I performed the analysis of heavy-flavour production as a function of the underlying event in pp collisions at $\sqrt{s} = 13$ TeV using simulations from PYTHIA 8. I observed that the production of low-transverse-momentum heavy flavour is dependent on the transverse event activity $R_{\mathrm{T}}$ in the toward region in events triggered with a charged hadron, hinting at the production of these particles in the UE processes. This dependence vanishes towards higher $p_{\mathrm{T}}$ values, as these heavy-flavour hadrons are predominantly produced in the hard processes disconnected from the UE. The same behaviour is exhibited by the heavy quarks, although at a slightly different momentum scale, which can be attributed to the loss of momentum during fragmentation. I showed that heavy-flavour hadron production in the transverse region is $R_{\mathrm{T}}$-dependent over the whole studied $p_{\mathrm{T}}$ range, signalling that heavy-flavour production in this region is strongly influenced by the underlying event.

The triggering of events with the identified jet allowed me to distinguish between hard processes initiated by heavy and light partons. The production of D and B mesons in the toward region in events triggered with charm- and beauty-jets, respectively, shows a similar behaviour at low-$p_{\mathrm{T}}$ to that observed in the charged-hadron-triggered events. At higher transverse momentum values, however, the $R_{\mathrm{T}}$-dependence persists because of the effect of wide-angle gluon splitting. Light-flavour jet triggers provide means to trigger on a hard process that is different from that of heavy-flavour production, therefore allowing for the underlying-event-dependent analysis of the connection between two hard processes. I showed that the heavy-flavour spectra in the toward region in events triggered with the light-parton jets are $R_{\mathrm{T}}$-dependent over the whole $p_{\mathrm{T}}$ range. I also showed that the behaviour of heavy-flavour production in the transverse region in events triggered with jets is qualitatively similar to that observed in

charged-hadron-triggered events, as this region is not influenced by the hard processes and is dominated by the underlying event, independently from the selection of leading process.

With the study described in this chapter, I provide the methodology for further experimental measurements of heavy-flavour production in connection to the underlying event and offer means for the interpretation of such results.

# Chapter 4

# Event-activity dependent $D^0$-meson production with the ALICE experiment

In this chapter, I apply the methodology developed in the previous chapter to measure the production of $D^0$ mesons as a function of transverse event activity in collisions registered by the ALICE experiment. The analysis is summarised in an ALICE Public Note [94]. The results will also be part of a journal article, that is currently under preparation within the collaboration.

## 4.1 Dataset

To study $D^0$-meson production as a function of underlying event activity $R_T$, I analysed data collected by the ALICE experiment during the Run 2 data-taking period (2016–2018). I studied proton–proton collision systems at a centre-of-mass energy of $\sqrt{s} = 13$ TeV. This data sample contains approximately 1.7 billion recorded minimum-bias events corresponding to an integrated luminosity $\mathcal{L}_{\text{int}} = 29.4\ \text{nb}^{-1}$. In addition to a minimum-bias trigger condition, a requirement

on the leading-particle transverse momentum $p_{\mathrm{T}}^{\mathrm{leading}} > 5$ GeV/$c$ was imposed to enable the categorisation of events by transverse-event activity $R_{\mathrm{T}}$. This condition reduced the number of analysed events down to 17 million. Due to this relatively small sample size, the analysis was performed only in the toward region.

Besides LHC collision data recorded by the experiment, ALICE also generated dedicated datasets using the PYTHIA 8 event generator. The final state of each event was then propagated through a model of the ALICE detector using GEANT 3 to achieve final states that can be directly compared to measurements.

## 4.2 Charged-particle track selection

A uniform azimuthal distribution of charged-particle tracks is desired for the current analysis due to the dependence of the $R_{\mathrm{T}}$ parameter on angular differences. In ALICE, the so-called global tracks (Fig. 4.1, in green) use information from both the Inner Tracking System (ITS) and the Time Projection Chamber (TPC). However, there are gaps in the azimuthal distribution of tracks, due to holes in the Silicon Pixel Detector (SPD) of the ITS. The raw data from the ITS detector are converted into clusters – groups of adjacent detector cells activated by the passage of a charged particle. However, the clustering algorithms fail in proximity to the SPD holes, as clusters cannot be reconstructed in these regions. To address this issue, a special track selection, referred to as complementary tracks, was implemented in the analysis. This selection compensates for the SPD holes by disregarding any clustering requirements for the ITS. The complementary tracks are shown in Fig. 4.1 in red. By combining the complementary tracks with the global track selection, I achieved a significantly more uniform azimuthal distribution of particle tracks. The residual structure causes a negligible systematic effect. The angular distribution of these so-called hybrid tracks is shown in blue in Fig. 4.1. The implementation of hybrid track selection enabled a much more precise classification of events based on their transverse activity, independent of

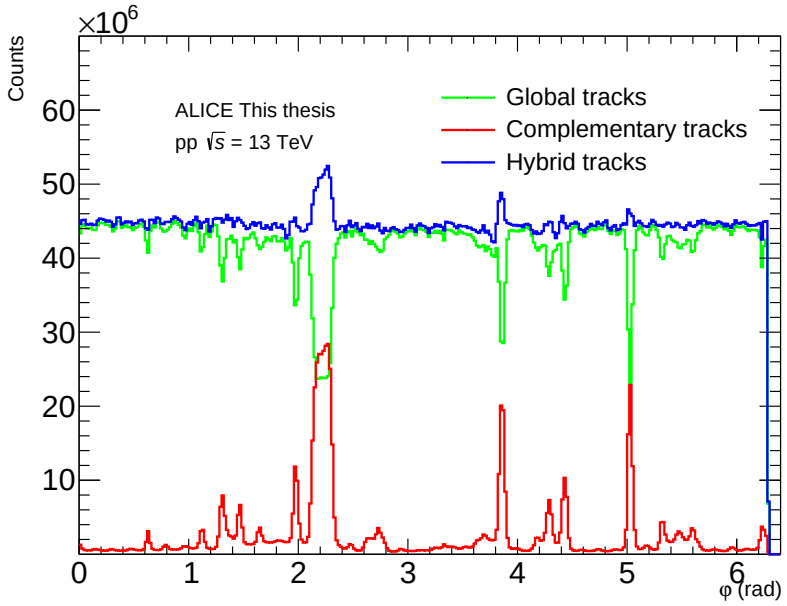


Figure 4.1: Azimuthal angle distribution of selected tracks. Green – global tracks, red – complementary tracks, blue – hybrid tracks.

the direction of outgoing particles.

## 4.3 Multiplicity in the transverse region

To define the $R_{\mathrm{T}}$ intervals in the data analysis, I examined the charged-particle multiplicity in the transverse region for all triggered events. The distribution of events by their transverse multiplicity is shown in the left panel of Fig. 4.2. The average transverse multiplicity of all events was determined to be $\langle N_{\mathrm{trans}} \rangle = 6.225$. As expected, this value differs from the $\langle N_{\mathrm{trans}} \rangle = 7.426$ obtained in PYTHIA 8 simulations that do not contain detector effects (Chapter 3). With this value established, the $R_{\mathrm{T}}$ parameter for each event can be calculated for $R_{\mathrm{T}}$-dependent studies. The $R_{\mathrm{T}}$ distribution is shown in the right panel of Fig. 4.2.

The distribution peaks slightly below 1 and becomes negligible towards high $R_{\mathrm{T}}$ values. Similarly to the studies in Chapter 3, I applied a technical cut-off at $R_{\mathrm{T}} = 10$, which didn't lead to loss of data. Given the available amount of data,

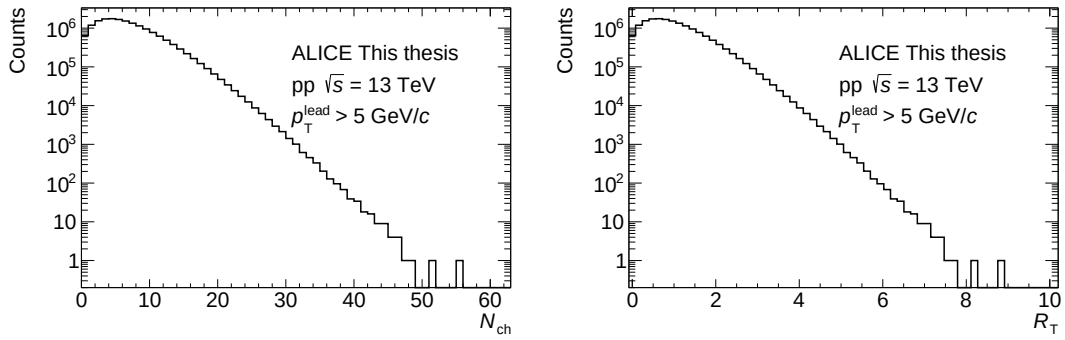


Figure 4.2: Charged-particle multiplicity distribution in the transverse region in triggered events (left) and distribution of selected events by their $R_{\mathrm{T}}$ (right).

I defined two $R_{\mathrm{T}}$ intervals for the analysis: below-average transverse activity, $0 < R_{\mathrm{T}} < 1$ (with a total of 10.05 million events); and above-average transverse activity, $1 < R_{\mathrm{T}} < 10$ (with a total of 6.81 million events).

This classification enabled a separate study of $\mathrm{D}^0$-meson production in events characterised by low and high underlying event activity.

## 4.4 Reconstruction of $\mathrm{D}^0$ mesons

The $\mathrm{D}^0$ and $\overline{\mathrm{D}^0}$ mesons were reconstructed via their $\mathrm{D}^0 \to K^-\pi^+$ and $\overline{\mathrm{D}^0} \to K^+\pi^-$ decays. These decay channels have a branching ratio (i.e., probability) of $3.89 \pm 0.04\%$ [95].

Charged kaons and pions are identified using the TPC detector, which measures their specific energy loss, $\frac{\mathrm{d}E}{\mathrm{d}x}$, inside the detector volume. The particle identification capabilities of the TPC are illustrated in Fig. 4.3. The curves corresponding to different particle species follow the Bethe – Bloch formula. As shown, differentiation between particle species is more pronounced at low momenta. At higher momenta, however, the regions corresponding to different species start to overlap, making particle identification ambiguous. This can lead to the misidentification of pions and kaons and a contribution of the so-called reflected $\mathrm{D}^0$ mesons,

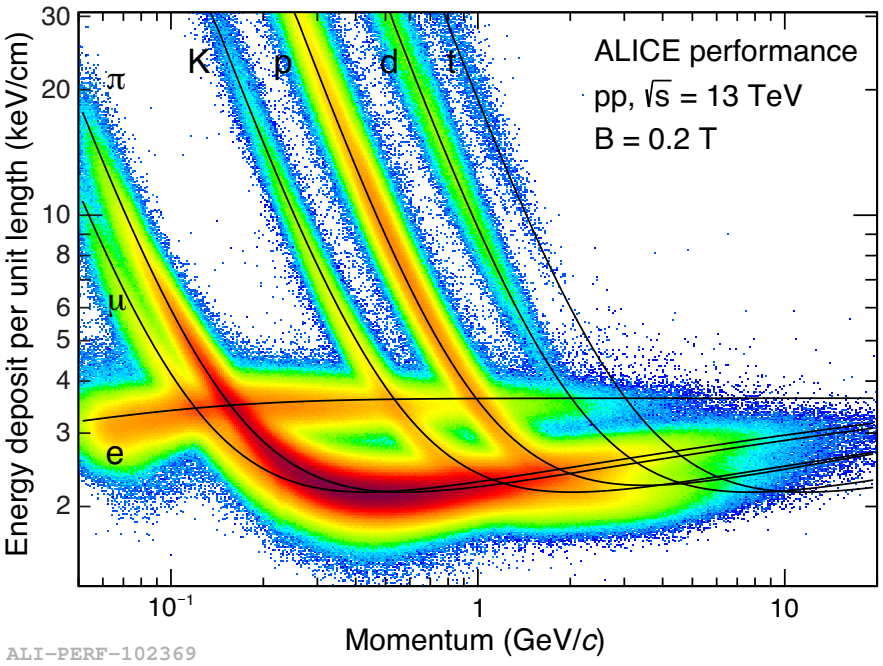


Figure 4.3: Energy deposit versus momentum measured with the ALICE TPC at magnetic field of 0.2 T and $\sqrt{s} = 13$ TeV. The black curves represent calculations for different particles using the Bethe – Bloch formula.

for which a decay kaon is identified as a pion and vice versa. In my analysis, a $3\sigma$ compatibility cut was applied to the difference between the measured and expected signals for the particle in the $p_{\mathrm{T}}$-dependent normalised distributions.

To identify kaon-pion pairs originating from a $\mathrm{D}^0$-meson candidate, a set of topological selections was applied. Firstly, the total invariant mass of the kaon-pion system was required to fall into a reasonable range of the $\mathrm{D}^0$-meson mass. In my analysis, the maximum allowed deviation was 400 MeV/$c^2$. Additionally, pions and kaons were required to have a transverse momentum above a certain threshold to exclude softly produced partons. I applied a threshold of $p_{\mathrm{T}} = 0.7$ GeV/$c$.

If a pion and a kaon are expected to originate from the same decay, the closest distance of approach (DCA) of their extended trajectories should be sufficiently small. In my study, the DCA was constrained to be no larger than 0.03 cm. By extrapolating particle tracks backwards, it is possible to calculate their impact

parameter with respect to the primary vertex (see Fig. 4.4). The impact param-

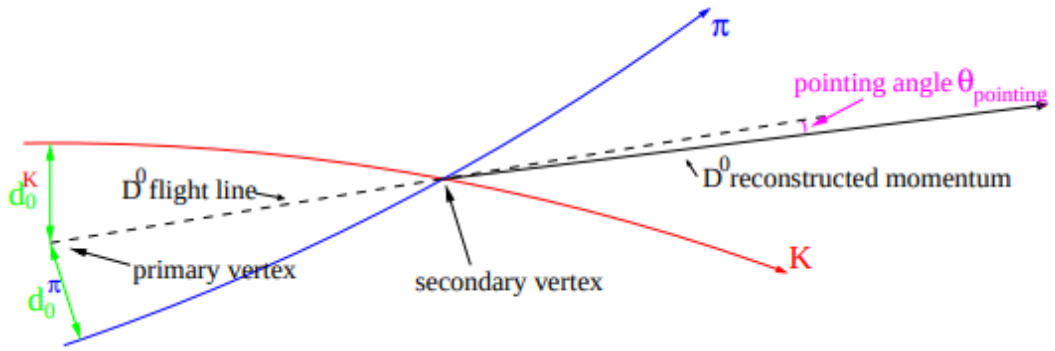


Figure 4.4: Schematics of a $D^0$-meson reconstruction.

eter was restricted to not exceed 1 mm. Additionally, a constraint was placed on the product of the impact parameters of the pion and the kaon in each candidate pair. These constraints are summarised in Table 4.1 (negative values arise when the two tracks pass on different sides of the primary vertex).

Further constraints were applied to the direction of flight of $D^0$-meson candidates. Regions, where $D^0$-meson production is suppressed, were excluded to reduce the combinatorial background. This was achieved by requiring the cosine of the $D^0$-meson's initial flight line direction in the centre-of-mass frame of the collision ($\cos\theta^*$) to remain below a specified upper limit. Lastly, the pointing angle ($\theta_{\mathrm{p}}$) – the angle between the reconstructed $D^0$-meson flight line and its expected flight line (connecting the primary and secondary vertices) – was required to be small. The selected $D^0$ candidates are sorted into five $p_{\mathrm{T}}^{\mathrm{D}^0}$ ranges: 2–5, 5–8, 8–12, 12–18, and 18–24 (GeV/$c$). All topological selections for $D^0$-meson candidates with various transverse momenta are motivated by the previous ALICE analyses [96, 97], and are detailed in Table 4.1.

| $p_{\mathrm{T}}^{\mathrm{D}^0}$ [GeV/$c$] | 2–3 | 3–4 | 4–7 | 7–8 | 8–12 | 12–16 | 16–24 |
|---|---|---|---|---|---|---|---|
| $\lvert M - M_{D^0}\rvert$ [GeV/$c^2$] | <0.4 | <0.4 | <0.4 | <0.4 | <0.4 | <0.4 | <0.4 |
| DCA [cm] | <0.03 | <0.03 | <0.03 | <0.03 | <0.03 | <0.03 | <0.03 |
| $\cos\theta^*$ | <0.8 | <0.8 | <0.8 | <0.8 | <0.9 | <1.0 | <1.0 |
| $p_{\mathrm{T}}$ (K) [GeV/$c$] | >0.7 | >0.7 | >0.7 | >0.7 | >0.7 | >0.7 | >0.7 |
| $p_{\mathrm{T}}(\pi)$ [GeV/$c$] | >0.7 | >0.7 | >0.7 | >0.7 | >0.7 | >0.7 | >0.7 |
| $\lvert d_0\rvert$ (K) [cm] | <0.1 | <0.1 | <0.1 | <0.1 | <0.1 | <0.1 | <0.1 |
| $\lvert d_0\rvert(\pi)$ [cm] | <0.1 | <0.1 | <0.1 | <0.1 | <0.1 | <0.1 | <0.1 |
| $d_0 d_0$ [$\times 10^{-8}$ cm$^2$] | <−20000 | <−12000 | <−8000 | <−7000 | <−5000 | <10000 | – |
| $\cos\theta_p$ | >0.9 | >0.85 | >0.85 | >0.85 | >0.85 | >0.85 | >0.85 |

Table 4.1: Topological selection criteria for $\mathrm{D}^0$ mesons in different transverse-momentum intervals.

## 4.5 Raw yield extraction

The invariant-mass distributions of the selected $\mathrm{D}^0$ candidates are shown for the different $p_{\mathrm{T}}^{\mathrm{D}^0}$ intervals for below-average and above-average $R_{\mathrm{T}}$ categories, as well as for $R_{\mathrm{T}}$-integrated category in Figs. 4.5, 4.6, and 4.7, respectively. The selected $\mathrm{D}^0$ candidates still include a substantial combinatorial background from randomly associated pion-kaon pairs that pass the selections. For $\mathrm{D}^0$-meson candidates with $p_{\mathrm{T}}^{\mathrm{D}^0} < 2$ GeV/$c$, the combinatorial background was too high to extract a significant signal.

The K-$\pi$ invariant-mass distributions show a clear peak around the nominal rest mass value of the $\mathrm{D}^0$ meson (1.864 GeV/$c^2$). In order to determine the raw yield of the $\mathrm{D}^0$ mesons, the combinatorial background has to be subtracted. The background is fitted with the $\chi^2$ method using an exponential function on the sideband regions ($3\sigma$-$5\sigma$ range from the invariant mass peak), where the contribution from the signal is negligible. This fit is represented by the red curves in the figures. After subtracting the background, the remaining peak is fitted with a Gaussian (blue curve). The results of the invariant mass peak fits are shown in Table 4.2. All the peaks are significant, with significance values $S/\sqrt{S+B}$ over 6. As discussed earlier, the production of $\mathrm{D}^0$ mesons is largely suppressed at low $p_{\mathrm{T}}$, therefore the lowest significance values are observed in the

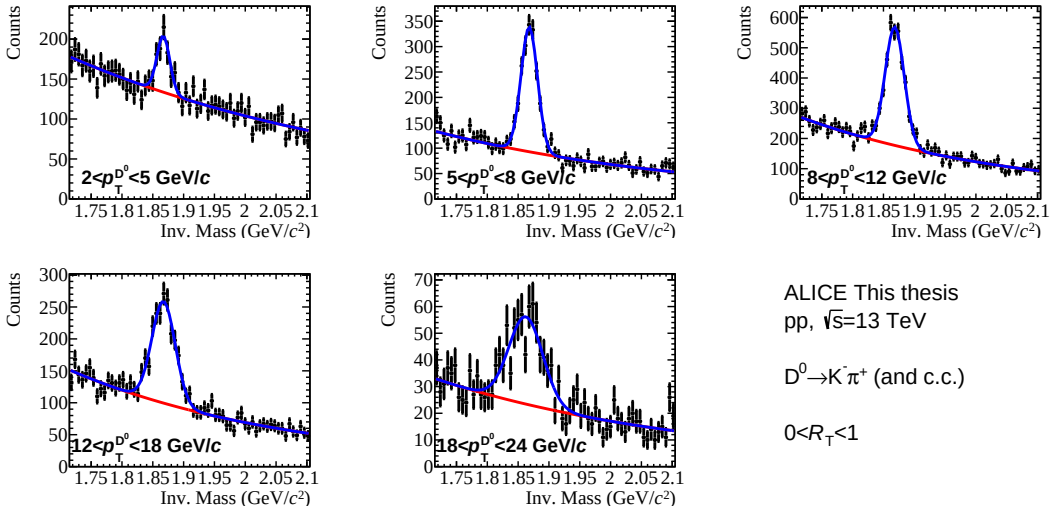


Figure 4.5: Invariant mass distributions of $\mathrm{D}^0$ meson candidates in the $0 < R_{\mathrm{T}} < 1$ region, for different $p_{\mathrm{T}}^{\mathrm{D}^0}$ ranges. The blue line represents the peak fit, and the red line represents the combinatorial background.

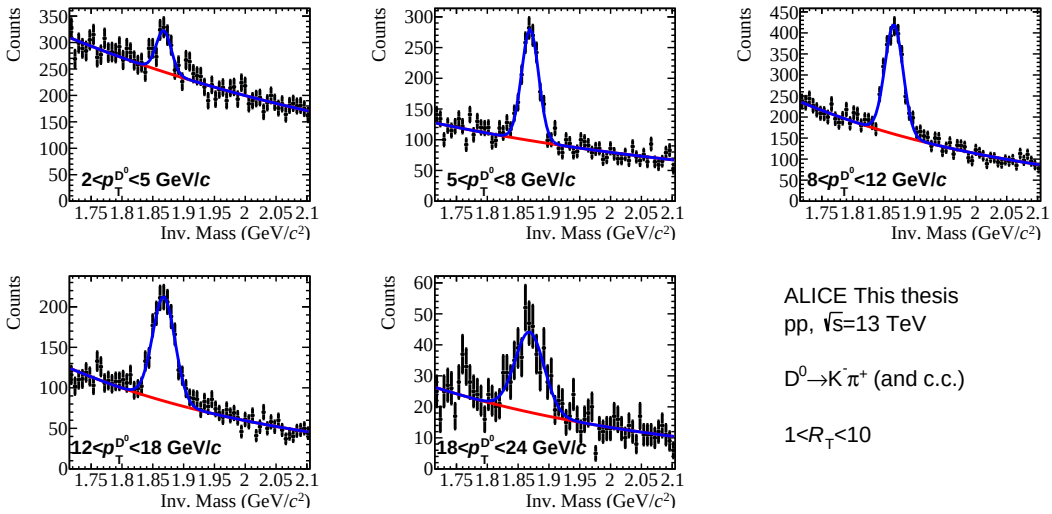


Figure 4.6: Invariant mass distributions of $\mathrm{D}^0$ meson candidates in the $1 < R_{\mathrm{T}} < 10$ region, for different $p_{\mathrm{T}}^{\mathrm{D}^0}$ ranges. The blue line represents the peak fit, and the red line represents the combinatorial background.

lowest transverse-momentum region.

I determined the raw yields by computing the integral between the background and signal fits. As a cross-check, I also applied the bin counting method. Both results agree within uncertainty.

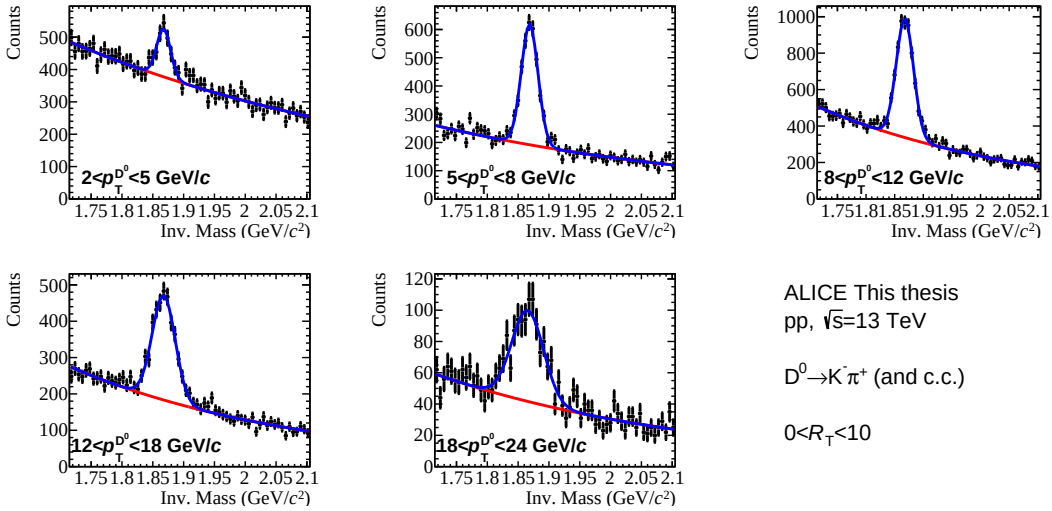


Figure 4.7: Invariant mass distributions for all $D^0$ candidates in different $p_T^{D^0}$ ranges. The blue line represents the peak fit, and the red line represents the combinatorial background.

| $R_T$ | $p_T^{D^0}$ [GeV/$c$] | M [GeV/$c^2$] | $\sigma$ [GeV/$c^2$] | Significance |
|---|---|---|---|---|
| 0–1 | 2–5 | 1.867±0.002 | 0.0105±0.0020 | 7.4±0.9 |
| | 5–8 | 1.868±0.001 | 0.0136±0.0006 | 26.7±0.7 |
| | 8–12 | 1.868±0.001 | 0.0154±0.0005 | 34.6±0.8 |
| | 12–18 | 1.867±0.001 | 0.0191±0.0011 | 22.3±0.9 |
| | 18–24 | 1.863±0.003 | 0.0279±0.0029 | 11.7±0.9 |
| 1–10 | 2–5 | 1.868±0.002 | 0.0122±0.0019 | 6.8±1.1 |
| | 5–8 | 1.870±0.001 | 0.0140±0.0008 | 21.1±0.8 |
| | 8–12 | 1.867±0.001 | 0.0153±0.0007 | 25.2±0.7 |
| | 12–18 | 1.868±0.001 | 0.0175±0.0013 | 19.3±0.9 |
| | 18–24 | 1.869±0.003 | 0.0242±0.0029 | 9.6±0.9 |
| 0–10 | 2–5 | 1.868±0.001 | 0.0108±0.0014 | 9.8±1.0 |
| | 5–8 | 1.869±0.000 | 0.0138±0.0004 | 33.9±0.8 |
| | 8–12 | 1.868±0.000 | 0.0148±0.0004 | 42.6±0.8 |
| | 12–18 | 1.868±0.001 | 0.0193±0.0008 | 29.5±0.9 |
| | 18–24 | 1.865±0.002 | 0.0259±0.0020 | 15.0±0.9 |

Table 4.2: Summary of the fitted parameters for the $D^0$ invariant mass peak together with the significance of the obtained fit.

## 4.6 Correction of the raw yields

The raw yields obtained from the invariant mass distributions do not account for various effects, such as the efficiency of particle detection, the geometrical acceptance of the ALICE detector, and the origin of the $D^0$ meson. Therefore, corrections must be applied to the raw yields to obtain the physical $D^0$ spectrum.

### 4.6.1 Acceptance and efficiency corrections

To account for the detection efficiency of the daughter particles, an efficiency correction has to be applied. Since the geometrical coverage provided by the detector is not complete, an acceptance correction is also needed. I determined these correction factors in a single step, by evaluating the $D^0$-meson production simulated with the PYTHIA 8 software, and then propagating the generated particles through a model of the detector system implemented in GEANT 3. Similarly to the data, the hybrid track selection was applied to the Monte Carlo data, resulting in similar spikes around 2.2 rad and 3.8 rad (Fig. 4.8). The average multiplicity in the transverse region was computed the same way as in data and yielded $\langle N_{\mathrm{trans}} \rangle = 4.802$.

To determine the fraction of $D^0$ mesons detected in the experiment, the number of $D^0$ candidates passing the same set of topological selections as for the data and later detected in the simulated detector environment was compared to the total number of generated $D^0$ mesons. The resulting fraction, called the acceptance-times-efficiency correction ($A \times \varepsilon$), compensates for tracking inefficiencies and the geometrical acceptance of the ALICE detector. This procedure was performed separately for prompt $D^0$ mesons (originating at the primary vertex) and for the feed-down $D^0$ mesons (decay products of $b$-hadrons). The prompt acceptance-times-efficiency correction was applied to the raw yields to compensate for the loss of signal, while the feed-down correction was later applied during the calculation of feed-down contribution.

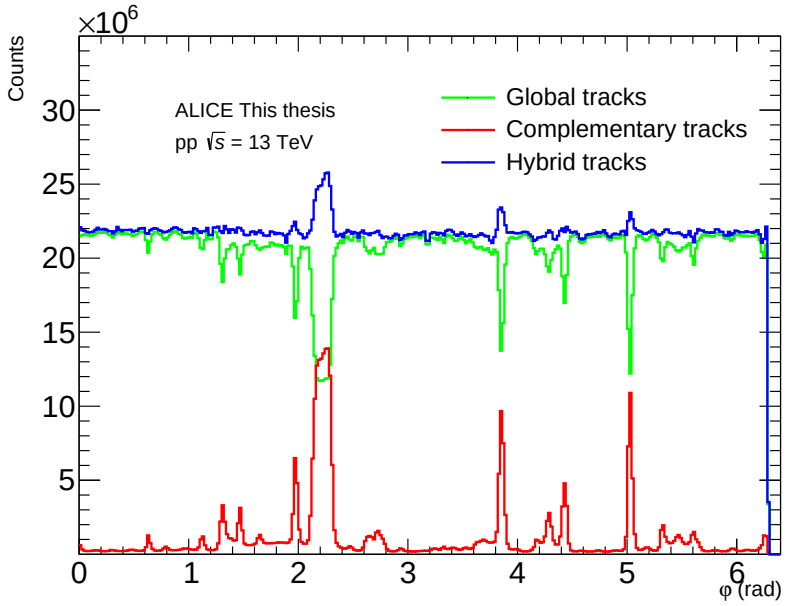


Figure 4.8: Azimuthal angle distribution of selected tracks in the PYTHIA 8 simulation. The global tracks are shown in green, complementary tracks are shown in red, and the hybrid tracks are shown in blue.

The A×$\varepsilon$ correction is shown in Fig. 4.9. It can be seen that the detection efficiency is independent of the transverse activity $R_{\mathrm{T}}$ for both prompt and feed-down $\mathrm{D}^0$ mesons. The values of the acceptance-times-efficiency correction for prompt $\mathrm{D}^0$ mesons increase with transverse momentum from 6% to 30%, which is lower than the values observed for feed-down $\mathrm{D}^0$ mesons, which range from 16% to 40%. This indicates that $\mathrm{D}^0$ mesons are not originating at the primary vertex, but they are rather coming from $b$-hadron decays, and are detected more efficiently compared to $\mathrm{D}^0$ mesons from charm hadronisation.

### 4.6.2 Feed-down correction

In order to study the production of $\mathrm{D}^0$ mesons, I had to exclude all yields originating from secondary decays of B mesons into D mesons. I calculated the fraction of prompt $\mathrm{D}^0$ mesons (originating from the primary vertex) based on the input from FONLL perturbative QCD calculations as

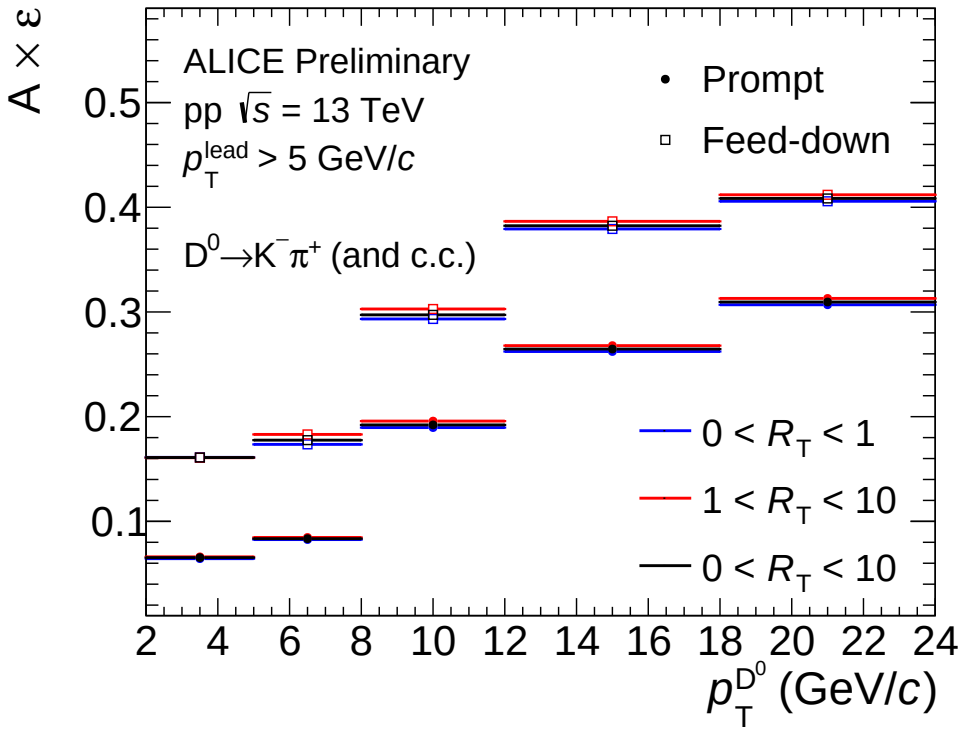


Figure 4.9: Acceptance-times-efficiency corrections for prompt and feed-down $\mathrm{D}^0$ mesons as a function of $p_{\mathrm{T}}^{\mathrm{D}^0}$ for the $R_{\mathrm{T}} < 1$ case in blue, $R_{\mathrm{T}} > 1$ case in red, as well as for the $R_{\mathrm{T}}$-integrated case in black.

$$f_{\mathrm{prompt}} = 1 - \left(\frac{\mathrm{d}^2\sigma}{\mathrm{d}y\mathrm{d}p_{\mathrm{T}}}\right)^{\mathrm{FONLL}}_{\mathrm{feed\text{-}down}} \cdot \frac{(\mathrm{A}\times\varepsilon)_{\mathrm{feed\text{-}down}} \cdot \Delta y \Delta p_{\mathrm{T}} \cdot \mathrm{BR} \cdot \mathcal{L}_{\mathrm{int}}}{N^{\mathrm{D_{raw}}}/2}\,, \qquad (4.1)$$

where $\left(\frac{\mathrm{d}^2\sigma}{\mathrm{d}y\mathrm{d}p_{\mathrm{T}}}\right)^{\mathrm{FONLL}}_{\mathrm{feed\text{-}down}}$ is the cross section of B mesons determined from the FONLL calculations with the respective branching ratios (BR) for decays into $\mathrm{D}^0$ mesons, $(\mathrm{A}\times\varepsilon)_{\mathrm{feed\text{-}down}}$ is the acceptance-times-efficiency correction for feed-down $\mathrm{D}^0$ mesons, $\Delta y$ is the rapidity window, $\Delta p_{\mathrm{T}}$ is the width of the transverse momentum interval, $\mathcal{L}_{\mathrm{int}}$ is the integrated luminosity, and $N^{\mathrm{D_{raw}}}$ is the raw yield obtained from the data. The factor of $1/2$ in the denominator is needed because the cross section is measured as an average of $\mathrm{D}^0$ and $\overline{\mathrm{D}^0}$. The integrated luminosity is calculated based on the inelastic pp cross section $\sigma_{\mathrm{inel}}$ at $\sqrt{s} = 13$ TeV centre-of-mass energy and the number of detected events as $\mathcal{L}_{\mathrm{int}} = \frac{N_{\mathrm{evt}}}{\sigma_{\mathrm{inel}}}$.

Because of the additional event trigger, which discards events with a leading particle having $p_{\mathrm{T}}^{\mathrm{leading}} < 5$ GeV/$c$, the FONLL-calculated B-meson cross section $\left(\frac{\mathrm{d}^2\sigma}{\mathrm{d}y\mathrm{d}p_{\mathrm{T}}}\right)^{\mathrm{FONLL}}_{\text{feed-down}}$ cannot be applied directly, as it is calculated for minimum bias events. To resolve this problem, I added additional factors to the equation above. First, the fraction of feed-down $\mathrm{D}^0$ mesons in the events satisfying the trigger condition had to be determined:

$$r_{\mathrm{trig}} = \frac{N^{\mathrm{D}^0_{\mathrm{feed-down}}}_{R_{\mathrm{T}(0-10)}}}{N^{\mathrm{D}^0_{\mathrm{feed-down}}}_{\mathrm{MB}}} \ , \tag{4.2}$$

where $N^{\mathrm{D}^0_{\mathrm{feed-down}}}_{R_{\mathrm{T}(0-10)}}$ denotes the number of feed-down $\mathrm{D}^0$ mesons in all the events with leading particle having $p_{\mathrm{T}}^{\mathrm{leading}} > 5$ GeV/$c$, while $N^{\mathrm{D}^0_{\mathrm{feed-down}}}_{\mathrm{all}}$ is the number of $\mathrm{D}^0$ mesons in the minimum-bias events. Furthermore, I had to account for the fact that feed-down $\mathrm{D}^0$ mesons are not produced uniformly among different $R_{\mathrm{T}}$ intervals. This can be accounted for with the factor:

$$r_{\mathrm{RT}} = \frac{N^{\mathrm{D}^0_{\mathrm{feed-down}}}_{R_{\mathrm{T}}}}{N^{\mathrm{D}^0_{\mathrm{feed-down}}}_{R_{\mathrm{T}(0-10)}}} \ . \tag{4.3}$$

Here, $N^{\mathrm{D}^0_{\mathrm{feed-down}}}_{R_{\mathrm{T}}}$ is the number of feed-down $\mathrm{D}^0$ mesons in a given $R_{\mathrm{T}}$ interval. By combining Eqs. (4.2) and (4.3), we arrive at a simple correction factor to be applied to the FONLL spectrum:

$$r = \frac{N^{\mathrm{D}^0_{\mathrm{feed-down}}}_{R_{\mathrm{T}}}}{N^{\mathrm{D}^0_{\mathrm{feed-down}}}_{\mathrm{MB}}} \ . \tag{4.4}$$

With this, the modified formula for calculating the fraction of prompt $\mathrm{D}^0$ mesons becomes

$$f_{\mathrm{prompt}} = 1 - \frac{N^{\mathrm{D}^0_{\mathrm{feed-down}}}_{R_{\mathrm{T}}}}{N^{\mathrm{D}^0_{\mathrm{feed-down}}}_{\mathrm{MB}}} \left(\frac{\mathrm{d}^2\sigma}{\mathrm{d}y\mathrm{d}p_{\mathrm{T}}}\right)^{\mathrm{FONLL}}_{\text{feed-down}} \cdot \frac{(\mathrm{A}\times\varepsilon)_{\text{feed-down}} \cdot \Delta y \Delta p_{\mathrm{T}} \cdot \mathrm{BR} \cdot L_{\mathrm{int}}}{N^{D_{\mathrm{raw}}}/2} \ . \tag{4.5}$$

I calculated the factor $r$ from Eq. (4.4) with PYTHIA 8 simulations. The resulting fractions are shown in Fig. 4.10. It can be seen that the production of

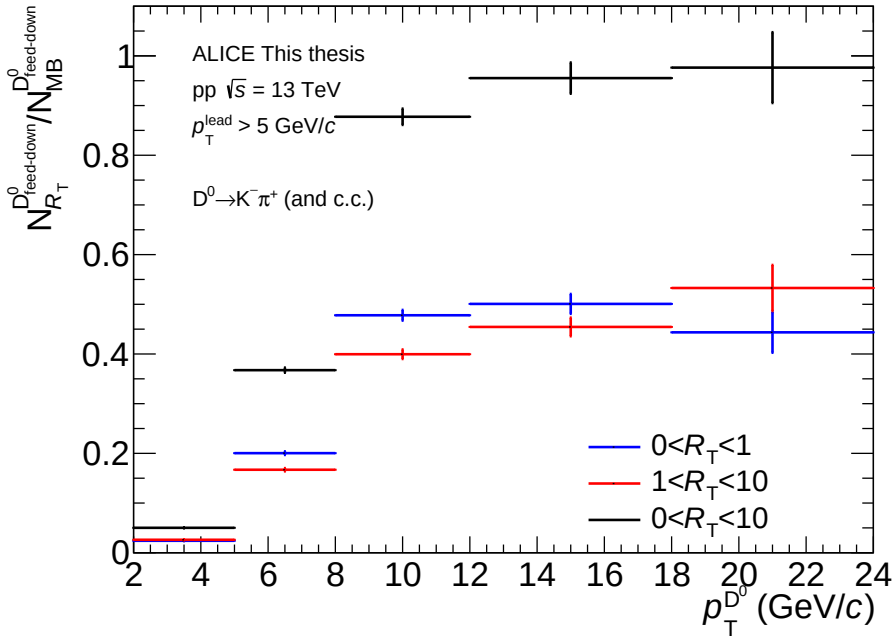


Figure 4.10: Ratio between the number of feed-down $D^0$ mesons in each of the studied $R_T$ intervals and the total number of feed-down $D^0$ mesons in the minimum-bias events simulated with PYTHIA 8.

feed-down $D^0$ mesons with transverse momentum below the trigger threshold is heavily suppressed. Starting from $p_T^{D^0} = 10$ GeV/$c$ upwards, however, almost all $D^0$ mesons are detected. This is due to them producing a daughter particle having a transverse momentum above $p_T = 5$ GeV/$c$ which triggers the event. Between $p_T^{D^0} = 5$ GeV/$c$ and $p_T^{D^0} = 10$ GeV/$c$, in order to trigger the event, the transverse momentum must be transferred unevenly between the $D^0$ daughters, with a larger discrepancy towards $D^0$ mesons with lower transverse momentum. Therefore, these $D^0$ mesons are still suppressed, but less so as we move towards higher $p_T^{D^0}$ values. Also, note that while trigger efficiencies in the $R_T$ bins of $0 < R_T < 1$ and $1 < R_T < 10$ are close to each other, there is still a distinguishable dependence on $R_T$. This also results in $R_T$ dependence of the feed-down correction.

The comparison between the original FONLL spectrum and the corrected spectrum is shown in Fig. 4.11 for the $0 < R_T < 10$ interval.

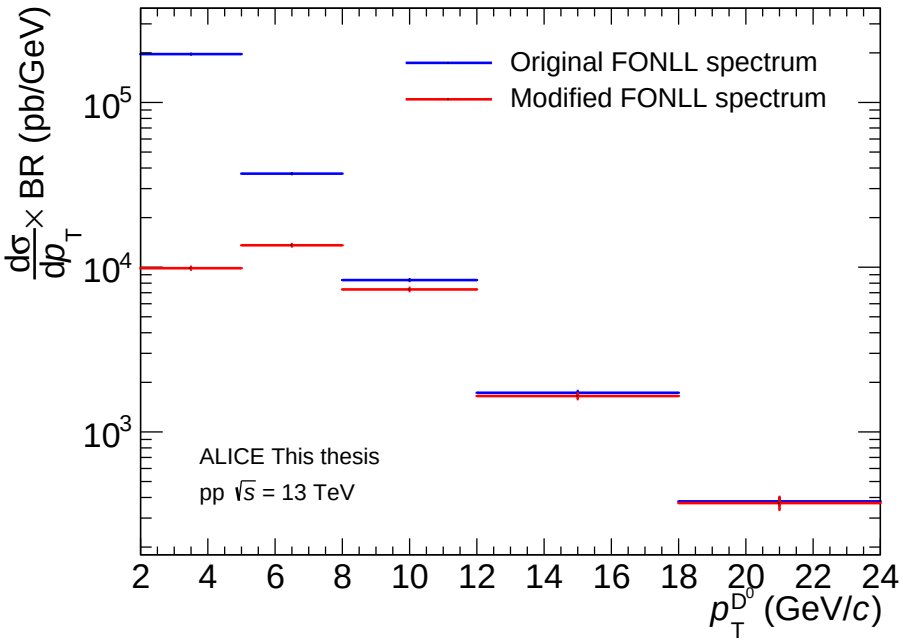


Figure 4.11: Comparison between the original FONLL spectrum for the minimum-bias events and the modified FONLL spectrum for the events with $p_{\mathrm{T}}^{\mathrm{leading}} > 5$ GeV/$c$ condition.

The fraction of prompt $\mathrm{D}^0$ mesons calculated in the analysis is summarised in Fig. 4.12. The raw yields are corrected with the central values of $f_{\mathrm{prompt}}$, while the statistical errors are inherited from the raw yield extraction. In the event sample considered in this analysis, the fraction of prompt $\mathrm{D}^0$ mesons with $p_{\mathrm{T}}^{\mathrm{D}^0} < 5$ GeV/$c$ is approximately 60%, significantly lower than what is obtained in the minimum-bias event sample. For $\mathrm{D}^0$ mesons with $p_{\mathrm{T}}^{\mathrm{D}^0} > 5$ GeV/$c$, the fraction is in the range of 85–90%, similar to other $\mathrm{D}^0$ measurements [96, 97].

## 4.7 Systematic uncertainties

In the analysis procedure described in the previous sections, the choice of parameters often played an important role. The final results may slightly depend on these parameters. These dependencies are accounted for as systematic uncer-

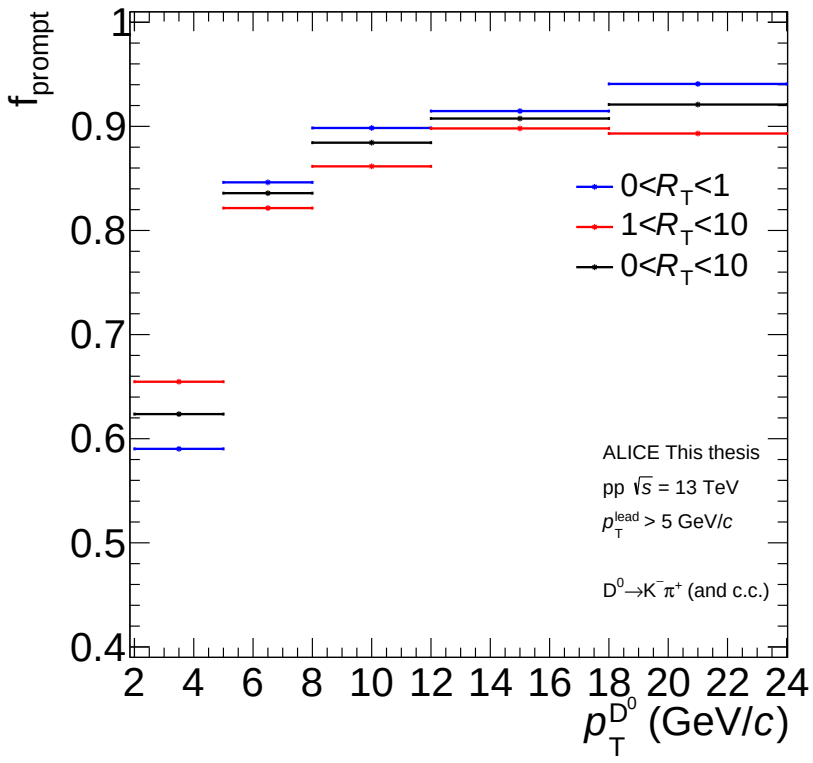


Figure 4.12: The fraction of prompt $D^0$ mesons in each of the $R_T$ intervals obtained in the analysis.

tainties. In the analysis, I considered several sources of systematic uncertainties, including detection and reconstruction efficiencies, data fitting stability, and the uncertainty from the simulated spectral shapes.

### 4.7.1 $D^0$ selection systematics

The systematic uncertainty of the reconstruction of $D^0$ candidates from their decay products originates from imperfections in the description of the $D^0$-meson kinematic properties, as well as from the detector resolution and alignment in the simulation. This systematic uncertainty was estimated by varying the parameters for the topological selections of $D^0$ mesons such that the resulting acceptance-times-efficiency correction varied by 5% and 10% (variations deemed sufficient in

previous ALICE analyses [97, 98] to test the stability of $D^0$ selection) in both the lower and higher directions relative to the values obtained in the analysis. This resulted in significant modification to the raw yields, signal-to-background ratios, and efficiencies. By applying less strict, looser constraints on the topological selection of $D^0$ candidates, I obtained two sets of results: "Looser1" with a 5% higher acceptance-times-efficiency correction and "Looser2" with a 10% higher value. Similarly, two sets were defined for tighter constraints: "Tighter1" corresponding to a 5% variation and "Tighter2" corresponding to a 10% variation. After defining the new sets of topological selections, I repeated the complete analysis (including extraction of raw yields and application of all corrections) and compared the deviation of the final results with respect to those obtained with the default selections. The systematic uncertainty was assigned separately for each point in the final results, based on the root mean square (RMS) of the four points coming from the four sets of cuts. Figure 4.13 shows the ratio between results with each set of modified topological selections and the results with the standard ones for $0 < R_{\mathrm{T}} < 1$ and $1 < R_{\mathrm{T}} < 10$.

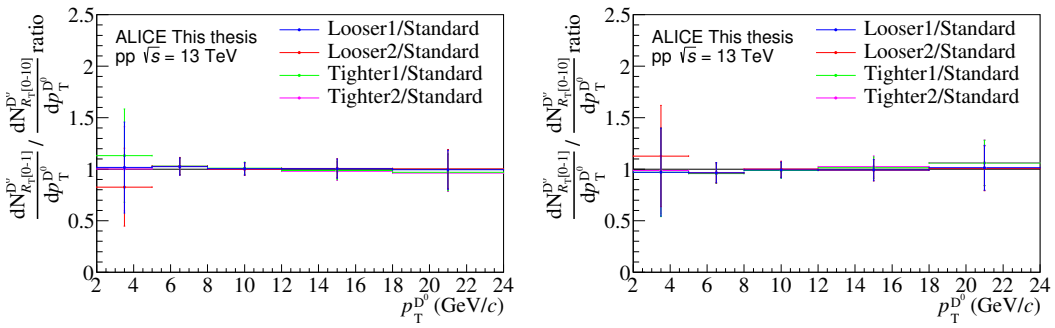


Figure 4.13: Ratio of the per-event $D^0$-meson yields with modified topological selections to the per-event $D^0$-meson yields with standard topological selections for events with $R_{\mathrm{T}} < 1$ (left) and $R_{\mathrm{T}} > 1$ (right).

The contribution of the $D^0$ selection systematic uncertainty was estimated to be in the range of 1–7%, depending on the transverse momentum of the $D^0$ and $R_{\mathrm{T}}$ of an event. The detailed list of assigned systematic uncertainty values is shown in Table 4.3. The highest uncertainty is observed in the lowest $p_{\mathrm{T}}^{\mathrm{D}^0}$ region,

| $p_{\mathrm{T}}^{\mathrm{D}^0}$ [GeV/$c$] | 2–5 | 5–8 | 8–12 | 12–18 | 18–24 |
|---|---|---|---|---|---|
| $R_{\mathrm{T}} < 1$ | 6% | 3% | 1% | 2% | 2% |
| $R_{\mathrm{T}} > 1$ | 7% | 4% | 1% | 2% | 2% |

Table 4.3: Assigned values of the systematic uncertainties connected to the $\mathrm{D}^0$ selection.

where, due to the presence of the trigger particle condition, the number of $\mathrm{D}^0$ mesons is significantly lower compared to the other $p_{\mathrm{T}}^{\mathrm{D}^0}$ regions. This results in higher sensitivity to the selection criteria of $\mathrm{D}^0$ candidates. In regions with higher $p_{\mathrm{T}}^{\mathrm{D}^0}$ values, the systematic uncertainty reaches a few percent at most.

### 4.7.2 Raw yield extraction systematics

The number of extracted $\mathrm{D}^0$ yields depends on the exact method of fitting the invariant mass distributions. Therefore, an additional systematic uncertainty was determined by varying the fit parameters and fit function shapes. The variations included changing the lower and upper bounds for the fits, merging several bins of the invariant mass histogram, and changing the background fitting function from exponential to a second-order polynomial. Additionally, one variation involved fixing the Gaussian width at the value obtained from the fits on $R_{\mathrm{T}}$-integrated invariant mass histograms. The summary of the varied parameters is presented in Table 4.4.

| Rebinning | 1 | **2** | 4 | |
|---|---|---|---|---|
| Lower mass limit | 1.68 | 1.70 | **1.72** | 1.74 |
| Upper mass limit | 2.08 | **2.10** | 2.12 | 2.14 |
| Width of Gaussian | **fixed** | released | | |
| Background fit | **Expo** | Pol2 | | |

Table 4.4: Variation of fitting parameters for the invariant mass distributions. Values used in the main analysis are written in bold.

All possible combinations of the fit settings were considered, resulting in a total of 192 trials for each of the $p_{\mathrm{T}}^{\mathrm{D}^0}$ and $R_{\mathrm{T}}$ regions. In each trial, the fitted $\mathrm{D}^0$ mass (centre of the Gaussian) and sigma (width of the Gaussian) values were checked to ensure they were within reasonable ranges (see Fig. 4.14 for an example) and failed fits were discarded. The distribution of the extracted raw yields

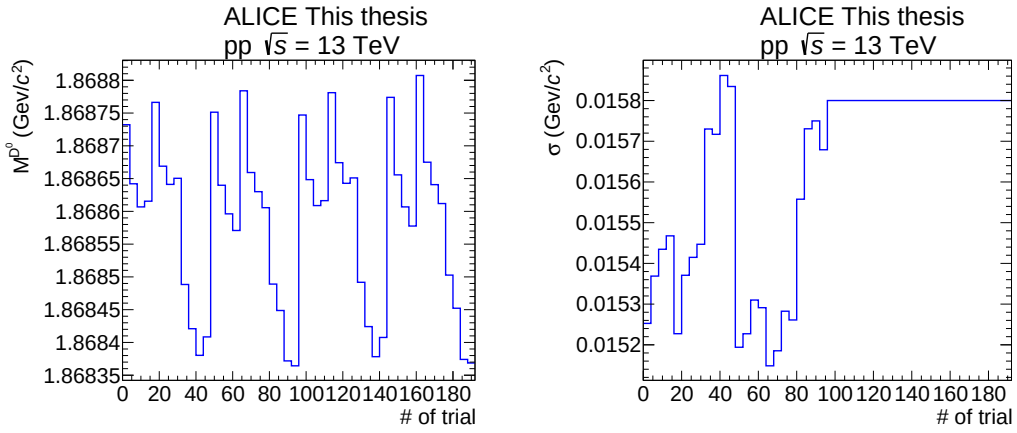


Figure 4.14: Parameters of the invariant mass peak fits of $\mathrm{D}^0$ candidates (central value $M^{\mathrm{D}^0}$ and width $\sigma$) for all combinations of the fit settings variations for $\mathrm{D}^0$ mesons with $12 < p_{\mathrm{T}}^{\mathrm{D}^0} < 18$ (GeV/$c$) and events with $R_{\mathrm{T}} < 1$.

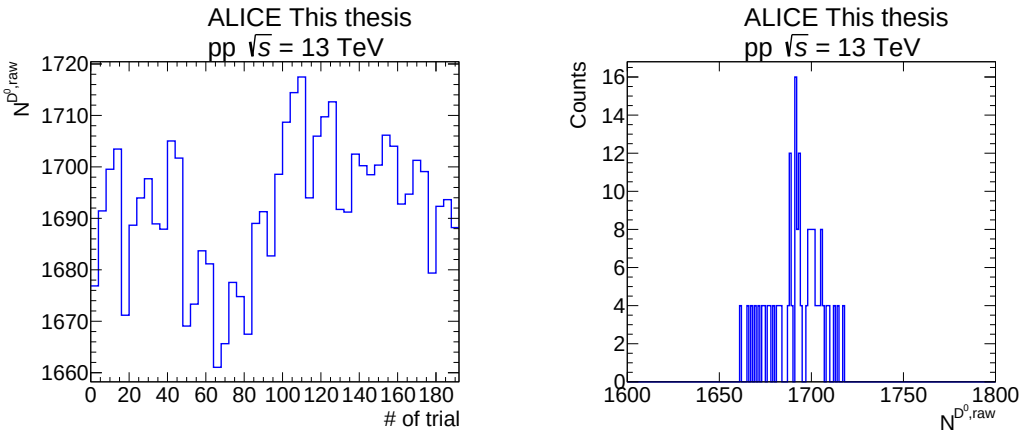


Figure 4.15: Number of extracted raw $\mathrm{D}^0$-meson yields for all combinations of the fit settings variations (left) and their distribution (right) for $\mathrm{D}^0$ mesons with $12 < p_{\mathrm{T}}^{\mathrm{D}^0} < 18$ (GeV/$c$) and events with $R_{\mathrm{T}} < 1$.

in the trials approximates a Gaussian form (Fig. 4.15). The systematic uncer-

tainty assigned to each of the points in the final result was evaluated based on the width of the raw yield distribution. The raw yield extraction technique applied in my analysis was shown to be quite stable, with the systematic uncertainties resulting from the variation of the fit not exceeding a few percent. The summary of the systematic uncertainties, point-by-point, is presented in Table 4.5.

| $p_{\mathrm{T}}^{\mathrm{D}^0}$ [GeV/$c$] | 2–5 | 5–8 | 8–12 | 12–18 | 18–24 |
|---|---|---|---|---|---|
| $R_{\mathrm{T}} < 1$ | 2% | 1% | 1% | 1% | 3% |
| $R_{\mathrm{T}} > 1$ | 5% | 1% | 1% | 3% | 4% |

Table 4.5: Assigned values of the systematic uncertainties connected to the raw yield extraction.

### 4.7.3 Bin migration systematics

Another major source of systematic uncertainty is the classification of events by the $R_{\mathrm{T}}$ value. Since the $R_{\mathrm{T}}$ classifier is determined from the charged-particle multiplicity in the transverse region, it is sensitive to particle detection at the boundary of the two $R_{\mathrm{T}}$ intervals (i.e., close to the average multiplicity of 6.225). In this range, a slight deviation in the charged-hadron multiplicity can move an event from $R_{\mathrm{T}} < 1$ to the $R_{\mathrm{T}} > 1$ category, or vice versa. To estimate the magnitude of this systematic uncertainty, I compared the results of the analysis obtained purely from data reconstruction with the results of the same analysis using MC-generated particles. The particles reconstructed from data had to be modified with the acceptance-times-efficiency correction to obtain results that are comparable to the MC. Note that the feed-down correction is not needed here, since the result is a fraction between spectra in different $R_{\mathrm{T}}$ regions, meaning that the feed-down factor cancels out. The comparison between reconstructed and MC spectrum ratios is shown in Fig. 4.16. Since there is no significant dependence on $p_{\mathrm{T}}$ for $\mathrm{D}^0$ mesons with transverse momentum larger than $p_{\mathrm{T}}^{\mathrm{D}^0} = 5$ GeV/$c$, the systematics for $p_{\mathrm{T}}^{\mathrm{D}^0}$ bins between $p_{\mathrm{T}}^{\mathrm{D}^0} = 5$ GeV/$c$ and $p_{\mathrm{T}}^{\mathrm{D}^0} = 24$ GeV/$c$ were

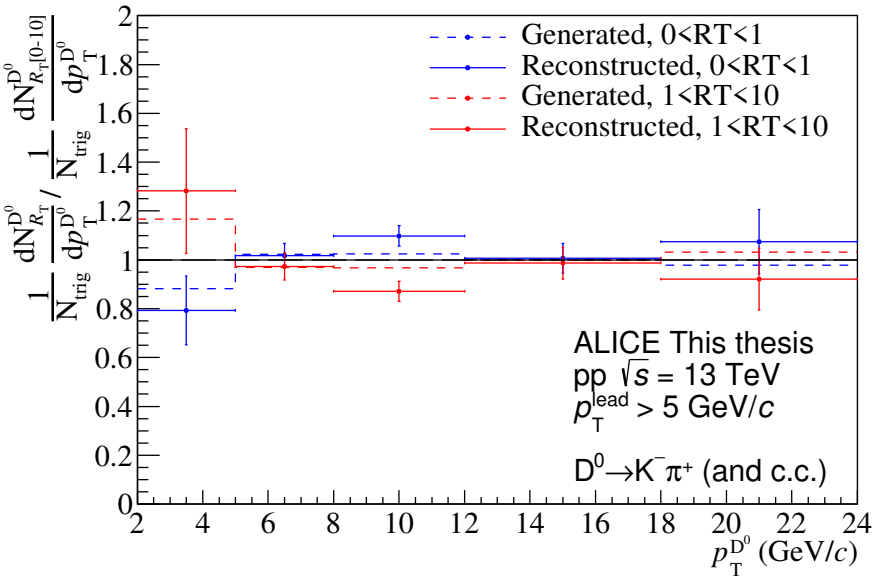


Figure 4.16: Ratio of the $R_{\mathrm{T}}$-dependent per-event $\mathrm{D}^0$-meson yields to the $R_{\mathrm{T}}$-integrated yield for reconstructed and MC data.

averaged. The values of the systematic uncertainties associated with the bin migration that were applied to the final result are summarised in Table 4.6.

| $p_{\mathrm{T}}^{\mathrm{D}^0}$ [GeV/$c$] | 2–5 | 5–8 | 8–12 | 12–18 | 18–24 |
|---|---|---|---|---|---|
| $R_{\mathrm{T}} < 1$ | 11% | 6% | 6% | 6% | 6% |
| $R_{\mathrm{T}} > 1$ | 9% | 5% | 5% | 5% | 5% |

Table 4.6: Assigned values of the systematic uncertainties connected to the bin migration.

### 4.7.4 Feed-down systematic uncertainty

There is another source of uncertainty corresponding to the feed-down correction. This uncertainty mainly arises from the FONLL spectrum. Following standard procedures [98], the FONLL factorisation and renormalisation scales, as well as the heavy-quark masses were varied as described in Ref. [99]. These variations result into two extreme values for the predicted FONLL particle spectra: one

with the highest possible values and another with the lowest. The difference between the feed-down corrections calculated with the standard FONLL spectra and the extreme ones gives the magnitude of this systematic uncertainty. This is the dominant source of systematic uncertainty in the lowest $p_{\mathrm{T}}^{\mathrm{D}^0}$ range, where it reaches up to 27%. The summary of the values assigned to the final result is presented in Table 4.7.

| $p_{\mathrm{T}}^{\mathrm{D}^0}$ [GeV/$c$] | 2–5 | 5–8 | 8–12 | 12–18 | 18–24 |
|---|---|---|---|---|---|
| $R_{\mathrm{T}} < 1$ | 27% | 5% | 3% | 2% | 1% |
| $R_{\mathrm{T}} > 1$ | 20% | 8% | 5% | 3% | 3% |

Table 4.7: Assigned values of the systematic uncertainties connected to the feed-down calculation.

There are a few additional sources of systematic uncertainty that are typically considered in D-meson analyses: the shape of the simulated $p_{\mathrm{T}}$ spectrum, the identification of charged hadrons, and the contribution of $\mathrm{D}^0$ reflections. The first uncertainty is estimated by using FONLL as an alternative event generator to simulate the $p_{\mathrm{T}}$ distribution of D mesons and comparing it to MC-generated results afterwards. The second uncertainty is evaluated by modifying the track selection criteria for identifying hadrons stemming from $\mathrm{D}^0$-meson decays. The contribution of reflections is determined by varying the ratio of the integral of the reflections to the integral of the signal and the shape of the templates used in the invariant-mass fits. All these sources of systematic uncertainty were found to be negligible [98], especially in comparison to the other sources of systematic uncertainties already described above, so I did not consider them in the analysis.

The summary of all systematic uncertainties, as well as the final assigned value for each data point in the result, is presented in Table 4.8. Since the individual sources of systematic uncertainty were considered to be uncorrelated with each other, they were added in quadrature to obtain the total systematic uncertainty for each data point in the final result.

| $R_{\mathrm{T}}$ | $p_{\mathrm{T}}^{\mathrm{D}^0}$ [GeV/$c$] | $\mathrm{D}^0$ selection | Raw yield extraction | Bin migration | Feed-down | Total |
|---|---|---|---|---|---|---|
| 0–1 | 2–5 | 6% | 2% | 11% | 27% | 30% |
| | 5–8 | 3% | 1% | 6% | 5% | 8% |
| | 8–12 | 1% | 1% | 6% | 3% | 7% |
| | 12–18 | 2% | 1% | 6% | 2% | 7% |
| | 18–24 | 2% | 3% | 6% | 1% | 7% |
| 1–10 | 2–5 | 7% | 5% | 9% | 20% | 24% |
| | 5–8 | 4% | 1% | 5% | 8% | 10% |
| | 8–12 | 1% | 1% | 5% | 5% | 7% |
| | 12–18 | 2% | 3% | 5% | 3% | 7% |
| | 18–24 | 2% | 4% | 5% | 3% | 7% |

Table 4.8: Summary of the total systematic uncertainties for each $R_{\mathrm{T}}$ category and $p_{\mathrm{T}}^{\mathrm{D}^0}$ range.

## 4.8 Corrected yields and model comparison

The $R_{\mathrm{T}}$-dependent per-trigger yields of $\mathrm{D}^0$ mesons were obtained by correcting the raw yields with the acceptance, efficiency and feed-down factors and then normalising them by the number of events registered in the corresponding $R_{\mathrm{T}}$ interval. For a better representation of the trends, I show the results as a ratio between the $R_{\mathrm{T}}$-differentiated yields and the $R_{\mathrm{T}}$-integrated yield, similarly to the results in Chapter 3.

In Fig. 4.17, the obtained yields in the toward region are presented, with the error bars representing the statistical uncertainties and boxes representing total systematic uncertainties. For $p_{\mathrm{T}}^{\mathrm{D}^0} > 5$ GeV/$c$, the results are consistent with unity within uncertainties in both $R_{\mathrm{T}}$ intervals. This indicates that the $\mathrm{D}^0$ mesons with high transverse momentum are produced in connection with the leading processes. On the other hand, for the lowest $p_{\mathrm{T}}^{\mathrm{D}^0}$ interval, there is a hint of dependence on the transverse activity. The results are also compared to the PYTHIA 8 simulations with the Monash as well as the CR-BLC Mode 2 tunes. Both calculations describe the data well within uncertainties, with the Monash tune predicting a slightly larger difference between the two $R_{\mathrm{T}}$ regions

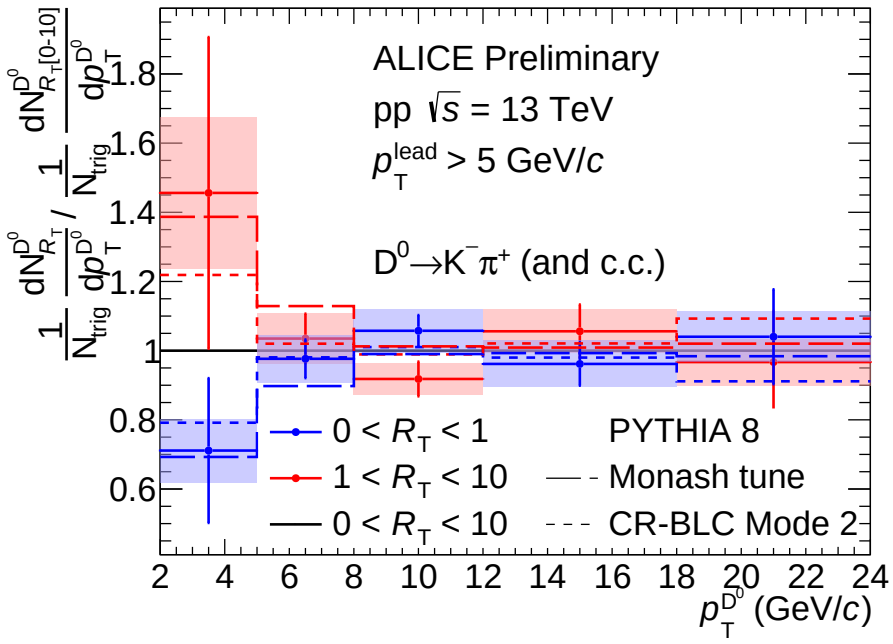


Figure 4.17: Ratio of the $R_{\mathrm{T}}$-dependent per-event $\mathrm{D}^0$-meson yields to the $R_{\mathrm{T}}$-integrated yield in the toward region, as a function of $p_{\mathrm{T}}^{\mathrm{D}^0}$, in pp collisions at $\sqrt{s} = 13$ TeV. The results are compared to model calculations from the PYTHIA 8 Monash and CR-BLC Mode 2 tunes. Boxes represent the total systematic uncertainty of the result.

at $p_{\mathrm{T}}^{\mathrm{D}^0} < 5$ GeV/$c$. However, simulations also show a dependence on $R_{\mathrm{T}}$ in the $5 < p_{\mathrm{T}}^{\mathrm{D}^0} < 8$ interval, while no such hint is observed in the data.

I also simulated the $R_{\mathrm{T}}$-dependent $\mathrm{D}^0$ production in the transverse region with the same two PYTHIA 8 tunes, shown in Fig. 4.18. There is a clear separation between the two $R_{\mathrm{T}}$ intervals across the full $p_{\mathrm{T}}^{\mathrm{D}^0}$ range, signalling that the $\mathrm{D}^0$-meson production is mostly independent of the leading processes. The effect is substantially stronger for the CR-BLC Mode 2 tune compared to the Monash tune due to the difference in the predicted underlying event by the two models. These predictions can be verified with a future high-precision measurement from the LHC Run 3 data-taking period.

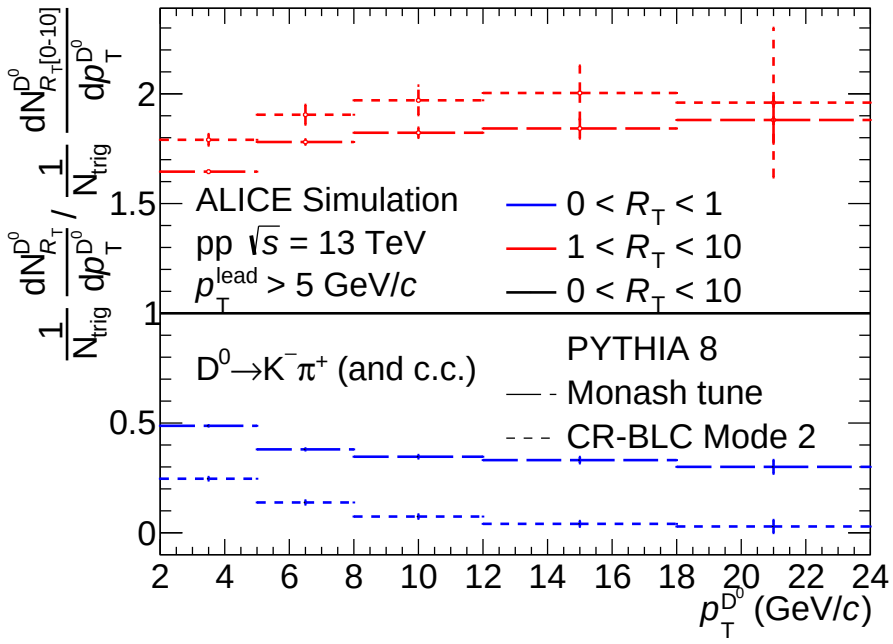


Figure 4.18: Ratio of the $R_{\mathrm{T}}$-dependent per-event $\mathrm{D}^0$ meson yields to the $R_{\mathrm{T}}$-integrated yield in the transverse region, as a function of $p_{\mathrm{T}}^{\mathrm{D}^0}$, in simulations of pp collisions at $\sqrt{s} = 13$ TeV from the PYTHIA 8 Monash and CR-BLC Mode 2 tunes.

## 4.9 Summary

Following my studies of the heavy-flavour production as a function of transverse event activity in simulations, I performed the data analysis of $\mathrm{D}^0$-meson production in the toward region as a function of $R_{\mathrm{T}}$ in pp collisions at $\sqrt{s} = 13$ TeV centre-of-mass energy with the ALICE experiment.

I obtained that in the $2 < p_{\mathrm{T}}^{\mathrm{D}^0} < 5$ GeV/$c$ region, events with above-average underlying event activity hint at a higher rate of $\mathrm{D}^0$-meson production in the toward region than events with below-average underlying event activity, while there is no significant difference from unity for either case if $p_{\mathrm{T}}^{\mathrm{D}^0} > 5$ GeV/$c$. I compared my results to the model predictions. The results are consistent with PYTHIA 8 using both the Monash tune and a model with colour reconnection

beyond leading colour approximation.

The integrated luminosity expected from the ongoing Run 3 data-taking period will make it feasible to carry out $R_{\mathrm{T}}$-differential studies of heavy-flavour production with the ALICE apparatus down to even lower transverse momenta, focusing on the transverse region which is representative of the underlying event.

# Chapter 5

# Timescale of heavy- and light-flavour production via non-extensive thermodynamics

In this chapter, I apply the principles of Tsallis thermodynamics to study the production of heavy quarks for the first time. I investigate the feasibility of such a study by investigating the thermodynamic consistency of the results. Additionally, I compare the results obtained for heavy-flavour hadrons to the light flavour and estimate the production time scales for various light- and heavy-flavour species. The research detailed in this chapter was published in Refs. [100, 101].

## 5.1 Flavour-dependent Tsallis thermometer

The Tsallis thermometer is a conceptual tool used in the context of high-energy physics, particularly in systems exhibiting non-extensive statistical behaviour. It is based on Tsallis statistics, a generalisation of the Boltzmann – Gibbs framework, that can be applied to locally non-thermalised systems.

### 5.1.1 Tsallis fits to spectra from RHIC and the LHC

To study the production of heavy-flavour hadrons using the Tsallis thermometer, I analysed publicly available measurements from the ALICE and STAR experiments [100]. These measurements span diverse collision systems (pp, p–Pb, Au–Au, and Pb–Pb) and energies (from $\sqrt{s_{\rm NN}} = 200$ GeV up to $\sqrt{s} = 7$ TeV). The studied pp collisions include minimum-bias spectra of $\rm D^0$, $\rm D^+$, and $\rm D^{*+}$ mesons at $\sqrt{s} = 5.02$ TeV and 7 TeV energies from the ALICE experiment [96, 98]. The spectra of these three meson species were also analysed from the p–Pb collisions at $\sqrt{s_{\rm NN}} = 5.02$ TeV taken by the ALICE experiment [102]. I also used two centrality-dependent $\rm D^0$-meson datasets: one from the Au–Au system at $\sqrt{s_{\rm NN}} = 200$ GeV from the STAR experiment [103], and another from the Pb–Pb system at $\sqrt{s_{\rm NN}} = 2.76$ TeV centre-of-mass energy from the ALICE experiment [104]. The $\rm D^0$-meson spectra from the STAR experiment were measured across five centrality classes: 0–10%, 10–20%, 20–40%, 40–60%, 60–80%. In contrast, the ALICE data consisted of two centrality classes: 0–20% and 40–80%. The charged-particle multiplicity corresponding to each centrality class is presented in Table 5.1, with higher multiplicity corresponding to more central collisions. All the heavy-flavour spectra that are used in this analysis cover a broad range of transverse momentum, with a large number of measured data points, enabling precise fitting with the Tsallis – Pareto distribution (Eq. (2.8)) [71]. Note that fitting with the Boltzmann – Gibbs distribution fails at transverse momenta above few GeV/$c$ [105].

I fitted the investigated D-meson datasets with the Tsallis – Pareto distribution using the LMFIT: Non-Linear Least-Squares Minimization and Curve-Fitting for Python package [106]. The fitting process was performed in two stages. First, the low- and high-$p_{\rm T}$ regions of spectra were fitted separately. The results from these initial fits were then used as input for fitting the entire spectrum. This method resulted in stable fits and yielded good $\chi^2/ndf$ values. The extracted fit

parameters, including the Tsallis temperature ($T$) and non-extensivity parameter ($q$), are summarised in Table 5.1. Examples of the fitted spectra are shown in Fig. 5.1, while all the fitted spectra can be found in Appendix A of Ref. [100].

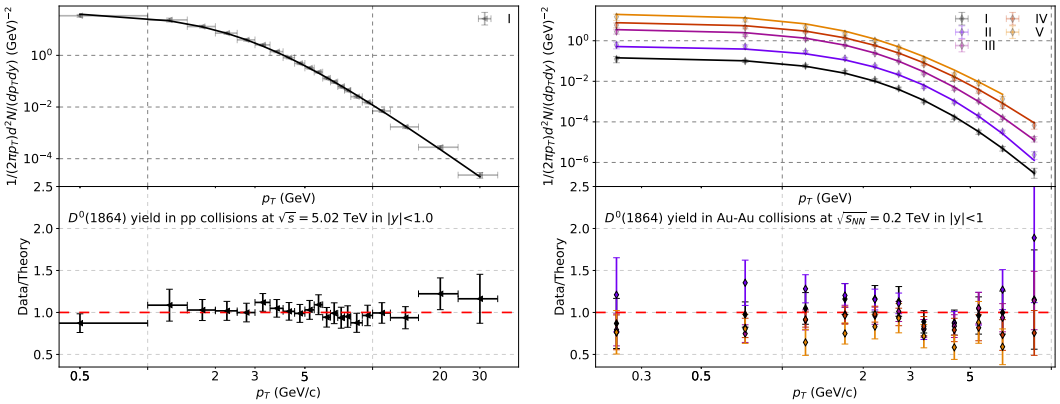


Figure 5.1: Fits on the D-meson spectra. (Left) $D^0$-meson spectrum from the ALICE pp data at $\sqrt{s} = 5.02$ TeV. (Right) $D^0$-meson spectra from the STAR Au–Au data at $\sqrt{s_{NN}} = 200$ GeV in 5 centrality classes.

The presence of radial flow may slightly alter the outcome of the fits. However, the current description, which utilises the non-extensive framework within a co-moving reference frame [107] and uses inputs from broader $p_T$ ranges (from 0 up to 8–30 GeV/$c$ depending on the particle species), does not require a radial flow parameter to account for the final-state hadrons produced in heavy-ion collisions [100].

### 5.1.2 Validation of the thermodynamical consistency

The non-extensive thermodynamic model used in my studies is constructed based on first principles. Consequently, the model, including the derived Tsallis – Pareto distributions, should satisfy the Euler equation [73]:

$$\epsilon + P - Ts - \mu n = 0 \ . \tag{5.1}$$

To verify whether the extracted fit parameters for the heavy-flavour mesons are consistent with thermodynamic principles, I checked the fulfilment of the first-

| $\sqrt{s_{NN}}$ [GeV] | Hadron | $\left\langle \frac{\mathrm{d}N_{\mathrm{ch}}}{\mathrm{d}\eta} \right\rangle$ | $T$ [GeV] | $q$ | $\chi^2$/ndf |
|---|---|---|---|---|---|
| Au–Au, 200 | $\mathrm{D}^0$ | 680.0 | 0.32±0.01 | 1.06±0.01 | 4.1/8 |
| | | 424.5 | 0.36±0.03 | 1.05±0.02 | 15.6/8 |
| | | 235.7 | 0.31±0.01 | 1.07±0.01 | 12.7/8 |
| | | 90.0 | 0.32±0.02 | 1.09±0.01 | 13.8/8 |
| | | 27.0 | 0.29±0.04 | 1.12±0.03 | 29.2/8 |
| Pb–Pb, 2760 | $\mathrm{D}^0$ | 600.0 | 0.32±0.06 | 1.16±0.02 | 0.9/4 |
| | | 45.0 | 0.23±0.05 | 1.21±0.02 | 0.9/4 |
| pp, 5020 | $\mathrm{D}^0$ | | 0.45±0.01 | 1.16±0.01 | 7.8/18 |
| | $\mathrm{D}^+$ | | 0.43±0.02 | 1.16±0.01 | 15.9/17 |
| | $\mathrm{D}^{*+}$ | | 0.44±0.02 | 1.17±0.01 | 11.6/16 |
| p–Pb, 5020 | $\mathrm{D}^0$ | | 0.43±0.02 | 1.17±0.01 | 199.7/18 |
| | $\mathrm{D}^+$ | | 0.38±0.03 | 1.17±0.01 | 792.3/17 |
| | $\mathrm{D}^{*+}$ | | 0.42±0.02 | 1.17±0.01 | 93.2/16 |
| pp, 7000 | $\mathrm{D}^0$ | | 0.49±0.02 | 1.15±0.01 | 7.5/10 |
| | $\mathrm{D}^+$ | | 0.47±0.04 | 1.16±0.01 | 7.8/8 |
| | $\mathrm{D}^{*+}$ | | 0.44±0.04 | 1.17±0.01 | 7.5/8 |

Table 5.1: Parameters of Tsallis fits on D-meson spectra.

order Euler equation. I calculated the quantities in eq. (5.1) from the Tsallis–Pareto distribution (eq. (2.8)) using the fitted Tsallis parameters, as follows [72, 73]:

$$P = g \int \frac{\mathrm{d}^3 p}{(2\pi)^3} T f, \tag{5.2}$$

$$N = nV = gV \int \frac{\mathrm{d}^3 p}{(2\pi)^3} f^q, \tag{5.3}$$

$$s = g \int \frac{\mathrm{d}^3 p}{(2\pi)^3} \left[ \frac{m_{\mathrm{T}} - m}{T} f^q + f \right], \tag{5.4}$$

$$\varepsilon = g \int \frac{\mathrm{d}^3 p}{(2\pi)^3} m_{\mathrm{T}} f \ . \tag{5.5}$$

Here, $f$ is the momentum distribution function of the degrees of freedom (hadrons), defined through the Tsallis–Pareto distribution.

Figure 5.2 demonstrates that the consistency condition is satisfied for light-

flavour mesons within 1% precision. For heavier hadrons, slight deviations can occur; however, for D mesons, these deviations remain below 8%. For most hadrons

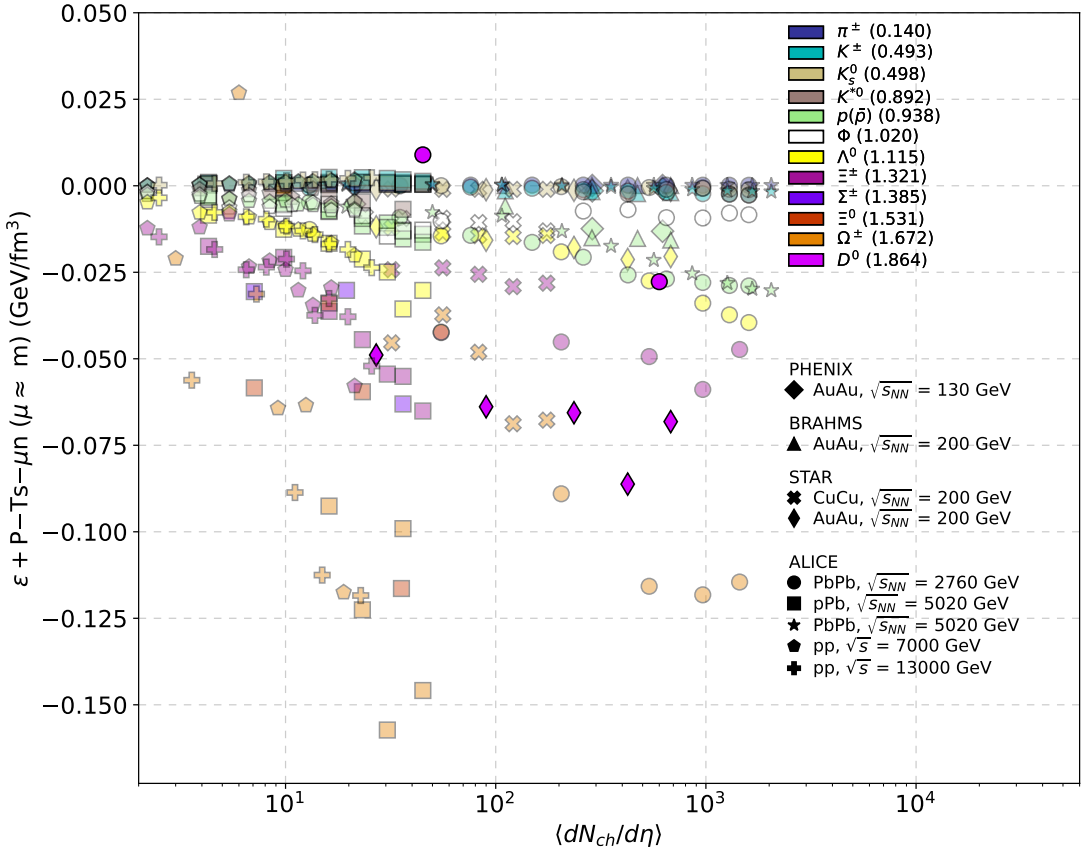


Figure 5.2: Thermodynamical consistency of the Tsallis – Pareto parameters. D-meson results (magenta) are compared to light-flavour hadron results from Ref. [75] (semi-transparent).

measured with high precision, the Tsallis model provides a thermodynamically consistent description. The slight deviations observed in the heavy-flavour case may result from the larger uncertainties in the D-meson spectra or indicate the limitations of the applicability of the non-extensive framework to such system.

### 5.1.3 Application of the Tsallis thermometer

The $T - (q-1)$ diagram containing pairs of fitted parameters for all the studied hadron spectra is called the Tsallis thermometer [75]. It can be used to study the

relations between particle species, collision systems, energies, and multiplicities within the framework of non-extensive thermodynamics. In Fig. 5.3, I present the extracted $T$ and $q$ pairs for the D mesons, alongside the parameters from the light-flavour study [75]. The light-flavour parameters are displayed without error bars and with semi-transparent colours for better visibility.

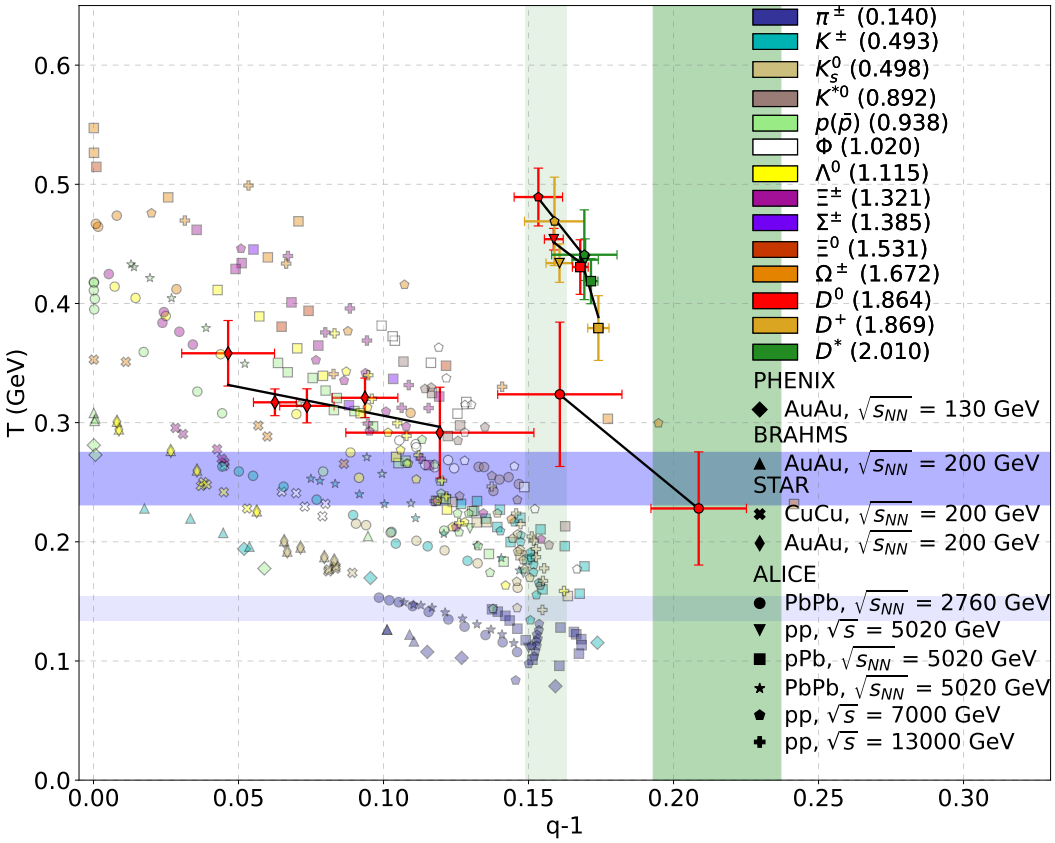


Figure 5.3: Tsallis-thermometer: the fitted $T$ and $q$ parameters of identified $D^0$, $D^+$ and $D^{*+}$ mesons stemming from pp, p–Pb, Pb–Pb, and Au–Au collisions at various energies and various multiplicity classes. Results for light-flavour hadrons from Ref. [75] are shown in semi-transparent colours for comparison. The green and blue bands show the estimated position of the "common" Tsallis parameters (see Sec. 5.1.4 for further details) for D mesons (with solid colours) and light flavours (with half-transparent colours).

For light-flavour hadrons, a mass hierarchy is observed in the $T$—$(q-1)$ diagram: the $T$ parameter shows an increasing trend with particle mass, being

lowest for pions and generally increasing towards heavier hadron species. A strong dependence on multiplicity is also evident – points corresponding to spectra with high multiplicity are located at higher $T$ values and lower $q$ values (towards the top left of the diagram), while low-multiplicity data points are concentrated at lower $T$ and higher $q$ values (towards the bottom right of the Tsallis thermometer). This behaviour becomes even more pronounced for heavy hadrons.

The D mesons, that are subject to the current study, follow these general trends. The D-meson points typically correspond to higher $T$ values compared to light-flavour hadrons from similar collision systems. Similarly to the light-flavour case, there is a multiplicity dependence, with $T$ increasing and $q$ decreasing as multiplicity rises.

However, there are notable differences in the trends between light- and heavy-flavour hadrons, offering insights into their differing production mechanisms and timescales. Light-flavour hadrons of the same species are concentrated within a narrow band of the Tsallis thermometer, showing minimal dependence on the collision system and energy. In contrast, the D-meson points from different collision systems are much more distant from each other. Specifically, the $T$–$q$ parameter pairs for D mesons shift towards the top right of the diagram as collision energy increases. This behaviour may be explained by the fact that in small collision systems, $c$ quarks originate directly from the early stages of the collisions, corresponding to high $T$ (Tsallis temperature) values and larger non-extensivity parameter ($q$). Conversely, in A–A collisions, $c$ quarks may undergo coalescence within the cooling and expanding medium [108], resulting in lower Tsallis parameter values.

### 5.1.4 Common Tsallis parameters

The Tsallis thermometer shows a grouping of all light-flavour hadrons at small multiplicities around a given point (intersection of the half-transparent blue and

green bands in Fig. 5.3) [75]. I call The Tsallis parameters corresponding to this point the "common" Tsallis parameters, $T_{\mathrm{eq}}$ and $q_{\mathrm{eq}}$. The $T_{\mathrm{eq}}$ and $q_{\mathrm{eq}}$ parameters correspond to a dilute system limit, which does not depend significantly on the collision system and energy. For D mesons, the behaviour is similar; however, their grouping point is different than that of the light-flavour case.

To determine the grouping point of D mesons on the Tsallis thermometer, I used the relation between the $T$ and $q$ parameters defined in Eq. (2.11). This function was used to fit the different sets of D-meson points on the $T$—$(q-1)$ diagram. The points from Au–Au and Pb–Pb collisions were fitted separately, while minimum-bias datasets from the same collision system and energy were grouped together due to the similar masses of D-meson species (1.864 GeV/$c^2$ for $\mathrm{D}^0$, 1.869 GeV/$c^2$ for $\mathrm{D}^+$ and 2.010 GeV/$c^2$ for $\mathrm{D}^{*+}$) and the limited data available. The fitted lines are shown in black in Fig. 5.3.

The $E$ and $\delta^2$ parameters extracted from these fits are presented in Fig. 5.4, along with points corresponding to light-flavour hadrons shown in semi-transparent colours. The relative size of multiplicity fluctuations, $\delta^2$, is larger for all D-meson points than that of light-flavour hadrons. Furthermore, the points corresponding to small collision systems exhibit larger $E$ values than those from heavy-ion collisions, as the slope of the fits in the $T$—$(q-1)$ diagram is generally steeper for these systems.

To determine the common Tsallis parameters for D mesons, I inverted Eq. (2.11) into the form:

$$E\delta^2 = T_{\mathrm{eq}} - (q_{\mathrm{eq}} - 1)E \ . \tag{5.6}$$

By fitting the D-meson points in the $E\delta^2$—$E$ diagram using this equation, I obtained $T_{\mathrm{eq}} = 0.253 \pm 0.022$ GeV and $q_{\mathrm{eq}} = 1.215 \pm 0.022$. These values, along with their uncertainties, are shown in Fig. 5.3 as the solid-coloured blue and green bands, respectively. The position of the bands is determined by the central values of the fitted $T_{\mathrm{eq}}$ and $q_{\mathrm{eq}}$ parameters, while the width of the bands is defined by

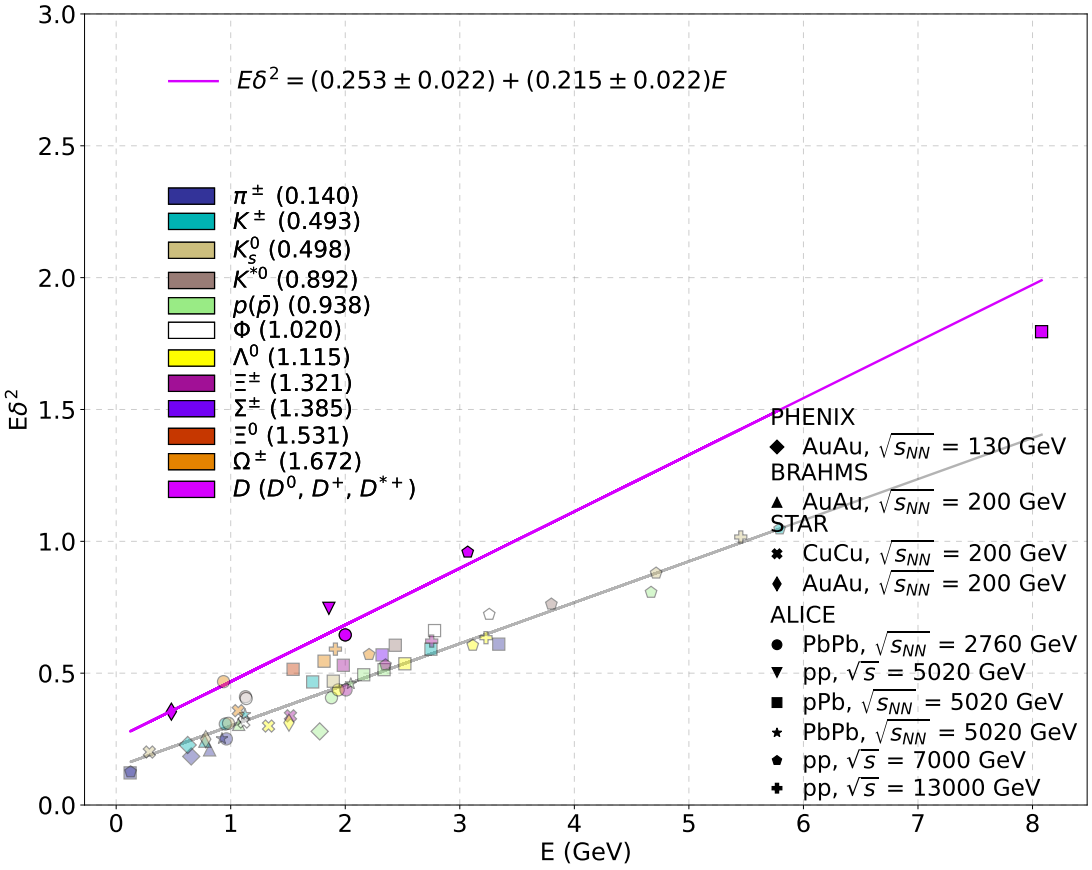


Figure 5.4: Correlation of the fit parameters $E\delta^2$ as a function of $E$. D-meson results (magenta) are compared to light-flavour hadron results (semi-transparent) from Ref. [75]. The magenta line shows the fitting of the D-meson points with Eq. (5.6).

the fit uncertainty.

The common Tsallis parameters for D mesons are offset by $\Delta T_{\mathrm{eq}} = 0.109 \pm 0.024$ GeV and $\Delta q_{\mathrm{eq}} = 0.059 \pm 0.023$ towards higher values compared to light hadrons. This difference can be attributed to the different information carried by light and heavy-flavour hadrons. Light-flavour hadron spectra predominantly form during the kinetic freeze-out phase of a collision, while the higher values of $T_{\mathrm{eq}}$ and $q_{\mathrm{eq}}$ demonstrate that heavy-flavour spectra reflect a hotter, more non-extensive state of the reaction. Moreover, the smaller the system size, the higher the non-extensivity parameter $q$.

### 5.1.5 Flavour-dependent time evolution

I used the Bjorken model [109] to connect the proper time of charm spectrum creation, $\tau_{\rm D}$, to that of light-flavour hadrons, $\tau_{\rm LF}$. In this model, the system is assumed to undergo a boost-invariant expansion along the beam axis, where the proper-time evolution of energy density and temperature follows a scaling law. It is important to note that the Bjorken picture imposes no specific thermodynamic assumptions, thus it is applicable for the non-extensive thermodynamic model to define a temperature-like measure. The Bjorken model defines the energy density as $\varepsilon = \sigma T^4$ (note that, while the equation takes the form of the Stefan–Boltzmann law, it follows directly from the Bjorken model). With the initial condition $\varepsilon(\tau_0) = \varepsilon_0 \rightarrow T(\tau_0) = T_0$, an analytical solution can be obtained [110]:

$$\tau = \tau_0 \left(\frac{T_0}{T}\right)^3 . \tag{5.7}$$

Assuming identical initial conditions for light- and heavy-flavour hadrons, i.e., $T_{0,LF}(\tau_0) = T_{0,D}(\tau_0)$, the relation between the proper times for charm and light-flavour creation becomes

$$\tau_{\rm D} = \tau_{\rm LF} \left(\frac{T_{\rm LF}}{T_{\rm D}}\right)^3 . \tag{5.8}$$

As mentioned earlier, the Bjorken model is independent of thermodynamic assumptions, allowing for the use of the common Tsallis temperature, $T_{\rm eq}$, obtained separately for light-flavour hadrons and D mesons in the non-extensive thermodynamic model. Using this, I determined the ratio of proper times as:

$$\tau_{\rm D} = (0.18 \pm 0.06)\tau_{\rm LF} . \tag{5.9}$$

This result indicates that heavy-flavour hadrons carry thermodynamic information from significantly earlier stages of the reaction than light-flavour hadrons, as shown in Fig. 5.5.

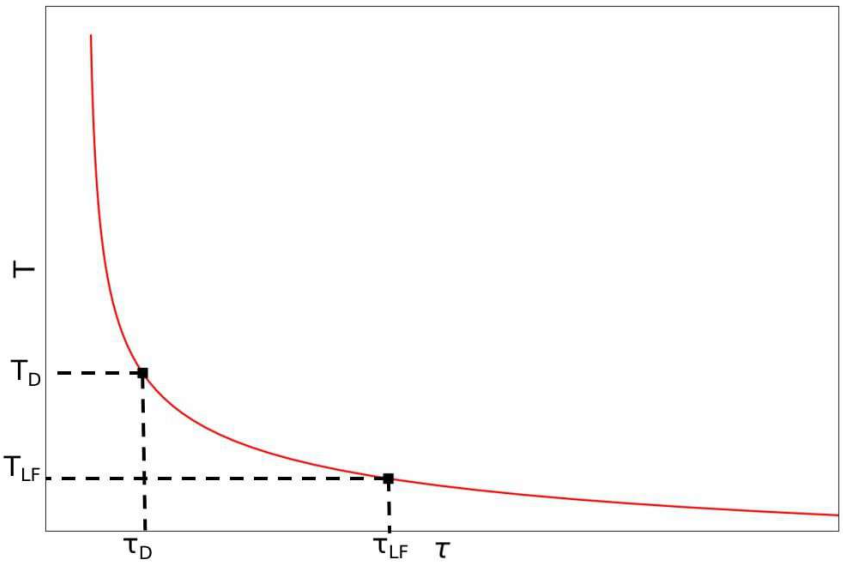


Figure 5.5: Schematic cooling curve of an ultrarelativistic collision of hadrons. Temperature and time scales are shown in arbitrary units.

## 5.2 Species-dependent analysis of the LHC data

Thanks to new, high-precision data available from the ALICE experiment, in this section I expand my previous results by considering various hadron species separately [101]. I analysed the production yields of charged pions [111–115] ($\pi^+$), kaons [22, 111–119] ($K^+$, $K^{0*}$, $K^0_s$), protons [111–115] (p), $\phi^0$ mesons [113, 117, 118], $\Lambda^0$ baryons [22, 112, 116, 119] and D mesons [96, 98, 102, 104] ($D^0$, $D^{*+}$, $D^+$), as well as the corresponding charge conjugates.

I followed the procedure described in the previous section to determine the $T_{\rm eq}$ and $q_{\rm eq}$ values separately for the various hadron species. Note that while the earlier studies used data from both RHIC and the LHC, here I focus exclusively on LHC results to ensure that the fundamental thermodynamic properties, such as heat capacity, remain stable within the energy regime under investigation [120].

### 5.2.1 Mass hierarchy

The obtained $T_{\rm eq}$ and $q_{\rm eq}$ values for light-flavour hadrons, as well as for heavy-flavour D mesons, are summarised in Table 5.2. These values are also visualised in Fig. 5.6, which shows the $T_{\rm eq}$ and $q_{\rm eq}$ parameters as functions of the hadron masses. The common Tallis temperature $T_{\rm eq}$ increases with the mass of the

| Hadron | Quark content | Mass, $m$ [MeV] | $T_{\rm eq}$ [MeV] | $q_{\rm eq}$ |
|---|---|---|---|---|
| $\pi^+$ | $u\overline{d}$ | 140 | $107 \pm 4$ | $1.151 \pm 0.004$ |
| $\mathrm{K}^+$ | $u\overline{s}$ | 493 | $154 \pm 11$ | $1.163 \pm 0.009$ |
| $\mathrm{K}^0_{\mathrm{s}}$ | $\frac{d\overline{s}+\overline{d}s}{\sqrt{2}}$ | 498 | $161 \pm 12$ | $1.159 \pm 0.007$ |
| $\mathrm{K}^{0*}$ | $d\overline{s}$ | 892 | $255 \pm 15$ | $1.138 \pm 0.008$ |
| p | $uud$ | 938 | $172 \pm 18$ | $1.143 \pm 0.009$ |
| $\phi^0$ | $s\overline{s}$ | 1020 | $234 \pm 8$ | $1.152 \pm 0.004$ |
| $\Lambda^0$ | $uds$ | 1115 | $158 \pm 23$ | $1.146 \pm 0.009$ |
| $\mathrm{D}^0$, $\mathrm{D}^+$, $\mathrm{D}^{*+}$ | $c\overline{u}$, $c\overline{d}$ | 1861–2010 | $343 \pm 107$ | $1.183 \pm 0.044$ |

Table 5.2: Summary of $T_{\rm eq}$ and $q_{\rm eq}$ values for different particle species. (Charge conjugates are not marked explicitly.)

mesons, and the trend determined by mesons is well described by a linear fit

$$T_{\rm eq} = (0.15 \pm 0.01) \times m + (85 \pm 5)\ \text{MeV} \tag{5.10}$$

in $c \equiv 1$ units. The baryons, however, do not follow the mass-ordered trend observed for mesons, as their $T_{\rm eq}$ values are significantly smaller compared to mesons with similar masses, hinting at later formation times for baryons than for mesons. This mass dependence is consistent with earlier observations of mass hierarchy from the Tsallis temperatures obtained directly from spectrum fits, as described in the previous section. While the emerging picture does not support the common logarithmic mass dependence of mesonic and baryonic Tsallis temperatures [121], more detailed baryonic measurements are needed to draw firm conclusions.

Another observation is that all the light-flavour mesons have similar non-

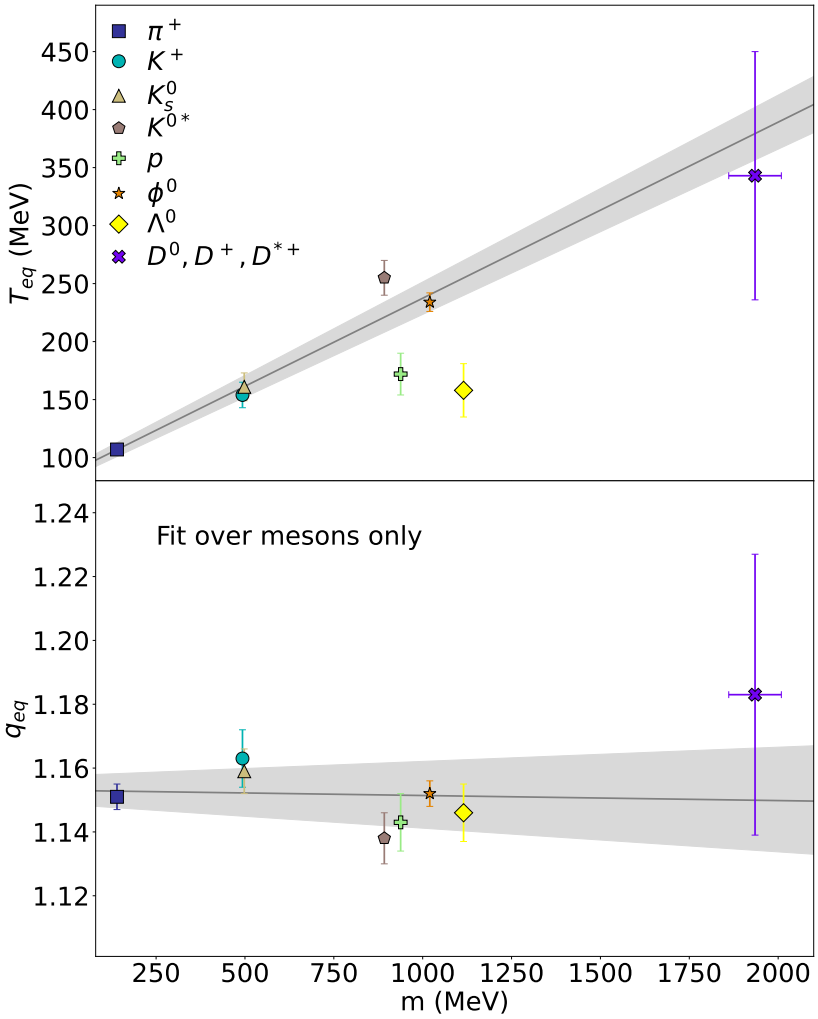


Figure 5.6: $T_{\rm eq}$ and $q_{\rm eq}$ parameters of different hadron species as a function of the invariant mass of the hadrons. The solid lines represent fits over the points corresponding to the mesons, with the grey bands representing the uncertainty range corresponding to one standard deviation.

extensivity parameters $q_{\rm eq}$, varying between 1.15 and 1.16, while the baryons have a slightly lower value, around 1.14. Although a significant difference can be observed between the $q_{\rm eq}$ values of unified RHIC and LHC light-flavour and D meson data, the current precision of LHC-only D-meson data does not support any rising trend. A linear fit to mesons yields

$$q_{\rm eq} = (-1.6 \pm 6.1) \cdot 10^{-6}\,{\rm MeV}^{-1} \times m + 1.153 \pm 0.004\ , \qquad (5.11)$$

which is consistent with a constant.

### 5.2.2 Spectrum formation times

I utilised the Bjorken-type expansion to estimate the formation times of spectra for various hadron species. The formation proper times of each hadron species were estimated with respect to the proper time of pions. The results are presented in Fig. 5.7. It can be observed that meson formation times are ordered by mass,

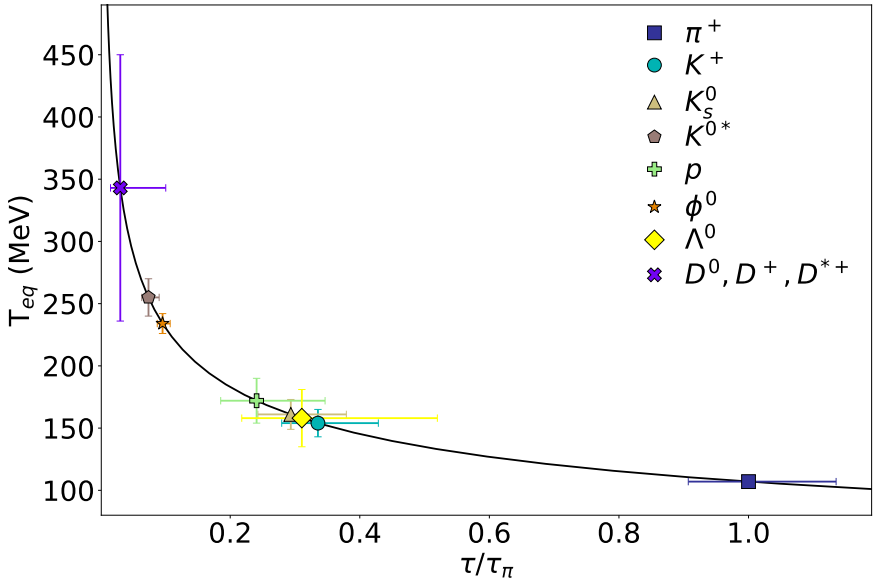


Figure 5.7: Formation proper times for each hadron species within the Bjorken model. The proper time is expressed in units relative to that of the pion, $\tau_\pi$.

with the spectra of heavier mesons corresponding to earlier formation times, while the spectra of lighter mesons are formed later. Interestingly, heavy-flavour D mesons follow this trend as well, albeit with large uncertainties. Baryons are formed later than mesons of similar masses. According to these results, pion spectra are formed at a substantially later time compared to all other hadrons. The proper time associated with the formation of pions is approximately 3 times larger than that for charged kaons, while D meson spectra are formed an order of magnitude earlier than those of kaons ($\tau_{\mathrm{K}}/\tau_\pi \approx 0.34$, $\tau_{\mathrm{D}}/\tau_\pi \approx 0.03$). These

results also agree with my earlier estimation of the relative formation proper times for heavy-flavour and light-flavour hadron spectra (not differentiated by species), $\tau_{\rm HF}/\tau_{\rm LF} \approx 0.18$.

### 5.2.3 Non-extensivity parameter and heat capacity

For systems with a fluctuating number of particles, the non-extensivity parameter $q$ can generally be written as [122]

$$q = 1 - \frac{1}{C} + \delta^2 \ , \tag{5.12}$$

where $C$ is the heat capacity of the system, while $\delta^2$ expresses the temperature or multiplicity fluctuations in the events ($\Delta T^2/\langle T\rangle^2$ and $\Delta n^2/\langle n\rangle^2$, respectively). The values of $\delta^2$ are obtained from fits on the $q$—$T$ points of each hadron species during the evaluation of the $q_{\rm eq}$ and $T_{\rm eq}$ parameters, as described in Sec. 5.1.4. Since the $\delta^2$ values increase with the size of the collision system, I was able to determine a range of possible values for each hadron species, where the lower boundary corresponds to pp collisions and the higher boundary to Pb–Pb collisions.

Several attempts have been made to estimate the heat capacity of the hot hadronic system. Based on temperature fluctuations, the specific heat capacity $c_V = C/n$ corresponding to a constant volume was estimated at SPS energies to be $c_V = 60 \pm 100$, assuming $\langle T\rangle = 180$ MeV [123]. In this study, the Tsallis nature of the $p_{\rm T}$ distribution was considered in the temperature fluctuations, but not in the derivation of the heat capacity. Another work based on lattice QCD calculations estimates $c_V/T^3 \approx 15$ in case of QGP and $c_V/T^3 \approx 21$ for the ideal gas limit [124]. More recent estimates of the specific heat in Au–Au and Cu–Cu collisions at RHIC, based on the Boltzmann – Gibbs statistics, yielded $c_V \approx 1 - 2$ [120]. Note that the $\sqrt{s}$ dependence of the heat capacity in the Hadron Resonance Gas (HRG) model is saturated in the ultra-relativistic limit [120], so this estimate is also

valid at LHC energies. This latter approach relies on extensive thermodynamics where $q = 1$, and therefore Eq. (5.12) reduces to $C = 1/\delta^2$. Non-extensive thermodynamics can provide corrections to this estimate. The Tsallis – Pareto fits to the spectra yield $q$ values significantly above unity, meaning that the specific heat of the system is expected to be higher than in the case of Boltzmann – Gibbs distribution. Another study based on the non-extensive framework obtained the value of specific heat to be around $c_V \approx 1 - 4$, depending on the value of $q$ and $T$ [125].

In my work, I use a different approach. I estimate the specific heat based on the common non-extensivity parameter $q_{\mathrm{eq}}$, corresponding to the low-multiplicity limit. By substituting the $q_{\mathrm{eq}}$ and $\delta^2$ values for each particle species in Eq. (5.12), I can obtain the specific heat of the very-low-multiplicity systems corresponding to the $T_{\mathrm{eq}}$ and $q_{\mathrm{eq}}$ values. The results across the different particle species are consistent with each other, yielding a lower boundary for the specific heat, $C \gtrapprox 5$, independently of the collision system or collision energy. Considering the system sizes, this is consistent with the values of the previous non-extensive study [125]. Due to the hyperbolic dependence between $q_{\mathrm{eq}}$ and $C$, the upper limit of the specific heat cannot be well estimated by the current precision of the available data.

For light mesons (specifically pions and kaons) produced in larger collision systems, $\delta^2 \approx q - 1$, leading to large $C$ values. This implies a largely thermalised system. For heavier mesons, including the heavy-flavour D mesons, which correspond to earlier spectrum formation times, the relative fluctuations are larger, leading to smaller heat capacity compared to the case of light flavours. This implies a strongly non-extensive system.

## 5.3 Summary

In this chapter, I investigated the production of light- and heavy-flavour hadrons within the Tsallis – Pareto non-extensive statistical framework. I used the data measured by the ALICE and STAR experiments that span diverse collision systems and energies.

I showed that the transverse momentum distributions of heavy-flavour D mesons are well described by the Tsallis – Pareto distribution. The parameters from the fits fulfil thermodynamical consistency, therefore the statistical framework is applicable to heavy as well as light flavour.

The Tsallis parameters of the fits to D-meson data exhibit a scaling behaviour with charged-particle multiplicity and with the collision energy, similarly to the light-flavour case. However, the scaling of D mesons is quantitatively different from that of light-flavour and strange hadrons. I found that the $T_{\rm eq}$ and $q_{\rm eq}$ parameters are higher for heavy-flavour than light-flavour hadrons. The higher $q_{\rm eq}$ means that the correlation within the heavy-quark system is slightly larger than that of light and strange quarks, indicating that heavy quarks are produced in the early stages of the collisions. The $T_{\rm eq}$ parameter for D mesons is higher than that of light flavour. This also suggests that D meson spectra preserve information from earlier stages of the reaction than light flavour.

Considering an expanding system and the results from a non-extensive statistical approach, $\Delta T$ and $\Delta q$ on the Tsallis thermometer can be understood as time-frame projections of different stages of the time evolution. By comparing charm production to that of light flavour, I showed that the production of D mesons corresponds to a significantly earlier proper time than light-flavour hadrons. Based on the Bjorken expansion, I estimated it as $\tau_{\rm D} = (0.18 \pm 0.06)\tau_{\rm LF}$.

I further analysed high-precision data from the ALICE experiment to investigate the formation and evolution of hot systems comprising charmed and light hadrons, by individually evaluating various hadron species. I determined

the common Tsallis parameters $T_{\rm eq}$ and $q_{\rm eq}$ for charged pions and kaons, $\rm K^0_s$, (anti)protons, $\phi$ mesons, $\Lambda^0$ hyperons, and D mesons and found that $T_{\rm eq}$ for all the mesons, both light and charm, follow a mass ordering, where $T_{\rm eq}$ linearly increases with mass. Baryons have a slightly lower $T_{\rm eq}$ than mesons with the same mass. On the other hand, LHC data alone does not show a significant ordering of $q_{\rm eq}$ with the mass of different mesons.

Using Bjorken expansion as an assumption, again, I determined the spectrum formation proper times for each hadron species relative to each other. As expected, the proper times are mass ordered and pion spectra are formed at a substantially later time compared to all the other hadrons ($\tau_{\rm K}/\tau_\pi \approx 0.34$ for charged kaons, $\tau_{\rm D}/\tau_\pi \approx 0.03$ for D mesons).

Finally, I estimated the heat capacity of the system based on the common non-extensivity parameters $q_{\rm eq}$ and relative fluctuations $\delta^2$ corresponding to each hadron species. The results yield a system-wide lower boundary, $C \gtrapprox 5$. The upper limit corresponding to light mesons implies a largely thermalised system, while heavier hadrons are strongly non-extensive regardless of the system size. This is consistent with the earlier formation of heavier hadron spectra.

# Chapter 6

# Conclusion and outlook

In my thesis, I used heavy-flavour production from small to large collision systems, both in theory and in experiment, to understand the thermodynamical properties and the QGP-like collective effects in reactions.

The origin of collective effects in small collision systems remains an open question in high-energy physics. One of the main explanations behind the collective behaviour of particles in small systems is vacuum QCD effects at the soft–hard boundary, among them the MPI. While the MPI cannot be accessed directly, there are observables which allow us to implicitly measure the extent of MPI in events.

I investigated the connection between the hard and soft regime using heavy-flavour production in terms of the transverse activity classifier $R_{\mathrm{T}}$, from both theoretical and experimental aspects. I analysed the production of D and B mesons, as well as $c$ and $b$ quarks in pp collisions at $\sqrt{s} = 13$ TeV using PYTHIA 8 simulations. Following the CDF event classification, I studied the production of heavy-flavour hadrons in events triggered by a charged-hadron leading particle. I investigated the production of heavy flavour in the toward region (azimuthally close to the leading particle) and in the transverse region (a region perpendicular to the leading particle). I obtained that the production of D and B mesons in the

toward region depends on the transverse event activity at low transverse momentum $p_{\mathrm{T}}$ values, while this dependence vanishes at high transverse momenta. This allowed me to conclude that low-transverse-momentum D and B mesons are produced in connection with the underlying event, while the high-$p_{\mathrm{T}}$ heavy-flavour mesons are mostly formed in the hard scattering.

As expected, there is a change in the transverse momentum scale connected to the hadronisation of $c$ quarks into D mesons, while a similar momentum loss is not present for the pair of $b$ quarks and B mesons due to much harder fragmentation.

In the transverse region, I observed that the heavy-flavour hadron production is $R_{\mathrm{T}}$-dependent over the full transverse-momentum range that was examined. This indicates that the production of D and B mesons in this region is strongly influenced by the underlying event.

As heavy-flavour hadrons have different fragmentation properties compared to light flavour, using trigger hadrons does not allow for a bias-free comparison between heavy and light-flavour production, especially in the toward and away regions. Therefore, I suggested utilising reconstructed jets as triggers to represent the leading process in events. This allows for retaining the connection between the leading process and the heavy-flavour particle created in association with it. By defining the leading process through reconstructed charged-particle jets, the results with different probes can be directly compared. Constraining the flavour of the jet-initiating parton allows for further insights into the connection of heavy-flavour production to the leading process or the underlying event. Selecting light jets, for instance, ensures that the heavy flavour arrives from a separate process. Heavy-flavour jet triggers, on the other hand, allow for the access of gluon-splitting or flavour-excitation topologies.

The production of D and B mesons in the toward region in events triggered with charm- and beauty-jets, respectively, shows a similar behaviour at low-$p_{\mathrm{T}}$ to that observed in the charged-hadron-triggered events. However, at higher $p_{\mathrm{T}}$ values a dependence on $R_{\mathrm{T}}$ is preserved due to the autocorrelation effects that

can be attributed to the wide-angle gluon splitting. In the case of events triggered by light jets, I observed a strong dependence of produced D and B mesons on the transverse activity $R_{\mathrm{T}}$ over the whole studied $p_{\mathrm{T}}$ range. This observation is consistent with the assumption that heavy flavour in these cases comes from the underlying event.

I also showed that the behaviour of heavy-flavour production in the transverse region in events triggered with jets is qualitatively similar to that observed in charged-hadron-triggered events, as this region is not influenced by the hard processes and is dominated by the underlying event, independently from the selection of leading process.

I continued the study of heavy-flavour production as a function of the transverse activity $R_{\mathrm{T}}$ in data analysis of pp collisions at $\sqrt{s} = 13$ TeV centre-of-mass energy registered with the ALICE experiment. Due to the limitations of available data recorded during the Run 2 data-taking period, I performed the study of $\mathrm{D}^0$-meson production only in the toward region.

The results obtained in the analysis hint at an $R_{\mathrm{T}}$-dependence of the produced $\mathrm{D}^0$ mesons in the lowest transverse-momentum region. This dependence vanishes at higher $p_{\mathrm{T}}$ values. These results confirm my prediction from PYTHIA 8 simulations, and the results are also consistent with simulations using colour reconnection beyond leading colour approximation. A more precise measurement in LHC Run 3 that can also be extended to the transverse region, will have the power to discriminate between different model predictions.

I extended the non-extensive thermodynamic framework to incorporate heavy-flavour production and better understand the timeline of heavy and light-flavour spectrum formation. I used the transverse momentum distributions of the identified D meson species measured in the ALICE and STAR experiments in multiple collision systems from pp to A–A and at collision energies varying from

$\sqrt{s_{\rm NN}}$ = 200 GeV to $\sqrt{s_{\rm NN}}$ = 7 TeV. I showed that the Tsallis–Pareto distribution accurately describes the transverse momentum spectrum of D mesons, similarly to light-flavour hadrons. I confirmed the validity of the applied model by verifying that the thermodynamical consistency is fulfilled.

I also showed that the Tsallis parameters extracted from the transverse momentum spectra of D mesons exhibit a scaling behaviour with the charged-particle multiplicity and collision energies, however, this scaling is quantitatively different from the light-flavour and strange-hadron case. I found that the $T_{\rm eq}$ and $q_{\rm eq}$ parameters are higher for heavy-flavour than light-flavour hadrons. The shift of these parameters supports the fact that heavy flavour is produced at earlier stages of the reaction than light-flavour hadrons, which are formed at the freeze-out stage.

I utilised the Bjorken model to connect the temperature difference between heavy and light flavours to their production timescale. I concluded that the production of D mesons corresponds to a significantly earlier proper time than light-flavour hadrons, $\tau_{\rm D} = (0.18 \pm 0.06)\tau_{\rm LF}$.

I further analysed high-precision data from the ALICE experiment to investigate the production of charmed and light hadrons, by individually evaluating various hadron species. I determined the common Tsallis parameters $T_{\rm eq}$ and $q_{\rm eq}$ for charged pions and kaons, $\rm K^0_s$, (anti)protons, $\phi$ mesons, $\Lambda^0$ hyperons, and D mesons. I obtained that the Tsallis temperature of the common grouping points $T_{\rm eq}$ of mesons scales with the meson mass. On the other hand, the $T_{\rm eq}$ values for baryons are significantly smaller than those of mesons with similar masses. I observed that the non-extensivity parameter of the common grouping points $q_{\rm eq}$ does not depend significantly on the hadron mass.

I observed that, assuming the Bjorken expansion, the meson formation times are ordered by meson mass. Pion spectra are formed substantially later than that of other hadrons: the formation timescale corresponding to pions is 3 times as large as that of kaons, and it is about 30 times larger than that of D mesons.

I also estimated the specific heat of the system based on the values of $q_{\mathrm{eq}}$ and the relative multiplicity fluctuations $\delta^2$. The results across the different particle species are consistent with each other, yielding a lower boundary for the specific heat $C > 5$. The large C values corresponding to light-flavour hadrons imply a largely thermalised system.

During Long Shutdown 2 after the LHC Run 2 data-taking period, the LHC experiments improved their detectors, allowing for much higher readout rates and better detection precision. The ALICE experiment in particular improved its secondary vertex resolution with the upgraded ITS, while the readout rate from the TPC detector was increased with the introduction of Gas Electron Multiplier (GEM) detectors. The first measurements with the Run 3 data show unprecedented precision in the measured spectra [126]. With the Run 3 data, the multi-differential studies of heavy flavour will become possible, together with direct access to the B-hadron sector. The increased amount of data will allow for more precise measurements with the methods I introduced in this thesis work.

# Acknowledgement

First of all, I would like to acknowledge my supervisor, Róbert Vértesi, for his invaluable help throughout my studies. I appreciate his advices and our discussions which allowed me to swiftly progress in my research.

I want to also thank my colleagues and co-authors, Gergely Gábor Barnaföldi and Gábor Bíró. Their experience in the field of non-extensive statistics was very helpful for discovering the particle physics from a new perspective.

I am grateful to all the members of the ALICE heavy-flavour physics working group for their support with the data analysis and countless suggestions for its improvement.

My immense gratitude goes to my family and friends for their moral support during my studies.

And I would like to acknowledge ALICE experiment, HUN-REN Wigner Research Centre for Physics, WSCLab facility. Also support by the NKFIH grant OTKA FK131979, as well as by the 2021-4.1.2-NEMZ_KI-2024-00034 project.

# Bibliography


[1] G. Dissertori. The Determination of the Strong Coupling Constant. *Adv. Ser. Direct. High Energy Phys.*, 26:113–128, 2016. doi: 10.1142/9789814733519_0006.

[2] Edward V. Shuryak. Quantum Chromodynamics and the Theory of Superdense Matter. *Phys. Rept.*, 61:71–158, 1980. doi: 10.1016/0370-1573(80)90105-2.

[3] Ulrich W. Heinz and Maurice Jacob. Evidence for a new state of matter: An Assessment of the results from the CERN lead beam program. 1 2000. arXiv: nucl-th/0002042.

[4] K. Adcox et al. Suppression of hadrons with large transverse momentum in central Au+Au collisions at $\sqrt{s_{NN}}$ = 130-GeV. *Phys. Rev. Lett.*, 88: 022301, 2002. doi: 10.1103/PhysRevLett.88.022301.

[5] Peter Jacobs and Jennifer Klay. Jets and high p(T) hadrons in dense matter: Recent results from STAR. *AIP Conf. Proc.*, 698(1):667–672, 2004. doi: 10.1063/1.1664324.

[6] J. Adams et al. Evidence from d + Au measurements for final state suppression of high p(T) hadrons in Au+Au collisions at RHIC. *Phys. Rev. Lett.*, 91:072304, 2003. doi: 10.1103/PhysRevLett.91.072304.

[7] Urs Achim Wiedemann. Jet Quenching in Heavy Ion Collisions. pages 521–562, 2010. doi: 10.1007/978-3-642-01539-7_17.

[8] Georges Aad et al. Observation of a Centrality-Dependent Dijet Asymmetry in Lead-Lead Collisions at $\sqrt{s_{NN}} = 2.77$ TeV with the ATLAS Detector at the LHC. *Phys. Rev. Lett.*, 105:252303, 2010. doi: 10.1103/PhysRevLett.105.252303.

[9] N. J. Abdulameer et al. Nonprompt direct-photon production in Au+Au collisions at sNN=200 GeV. *Phys. Rev. C*, 109(4):044912, 2024. doi: 10.1103/PhysRevC.109.044912.

[10] Albert M Sirunyan et al. Measurement of nuclear modification factors of $\Upsilon$(1S), $\Upsilon$(2S), and $\Upsilon$(3S) mesons in PbPb collisions at $\sqrt{s_{\mathrm{NN}}} = 5.02$ TeV. *Phys. Lett. B*, 790:270–293, 2019. doi: 10.1016/j.physletb.2019.01.006.

[11] John C. Collins and M. J. Perry. Superdense Matter: Neutrons Or Asymptotically Free Quarks? *Phys. Rev. Lett.*, 34:1353, 1975. doi: 10.1103/PhysRevLett.34.1353.

[12] K. Adcox et al. Formation of dense partonic matter in relativistic nucleus-nucleus collisions at RHIC: Experimental evaluation by the PHENIX collaboration. *Nucl. Phys. A*, 757:184–283, 2005. doi: 10.1016/j.nuclphysa.2005.03.086.

[13] K Aamodt et al. Elliptic flow of charged particles in Pb-Pb collisions at 2.76 TeV. *Phys. Rev. Lett.*, 105:252302, 2010. doi: 10.1103/PhysRevLett.105.252302.

[14] Ke Li, Cheng Ma, Jiahua Qu, and Jiayi Zhang. The perfect fluid characteristic of the quark gluon plasma. In Saman K. Halgamuge, Hao Zhang, Dingxuan Zhao, and Yongming Bian, editors, *The 8th International Conference on Advances in Construction Machinery and Vehicle Engineering*,

pages 1223–1233, Singapore, 2024. Springer Nature Singapore. ISBN 978-981-97-1876-4.

[15] S. Voloshin and Y. Zhang. Flow study in relativistic nuclear collisions by Fourier expansion of Azimuthal particle distributions. *Z. Phys. C*, 70:665–672, 1996. doi: 10.1007/s002880050141.

[16] K. H. Ackermann et al. Elliptic flow in Au + Au collisions at (S(NN))**(1/2) = 130 GeV. *Phys. Rev. Lett.*, 86:402–407, 2001. doi: 10.1103/PhysRevLett.86.402.

[17] Berndt Muller. From Quark-Gluon Plasma to the Perfect Liquid. *Acta Phys. Polon. B*, 38:3705–3730, 2007.

[18] Piotr Bozek and Wojciech Broniowski. Correlations from hydrodynamic flow in p-Pb collisions. *Phys. Lett. B*, 718:1557–1561, 2013. doi: 10.1016/j.physletb.2012.12.051.

[19] Vardan Khachatryan et al. Evidence for collectivity in pp collisions at the LHC. *Phys. Lett. B*, 765:193–220, 2017. doi: 10.1016/j.physletb.2016.12.009.

[20] Serguei Chatrchyan et al. Long-range and short-range dihadron angular correlations in central PbPb collisions at a nucleon-nucleon center of mass energy of 2.76 TeV. *JHEP*, 07:076, 2011. doi: 10.1007/JHEP07(2011)076.

[21] Shreyasi Acharya et al. Investigations of Anisotropic Flow Using Multiparticle Azimuthal Correlations in pp, p-Pb, Xe-Xe, and Pb-Pb Collisions at the LHC. *Phys. Rev. Lett.*, 123(14):142301, 2019. doi: 10.1103/PhysRevLett.123.142301.

[22] Jaroslav Adam et al. Enhanced production of multi-strange hadrons in high-multiplicity proton-proton collisions. *Nature Phys.*, 13:535–539, 2017. doi: 10.1038/nphys4111.

[23] A. Beraudo, A. De Pace, M. Monteno, M. Nardi, and F. Prino. Heavy flavors in heavy-ion collisions: quenching, flow and correlations. *Eur. Phys. J. C*, 75(3):121, 2015. doi: 10.1140/epjc/s10052-015-3336-6.

[24] Thomas A. Trainor. The RHIC azimuth quadrupole: "Perfect liquid" or gluonic radiation? *Mod. Phys. Lett. A*, 23:569–589, 2008. doi: 10.1142/S0217732308026637.

[25] Andrei Leonidov and Dmitry Ostrovsky. Angular pattern of minijet transverse energy flow in hadron and nuclear collisions. *Eur. Phys. J. C*, 16: 683–693, 2000. doi: 10.1134/1.1481483.

[26] Christian Bierlich. Microscopic collectivity: The ridge and strangeness enhancement from string–string interactions. *Nucl. Phys. A*, 982:499–502, 2019. doi: 10.1016/j.nuclphysa.2018.07.015.

[27] Antonio Ortiz, Gyula Bencedi, and Héctor Bello. Revealing the source of the radial flow patterns in proton–proton collisions using hard probes. *J. Phys. G*, 44(6):065001, 2017. doi: 10.1088/1361-6471/aa6594.

[28] P. Bartalini et al. Multi-Parton Interactions at the LHC. 11 2011.

[29] A. Andronic et al. Heavy-flavour and quarkonium production in the LHC era: from proton–proton to heavy-ion collisions. *Eur. Phys. J. C*, 76(3): 107, 2016. doi: 10.1140/epjc/s10052-015-3819-5.

[30] S. Acharya et al. Direct observation of the dead-cone effect in quantum chromodynamics. *Nature*, 605(7910):440–446, 2022. doi: 10.1038/s41586-022-04572-w. [Erratum: Nature 607, E22 (2022)].

[31] John C. Collins, Davison E. Soper, and George F. Sterman. Factorization of Hard Processes in QCD. *Adv. Ser. Direct. High Energy Phys.*, 5:1–91, 1989. doi: 10.1142/9789814503266_0001.

[32] Shreyasi Acharya et al. Measurement of Prompt $D^0$, $\Lambda_c^+$, and $\Sigma_c^{0,++}(2455)$ Production in Proton–Proton Collisions at $\sqrt{s} = 13$ TeV. *Phys. Rev. Lett.*, 128(1):012001, 2022. doi: 10.1103/PhysRevLett.128.012001.

[33] Albert M Sirunyan et al. Production of $\Lambda_c^+$ baryons in proton–proton and lead–lead collisions at $\sqrt{s_{NN}} = 5.02$ TeV. *Phys. Lett. B*, 803:135328, 2020. doi: 10.1016/j.physletb.2020.135328.

[34] Yoshini Bailung. Measurement of D-meson production as a function of charged-particle multiplicity in proton–proton collisions at $\sqrt{s} = 13$ TeV with ALICE at the LHC. *PoS*, LHCP2021:190, 2021. doi: 10.22323/1.397.0190.

[35] Georges Aad et al. Observation of a new particle in the search for the Standard Model Higgs boson with the ATLAS detector at the LHC. *Phys. Lett. B*, 716:1–29, 2012. doi: 10.1016/j.physletb.2012.08.020.

[36] Serguei Chatrchyan et al. Observation of a New Boson at a Mass of 125 GeV with the CMS Experiment at the LHC. *Phys. Lett. B*, 716:30–61, 2012. doi: 10.1016/j.physletb.2012.08.021.

[37] K. H. Ackermann et al. STAR detector overview. *Nucl. Instrum. Meth. A*, 499:624–632, 2003. doi: 10.1016/S0168-9002(02)01960-5.

[38] P. Martinengo. The new Inner Tracking System of the ALICE experiment. *Nucl. Phys. A*, 967:900–903, 2017. doi: 10.1016/j.nuclphysa.2017.05.069.

[39] J. Alme et al. The ALICE TPC, a large 3-dimensional tracking device with fast readout for ultra-high multiplicity events. *Nucl. Instrum. Meth. A*, 622: 316–367, 2010. doi: 10.1016/j.nima.2010.04.042.

[40] A. Agostinelli. The performance of the ALICE TOF detector. *Nuovo Cim. C*, 034N06:251–252, 2011. doi: 10.1393/ncc/i2011-11102-x.

[41] E. Abbas et al. Performance of the ALICE VZERO system. *JINST*, 8: P10016, 2013. doi: 10.1088/1748-0221/8/10/P10016.

[42] K. Aamodt et al. The ALICE experiment at the CERN LHC. *JINST*, 3: S08002, 2008. doi: 10.1088/1748-0221/3/08/S08002.

[43] Christian Bierlich et al. A comprehensive guide to the physics and usage of PYTHIA 8.3. *SciPost Phys. Codeb.*, 2022:8, 2022. doi: 10.21468/SciPostPhysCodeb.8.

[44] Peter Skands, Stefano Carrazza, and Juan Rojo. Tuning PYTHIA 8.1: the Monash 2013 Tune. *Eur. Phys. J. C*, 74(8):3024, 2014. doi: 10.1140/epjc/s10052-014-3024-y.

[45] Jesper R. Christiansen and Peter Z. Skands. String Formation Beyond Leading Colour. *JHEP*, 08:003, 2015. doi: 10.1007/JHEP08(2015)003.

[46] Stefano Frixione, Paolo Nason, and Carlo Oleari. Matching NLO QCD computations with Parton Shower simulations: the POWHEG method. *JHEP*, 11:070, 2007. doi: 10.1088/1126-6708/2007/11/070.

[47] P. Nason, S. Dawson, and R. Keith Ellis. The Total Cross-Section for the Production of Heavy Quarks in Hadronic Collisions. *Nucl. Phys. B*, 303: 607–633, 1988. doi: 10.1016/0550-3213(88)90422-1.

[48] Matteo Cacciari, Mario Greco, and Paolo Nason. The $p_T$ spectrum in heavy-flavour hadroproduction. *JHEP*, 05:007, 1998. doi: 10.1088/1126-6708/1998/05/007.

[49] René Brun, F. Bruyant, Federico Carminati, Simone Giani, M. Maire, A. McPherson, G. Patrick, and L. Urban. GEANT Detector Description and Simulation Tool. 10 1994. doi: 10.17181/CERN.MUHF.DMJ1.

[50] Michael L. Miller, Klaus Reygers, Stephen J. Sanders, and Peter Steinberg. Glauber modeling in high energy nuclear collisions. *Ann. Rev. Nucl. Part. Sci.*, 57:205–243, 2007. doi: 10.1146/annurev.nucl.57.090506.123020.

[51] Kenneth Aamodt et al. Centrality dependence of the charged-particle multiplicity density at mid-rapidity in Pb-Pb collisions at $\sqrt{s_{NN}} = 2.76$ TeV. *Phys. Rev. Lett.*, 106:032301, 2011. doi: 10.1103/PhysRevLett.106.032301.

[52] T. Aaltonen et al. Studying the Underlying Event in Drell-Yan and High Transverse Momentum Jet Production at the Tevatron. *Phys. Rev. D*, 82: 034001, 2010. doi: 10.1103/PhysRevD.82.034001.

[53] Gyula Bencedi, Antonio Ortiz, and Antonio Paz. Disentangling the hard gluon bremsstrahlung effects from the relative transverse activity classifier in pp collisions. *Phys. Rev. D*, 104(1):016017, 2021. doi: 10.1103/PhysRevD.104.016017.

[54] Helen Caines. Jet and underlying event measurements in p + p collisions at RHIC. *Nucl. Phys. A*, 855:376–379, 2011. doi: 10.1016/j.nuclphysa.2011.02.084.

[55] Vardan Khachatryan et al. First Measurement of the Underlying Event Activity at the LHC with $\sqrt{s} = 0.9$ TeV. *Eur. Phys. J. C*, 70:555–572, 2010. doi: 10.1140/epjc/s10052-010-1453-9.

[56] Betty Abelev et al. Underlying Event measurements in *pp* collisions at $\sqrt{s} = 0.9$ and 7 TeV with the ALICE experiment at the LHC. *JHEP*, 07: 116, 2012. doi: 10.1007/JHEP07(2012)116.

[57] Georges Aad et al. Measurement of the underlying event in jet events from 7 TeV proton-proton collisions with the ATLAS detector. *Eur. Phys. J. C*, 74(8):2965, 2014. doi: 10.1140/epjc/s10052-014-2965-5.

[58] Shreyasi Acharya et al. Underlying Event properties in pp collisions at $\sqrt{s}$ = 13 TeV. *JHEP*, 04:192, 2020. doi: 10.1007/JHEP04(2020)192.

[59] Tim Martin, Peter Skands, and Sinead Farrington. Probing Collective Effects in Hadronisation with the Extremes of the Underlying Event. *Eur. Phys. J. C*, 76(5):299, 2016. doi: 10.1140/epjc/s10052-016-4135-4.

[60] S. Catani, Yuri L. Dokshitzer, M. Olsson, G. Turnock, and B. R. Webber. New clustering algorithm for multi - jet cross-sections in e+ e- annihilation. *Phys. Lett. B*, 269:432–438, 1991. doi: 10.1016/0370-2693(91)90196-W.

[61] Yuri L. Dokshitzer, G. D. Leder, S. Moretti, and B. R. Webber. Better jet clustering algorithms. *JHEP*, 08:001, 1997. doi: 10.1088/1126-6708/1997/08/001.

[62] Matteo Cacciari, Gavin P. Salam, and Gregory Soyez. The anti-$k_t$ jet clustering algorithm. *JHEP*, 04:063, 2008. doi: 10.1088/1126-6708/2008/04/063.

[63] J. Cleymans and H. Satz. Thermal hadron production in high-energy heavy ion collisions. *Z. Phys. C*, 57:135–148, 1993. doi: 10.1007/BF01555746.

[64] Peter Braun-Munzinger, Krzysztof Redlich, and Johanna Stachel. Particle production in heavy ion collisions. *in: Quark–Gluon Plasma 3, World Scientific Publishing (Singapore), eds.: R. C. Hwa and X.-N. Wang,*:491–599, 2004. doi: 10.1142/9789812795533_0008.

[65] Cheuk-Yin Wong, Grzegorz Wilk, Leonardo J. L. Cirto, and Constantino Tsallis. From QCD-based hard-scattering to nonextensive statistical mechanical descriptions of transverse momentum spectra in high-energy $pp$ and $p\bar{p}$ collisions. *Phys. Rev. D*, 91(11):114027, 2015. doi: 10.1103/PhysRevD.91.114027.

[66] Constantino Tsallis. Possible Generalization of Boltzmann-Gibbs Statistics. *J. Statist. Phys.*, 52:479–487, 1988. doi: 10.1007/BF01016429.

[67] Constantino Tsallis. Nonadditive entropy: The Concept and its use. *Eur. Phys. J. A*, 40:257–266, 2009. doi: 10.1140/epja/i2009-10799-0.

[68] Constantino Tsallis. *Introduction to Nonextensive Statistical Mechanics: Approaching a Complex World*. Springer, New York, 2009. ISBN 978-0-387-85358-1, 978-0-387-85359-8. doi: 10.1007/978-0-387-85359-8.

[69] Jean Letessier and Johann Rafelski. *Hadrons and Quark–Gluon Plasma*. Oxford University Press, 2002. ISBN 978-1-00-929075-3, 978-0-511-53499-7, 978-1-00-929070-8, 978-1-00-929073-9. doi: 10.1017/9781009290753.

[70] Jean Cleymans and Masimba Wellington Paradza. Tsallis Statistics in High Energy Physics: Chemical and Thermal Freeze-Outs. *MDPI Physics*, 2(4): 654–664, 2020. doi: 10.3390/physics2040038.

[71] Keming Shen, Gergely Gábor Barnaföldi, and Tamás Sándor Biró. Hadron Spectra Parameters within the Non-Extensive Approach. *Universe*, 5(5): 122, 2019. doi: 10.3390/universe5050122.

[72] J. Cleymans and D. Worku. Relativistic Thermodynamics: Transverse Momentum Distributions in High-Energy Physics. *Eur. Phys. J. A*, 48:160, 2012. doi: 10.1140/epja/i2012-12160-0.

[73] J. Cleymans, G. I. Lykasov, A. S. Parvan, A. S. Sorin, O. V. Teryaev, and D. Worku. Systematic properties of the Tsallis Distribution: Energy Dependence of Parameters in High-Energy p-p Collisions. *Phys. Lett. B*, 723:351–354, 2013. doi: 10.1016/j.physletb.2013.05.029.

[74] Pei-Pin Yang, Mai-Ying Duan, Fu-Hu Liu, and Raghunath Sahoo. Analysis of Identified Particle Transverse Momentum Spectra Produced in pp, p–Pb

and Pb–Pb Collisions at the LHC Using TP-like Function. *Symmetry*, 14 (8):1530, 2022. doi: 10.3390/sym14081530.

[75] Gábor Bíró, Gergely Gábor Barnaföldi, and Tamás Sándor Biró. Tsallis-thermometer: a QGP indicator for large and small collisional systems. *J. Phys. G*, 47(10):105002, 2020. doi: 10.1088/1361-6471/ab8dcb.

[76] Jinbiao Gu, Chenyan Li, Qiang Wang, Wenchao Zhang, and Hua Zheng. Collective expansion in pp collisions using the Tsallis statistics. *J. Phys. G*, 49(11):115101, 2022. doi: 10.1088/1361-6471/ac9074.

[77] Jia-Yu Chen, Mai-Ying Duan, Fu-Hu Liu, and Khusniddin K. Olimov. Multi-source thermal model describing multi-region structure of transverse momentum spectra of identified particles and parameter dynamics of system evolution in relativistic collisions. 10 2023. doi: 10.1007/s12648-023-03003-4.

[78] Murad Badshah, Abd Haj Ismail, Muhammad Waqas, Muhammad Ajaz, Mateen Ullah Mian, Elmuez A. Dawi, Muhammad Adil Khan, and Atef AbdelKader. Excitation Function of Freeze-Out Parameters in Symmetric Nucleus–Nucleus and Proton–Proton Collisions at the Same Collision Energy. *Symmetry*, 15(8):1554, 2023. doi: 10.3390/sym15081554.

[79] Paolo Castorina and Helmut Satz. High Energy Hadron Production, Self-Organized Criticality and Absorbing State Phase Transition. *Springer Proc. Phys.*, 250:75–81, 2020. doi: 10.1007/978-3-030-53448-6_10.

[80] Tamas S. Biro and Berndt Muller. Almost exponential transverse spectra from power law spectra. *Phys. Lett. B*, 578:78–84, 2004. doi: 10.1016/j.physletb.2003.10.052.

[81] Mubarak Alqahtani, Nasser Demir, and Michael Strickland. Nonextensive

hydrodynamics of boost-invariant plasmas. *Eur. Phys. J. C*, 82(10):973, 2022. doi: 10.1140/epjc/s10052-022-10943-4.

[82] A. Adare et al. Charged hadron multiplicity fluctuations in Au+Au and Cu+Cu collisions from $\sqrt{s_{NN}} = 22.5$ to 200 GeV. *Phys. Rev. C*, 78:044902, 2008. doi: 10.1103/PhysRevC.78.044902.

[83] K. Aamodt et al. Charged-particle multiplicity measurement in proton-proton collisions at $\sqrt{s} = 7$ TeV with ALICE at LHC. *Eur. Phys. J. C*, 68: 345–354, 2010. doi: 10.1140/epjc/s10052-010-1350-2.

[84] Vardan Khachatryan et al. Charged Particle Multiplicities in *pp* Interactions at $\sqrt{s} = 0.9$, 2.36, and 7 TeV. *JHEP*, 01:079, 2011. doi: 10.1007/JHEP01(2011)079.

[85] Tamás Sándor Biró, Péter Ván, Gergely Gábor Barnaföldi, and Károly Ürmössy. Statistical power law due to reservoir fluctuations and the universal thermostat independence principle. *Entropy*, 16(12):6497–6514, 2014. ISSN 1099-4300. doi: 10.3390/e16126497. URL `https://www.mdpi.com/1099-4300/16/12/6497`.

[86] T. S. Biro, G. G. Barnaföldi, and P. Van. New Entropy Formula with Fluctuating Reservoir. *Physica A*, 417:215–220, 2015. doi: 10.1016/j.physa.2014.07.086.

[87] Gábor Bíró, Gergely Gábor Barnaföldi, Tamás Sándor Biró, Károly Ürmössy, and Ádám Takács. Systematic Analysis of the Non-extensive Statistical Approach in High Energy Particle Collisions - Experiment vs. Theory. *Entropy*, 19:88, 2017. doi: 10.3390/e19030088.

[88] Albert M Sirunyan et al. Extraction and validation of a new set of CMS PYTHIA8 tunes from underlying-event measurements. *Eur. Phys. J. C*, 80 (1):4, 2020. doi: 10.1140/epjc/s10052-019-7499-4.

[89] László Gyulai, Szende Sándor, and Róbert Vértesi. Defining the Underlying-Event Activity in the Presence of Heavy-Flavour Processes in Proton-Proton Collisions at LHC Energies. *Particles*, 5(3):235–244, 2022. doi: 10.3390/particles5030021.

[90] Matteo Cacciari. FastJet: A Code for fast $k_t$ clustering, and more. In *41st Rencontres de Moriond: QCD and Hadronic Interactions*, pages 487–490, 7 2006.

[91] Albert M Sirunyan et al. Dependence of inclusive jet production on the anti-k$_T$ distance parameter in pp collisions at $\sqrt{\mathrm{s}} = 13$ TeV. *JHEP*, 12:082, 2020. doi: 10.1007/JHEP12(2020)082.

[92] Shreyasi Acharya et al. Measurement of inclusive charged-particle b-jet production in pp and p-Pb collisions at $\sqrt{s_{\mathrm{NN}}} = 5.02$ TeV. *JHEP*, 01:178, 2022. doi: 10.1007/JHEP01(2022)178.

[93] Yuri L. Dokshitzer, Valery A. Khoze, and S. I. Troian. On specific QCD properties of heavy quark fragmentation ('dead cone'). *J. Phys. G*, 17: 1602–1604, 1991. doi: 10.1088/0954-3899/17/10/023.

[94] Physics Preliminary Summary: $\mathrm{D}^0$ meson yields as a function of the underlying event activity in pp collisions at $\sqrt{s} = 13$ TeV. 2024.

[95] M. Tanabashi et al. Review of Particle Physics. *Phys. Rev. D*, 98(3):030001, 2018. doi: 10.1103/PhysRevD.98.030001.

[96] Shreyasi Acharya et al. Measurement of D-meson production at mid-rapidity in pp collisions at $\sqrt{s} = 7$ TeV. *Eur. Phys. J. C*, 77(8):550, 2017. doi: 10.1140/epjc/s10052-017-5090-4.

[97] S. Acharya et al. Measurement of $\mathrm{D}^0$, $\mathrm{D}^+$, $\mathrm{D}^{*+}$ and $\mathrm{D}_s^+$ production in Pb-Pb collisions at $\sqrt{\mathrm{s}_{\mathrm{NN}}} = 5.02$ TeV. *JHEP*, 10:174, 2018. doi: 10.1007/JHEP10(2018)174.

[98] Shreyasi Acharya et al. Measurement of $D^0$ , $D^+$ , $D^{*+}$ and $D_s^+$ production in pp collisions at $\sqrt{s} = 5.02$ TeV with ALICE. *Eur. Phys. J. C*, 79(5): 388, 2019. doi: 10.1140/epjc/s10052-019-6873-6.

[99] Matteo Cacciari, Stefano Frixione, Nicolas Houdeau, Michelangelo L. Mangano, Paolo Nason, and Giovanni Ridolfi. Theoretical predictions for charm and bottom production at the LHC. *JHEP*, 10:137, 2012. doi: 10.1007/JHEP10(2012)137.

[100] László Gyulai, Gábor Bíró, Róbert Vértesi, and Gergely Gábor Barnaföldi. How far can we see back in time in high-energy collisions using charm hadrons? *J. Phys. G*, 51(8):085103, 2024. doi: 10.1088/1361-6471/ad59b9.

[101] László Gyulai, Gábor Bíró, Róbert Vértesi, and Gergely Gábor Barnaföldi. Evolution of the hot dense matter at LHC energies through light and heavy-flavor hadrons using non-extensive thermodynamics. 9 2024.

[102] Shreyasi Acharya et al. Measurement of prompt $D^0$, $D^+$, $D^{*+}$, and $D_S^+$ production in p–Pb collisions at $\sqrt{s_{NN}} = 5.02$ TeV. *JHEP*, 12:092, 2019. doi: 10.1007/JHEP12(2019)092.

[103] Jaroslav Adam et al. Centrality and transverse momentum dependence of $D^0$-meson production at mid-rapidity in Au+Au collisions at $\sqrt{s_{NN}} = 200\,\text{GeV}$. *Phys. Rev. C*, 99(3):034908, 2019. doi: 10.1103/PhysRevC.99.034908.

[104] Betty Abelev et al. Suppression of high transverse momentum D mesons in central Pb-Pb collisions at $\sqrt{s_{NN}} = 2.76$ TeV. *JHEP*, 09:112, 2012. doi: 10.1007/JHEP09(2012)112.

[105] Gábor Bíró, Leonid Serkin, Guy Paić, and Gergely Gábor Barnaföldi. Is there (no) collective flow in pp collisions? 3 2024.

[106] Matthew Newville, Till Stensitzki, Daniel B. Allen, Michal Rawlik, Antonino Ingargiola, and Andrew Nelson. Non-linear least-square minimization and curve-fitting for python. *Astrophysics Source Code Library*, 1606.014, 2014. doi: 10.5281/zenodo.3588521.

[107] K. Urmossy and T. S. Biro. Cooper-Frye Formula and Non-extensive Coalescence at RHIC Energy. *Phys. Lett. B*, 689:14–17, 2010. doi: 10.1016/j.physletb.2010.04.037.

[108] Salvatore Plumari, Vincenzo Minissale, Santosh K. Das, G. Coci, and V. Greco. Charmed Hadrons from Coalescence plus Fragmentation in relativistic nucleus-nucleus collisions at RHIC and LHC. *Eur. Phys. J. C*, 78 (4):348, 2018. doi: 10.1140/epjc/s10052-018-5828-7.

[109] J. D. Bjorken. Highly Relativistic Nucleus-Nucleus Collisions: The Central Rapidity Region. *Phys. Rev. D*, 27:140–151, 1983. doi: 10.1103/PhysRevD.27.140.

[110] V. K. Magas, J. Gordillo, D. Strottman, Y. L. Xie, and L. P. Csernai. Initial state with shear in peripheral heavy ion collisions. *Phys. Rev. C*, 97 (6):064903, 2018. doi: 10.1103/PhysRevC.97.064903.

[111] Jaroslav Adam et al. Multiplicity dependence of charged pion, kaon, and (anti)proton production at large transverse momentum in p-Pb collisions at $\sqrt{s_{\mathrm{NN}}} = 5.02$ TeV. *Phys. Lett. B*, 760:720–735, 2016. doi: 10.1016/j.physletb.2016.07.050.

[112] Betty Bezverkhny Abelev et al. Multiplicity Dependence of Pion, Kaon, Proton and Lambda Production in p-Pb Collisions at $\sqrt{s_{NN}} = 5.02$ TeV. *Phys. Lett. B*, 728:25–38, 2014. doi: 10.1016/j.physletb.2013.11.020.

[113] Shreyasi Acharya et al. Multiplicity dependence of light-flavor hadron pro-

duction in pp collisions at $\sqrt{s} = 7$ TeV. *Phys. Rev. C*, 99(2):024906, 2019. doi: 10.1103/PhysRevC.99.024906.

[114] Betty Abelev et al. Centrality dependence of $\pi$, K, p production in Pb-Pb collisions at $\sqrt{s_{NN}} = 2.76$ TeV. *Phys. Rev. C*, 88:044910, 2013. doi: 10.1103/PhysRevC.88.044910.

[115] Shreyasi Acharya et al. Production of charged pions, kaons, and (anti-)protons in Pb-Pb and inelastic *pp* collisions at $\sqrt{s_{NN}} = 5.02$ TeV. *Phys. Rev. C*, 101(4):044907, 2020. doi: 10.1103/PhysRevC.101.044907.

[116] Betty Bezverkhny Abelev et al. $K^0_S$ and $\Lambda$ production in Pb-Pb collisions at $\sqrt{s_{NN}} = 2.76$ TeV. *Phys. Rev. Lett.*, 111:222301, 2013. doi: 10.1103/PhysRevLett.111.222301.

[117] Jaroslav Adam et al. Production of $K^*$ $(892)^0$ and $\phi$ (1020) in p–Pb collisions at $\sqrt{s_{\rm NN}} = 5.02$ TeV. *Eur. Phys. J. C*, 76(5):245, 2016. doi: 10.1140/epjc/s10052-016-4088-7.

[118] Jaroslav Adam et al. $K^*(892)^0$ and $\phi(1020)$ meson production at high transverse momentum in pp and Pb-Pb collisions at $\sqrt{s_{\rm NN}} = 2.76$ TeV. *Phys. Rev. C*, 95(6):064606, 2017. doi: 10.1103/PhysRevC.95.064606.

[119] Shreyasi Acharya et al. Multiplicity dependence of (multi-)strange hadron production in proton-proton collisions at $\sqrt{s} = 13$ TeV. *Eur. Phys. J. C*, 80(2):167, 2020. doi: 10.1140/epjc/s10052-020-7673-8.

[120] Sumit Basu, Sandeep Chatterjee, Rupa Chatterjee, Tapan K. Nayak, and Basanta K. Nandi. Specific Heat of Matter Formed in Relativistic Nuclear Collisions. *Phys. Rev. C*, 94(4):044901, 2016. doi: 10.1103/PhysRevC.94.044901.

[121] Keming Shen, Gergely Gábor Barnaföldi, and Tamás Sándor Biró. Hadronization within the non-extensive approach and the evolution of

the parameters. *Eur. Phys. J. A*, 55(8):126, 2019. doi: 10.1140/epja/i2019-12813-4.

[122] T. S. Biró, G. G. Barnaföldi, P. Ván, and K. Ürmössy. Statistical Power-Law Spectra due to Reservoir Fluctuations. 4 2014.

[123] R. Korus, S. Mrowczynski, M. Rybczynski, and Z. Wlodarczyk. Transverse momentum fluctuations due to temperature variation in high-energy nuclear collisions. *Phys. Rev. C*, 64:054908, 2001. doi: 10.1103/PhysRevC.64.054908.

[124] Rajiv V. Gavai, Sourendu Gupta, and Swagato Mukherjee. The Speed of sound and specific heat in the QCD plasma: Hydrodynamics, fluctuations and conformal symmetry. *Phys. Rev. D*, 71:074013, 2005. doi: 10.1103/PhysRevD.71.074013.

[125] Dushmanta Sahu and Raghunath Sahoo. Characterizing Proton-Proton Collisions at the Large Hadron Collider with Thermal Properties. *MDPI Physics*, 3(2):207–219, 2021. doi: 10.3390/physics3020016.

[126] Shreyasi Acharya et al. Prompt and non-prompt J/$\psi$ production at midrapidity in Pb–Pb collisions at $\sqrt{s_{\mathrm{NN}}} = 5.02$ TeV. *JHEP*, 02:066, 2024. doi: 10.1007/JHEP02(2024)066.